Supplementary Materials

Contents

List of Figures

List of Tables

1. Materials and Methods

Computational visual sensory ecology estimates. Here we will first provide the detailed derivation for how to relate pupil size to visual range when viewing through air. We then describe the optical properties of the simulated water used for our estimations of aquatic visual range, as well as those of four other water types we simulated to show the sensitivity of our aquatic visual range estimate to assumed water clarity. We examined two water types that are clearer and two that are less clear than our base case. We then summarize for convenience the basic formulas from Nilsson et al.[1] that we used for computing visual range in the aquatic case, and add contrast to this basic framework. Finally, we describe how range was numerically computed using these relations. The units and value of the parameters used throughout are summarized in Table S1.

Across the aerial and aquatic range estimates, two pupil sizes were considered: one for the finned tetrapods and one for the digited tetrapods, as well as ±1 standard deviation on either side of the mean for these two groups. Measurements of pupil size to orbit size in teleost fish show that pupil size is highly correlated with orbit length (p. 8). We used the mean ratio of pupil size to orbit length (γ=0.449) to scale the mean orbit length found in the finned tetrapod group and the mean orbit length found in the digited tetrapod group. We assume pupil size is fixed, as is the case for most vertebrates other than tetrapods.

Previous theories on aerial vision have used field luminance, which by definition is: $L = \int_{\lambda=400\,\mathrm{nm}}^{\lambda=700\,\mathrm{nm}} I(\lambda)P(\lambda)\mathrm{d}\lambda$, where $I(\lambda)$ is spectral radiance and $P(\lambda)$ is the luminance function. On the other hand, Hydrolight simulations provide spectral radiance information, which the aquatic vision model accounts for. As it can be seen from the definition, when using luminance we no longer have spectral information but the value of luminance is related to spectral radiance, thus making the basic theory for aerial vision and aquatic vision the same.

Aerial vision model. Visual range is partially dependent on *Meteorological Range*, which is determined only by the physical stimulus reaching the eye[2]. Calculation of meteorological range requires assumptions about inherent target luminance, target shape, background luminance, extinction factor (dissipation of light including contrast of an object), and plane of view. These assumptions, originally made by Koschmieder, are summarized by Horvath[3]; details can be found in that publication.

Meteorological range overestimates actual visual range because it does not incorporate how the eye's activation is affected by a difference in contrast (contrast threshold). Contrast threshold is related to the background luminance and angular diameter of the target on the retina[4].

Assuming white light and horizontal vision the apparent luminance B_g of an object with inherent luminance B_o and horizon luminance B_h, in terms of range r, and extinction coefficient $\sigma(\lambda)$ can be written as:

$$B_\mathrm{g}(\lambda) = B_\mathrm{o}(\lambda)\mathrm{e}^{-\sigma(\lambda)r} + B_\mathrm{h}(\lambda)\left(1 - \mathrm{e}^{-\sigma(\lambda)r}\right) \qquad [1]$$

Due to the assumption of white light we can define the luminance of the horizon (B_h) as: $B_\mathrm{h}(\lambda) = LW(\lambda)\bar{y}(\lambda)$, where L is the field luminance, $W(\lambda)$ is the spectral radiance emitted, and $\bar{y}(\lambda)$ is the color distribution coefficient. Given that $\int W(\lambda)\bar{y}(\lambda)\mathrm{d}\lambda = 100\%$ the above integral represents the total illumination on the atmosphere between the viewer and the target[4, p. 155]. Distribution coefficients $W(\lambda)\bar{y}(\lambda)$ were adapted from Middleton[4, p.152].

By definition the intrinsic contrast of an object can range from black (no reflection) (-1) to isoluminous with background (0), and then self-illuminating (> 0 to ∞): $C_O \in [-1, \infty)$[4, 5]. The inherent contrast of an object can be expressed in terms of luminance as:

$$C_0 = \frac{B_\mathrm{o}(\lambda) - B_\mathrm{h}(\lambda)}{B_\mathrm{h}(\lambda)} \qquad [2]$$

Rearranging equation (1), and substituting intrinsic contrast C_0 (Eq.: 2), the apparent luminance of an object (B_λ) can be rewritten as:

$$B_\mathrm{g}(\lambda) = B_\mathrm{h}(\lambda)\left(1 + \mathrm{C}_0\mathrm{e}^{-\sigma(\lambda)r}\right) \qquad [3]$$

Derivation of meteorological range is not dependent on an observer being present; only on the physics of light. The target discrimination criterion then relies on the assumption that if the Gaussian distribution of photon events originating from the target (N_T), and the distribution of those events from the background (N_B), are sufficiently different from the total Poisson photon noise (the square root of the sum of these two quantities), then detection is possible (Eq.: 4)[1]. An object is then seen when the following inequality holds for the detection threshold equation:

$$|\mathrm{N_T} - \mathrm{N_B}| \geq \mathrm{R}\sqrt{\mathrm{N_T} + \mathrm{N_B}}, \qquad [4]$$

where R is a reliability coefficient of 1.96 for 95% confidence.

Derivation of Firing Threshold. The total number of photons hitting the channel aimed at the target ($\mathrm{N_T} = \mathrm{N_O} + \mathrm{N_{false}}$) will be dependent on object's angular size, apparent luminance (B_g), and dark noise ($\mathrm{N_{false}}$, number of photon false detections). On the other hand, photon detection by the viewing channel due to background light ($\mathrm{N_B} = \mathrm{N_h} + \mathrm{N_{false}}$) will be determined by the horizon luminance (B_h) and dark noise.

For optimal object detectability, a channel that adapts to the angular size of the target is required. This ensures that the full width of the target can be observed.

The object and background luminance determines the number of photons available in a signal. However in mesopic (dim) and scotopic (dark) conditions, range decreases due to a lower signal ($|\mathrm{N_T} - \mathrm{N_B}|$) to noise ($\sqrt{\mathrm{N_T} + \mathrm{N_B}}$) relationship.

For a clear image the most important factor is the number of photons available in a surrounding. Small photon numbers that occur in the scotopic and mesopic regions, and large statistical uncertainties that are a result of this, cause a decrease in the resolution of an image. The amount of light that can be collected is dependent on the area created by dilation or constriction of the pupil ($\pi D^2/4$)[6]. Moreover, to control the number of possible photon detections, the integration time (Δt) changes with respect to light levels. With the optimal detection condition and equally weighted photoreceptors, the angular size of the target on the retina ($(\pi T^2)/(r^2 4)$ in steradians) will determine the channel size and thus potential resolution[1]. Sensitivity S therefore can be written as:

$$S = \begin{cases} \left(\frac{\pi}{4}\right)^2 D^2 \left(\frac{T}{r}\right)^2 \Delta t \left(\frac{kl}{2.3+kl}\right)\eta & \text{if } 1.5 \le \log B_\text{h} \le 4 \\ & \text{(photopic)} \\ \left(\frac{\pi}{4}\right)^2 D^2 \left(\frac{T}{r}\right)^2 \Delta t \left(1-\mathrm{e}^{-kl}\right)\eta & \text{if } \log B_\text{h} \le 1.5 \\ & \text{(mesopic, scotopic)} \end{cases} \quad [5]$$

In equation 5 (units provided in square brackets), D [m] is the pupil diameter, T [m] is the target width, r [m] is the distance between observer and target (referred to as range), Δt [s] is the integration time, k [μm^{-1}], l [μm], η is the photoreceptor length, absorption coefficient and efficiency, respectively. The absorption coefficient refers to the fraction of light that can be absorbed by a unit length photoreceptor; therefore an animal with a larger k value will be able to absorb a greater fraction of the incident light when compared to an animal with a lower k value[6]. The terms $kl/(2.3+kl)$ and $1-\mathrm{e}^{-kl}$ are calculated from photoreceptor absorption spectrum ($A(\lambda)$)[7], detailed further on p. 5.

Thus, if an eye has optical sensitivity S[m^2 sr] and is viewing a background scene (no object present) with spectral radiance $\widehat{R}_\text{h}(\lambda)$[photons m^{-2} s^{-1} sr^{-1}] then the total number of photons that can be absorbed by an eye from the horizon is simply $\mathrm{N_h} = \widehat{R}_\text{h} \cdot S$. Similarly, for an eye only viewing a circular object at some distance horizontally we would get $\mathrm{N_O} = \widehat{R}_\text{g} \cdot S$. In many cases it is convenient to express the mean number of photons per second entering the through the pupil ($\widehat{R}_\text{h,g}$) in terms of luminance. This can be accomplished by using the formula $\widehat{R}_\text{h,g} = (1.31\times10^{15}/0.89)B_\text{h,g}(\lambda)$, where $\bar{\beta} = (1.31\times10^{15}/0.89)$ is called the intensity parameter coefficient[8, 9].

However, for these two identical channels there is dark noise contributing false photon event detections. For aerial vision simulations, dark noise ($\mathtt{X}$) was set to be 0.080 photoisomerizations per rod per second (at a temperature of 23.5° C[10]. With the condition that channel size is dependent on the angular size of the target on the retina (Tf/r, where f [m] is focal length, and r [m] is range), we get the total number of photoreceptors that form the channel to be $(Tf/rd)^2$ (d [m] refers to photoreceptor diameter), due to an assumed square profile[1]. Combining the total number of photoreceptors in a square array channel with dark noise and integration time we get the total number of falsely detected photons to be $\mathrm{N_{false}} = \mathtt{X}(Tf/rd)^2\Delta t$. This can be further simplified by using the relationship $f = FD$ (F-number is denoted by F), which yields the relevant equation $\mathrm{N_{false}} = \mathtt{X}(TFD/rd)^2\Delta t$.

Referring back to the detection threshold equation (Eq. 4) and substituting $\mathrm{N_B} = \widehat{R}_\text{h} \cdot S + \mathtt{X}(TFD/rd)^2\Delta t$ and $\mathrm{N_O} = \widehat{R}_\text{g} \cdot S + \mathtt{X}(TFD/rd)^2\Delta t$, we get the overall firing threshold equation:

$$|(\widehat{R}_\text{g} \cdot S) - (\widehat{R}_\text{h} \cdot S)| = \mathrm{R}\sqrt{\widehat{R}_\text{g} \cdot S + \widehat{R}_\text{h} \cdot S + 2\mathtt{X}(TFD/rd)^2\Delta t} \quad [6]$$

However, calculating range based on only firing threshold for the case of aerial vision results in ranges that are larger than are psychophysically realistic. This is because it does not incorporate the effect of the eye's contrast threshold, as described earlier. By using the results reported by Blackwell[11], the contrast thresholded range for a circular object under specific lighting conditions were calculated.

Modelling visibility of objects with contrast threshold. The attenuation length of light in air is on the order of tens of kilometers[4, 12]. Therefore, what is limiting to vision is not medium attenuation but rather the psychophysical response to the apparent object contrast, which decays with distance. Contrast attenuation, similar to light attenuation, follows the expression $C_R = C_0\mathrm{e}^{-\sigma(\lambda)r}$. At a given range r the observed contrast will be lower than that of the inherent contrast of an object, and if it is below the contrast threshold (which is a function of field background luminance (L) and angular size) the object will be invisible.

The data presented by Blackwell provided a relationship between angular size of the object and contrast threshold under different adaptation brightnesses. These data were changed to the ratio of angular size of object and angular resolution of the observing channel ($\delta_0 = \delta_s/\delta_t$)[13]. The angular resolution of the channel was set to be the diffraction limit $\delta_t = 1.22\lambda/D$ for $\lambda = 555$ nm[14]. This resulted in different brightness adaptation curves for contrast threshold ($\Psi(D,T,r,L)$). Based on Duntley's approach to calculate range of visibility given atmospheric range for circular objects[2], an algorithm that combines firing threshold (to solve for atmospheric range) and contrast threshold was formulated, shown below. To see the values of the parameters mentioned, see above or Table S1, with the exception of K_t. K_t is detailed on p. 5. The inclusion of contrast threshold gives us ranges that are comparable to nomographic visibility charts calculated by Duntley[2], assuming 2 mm pupil diameter in daylight.

Algorithm 1 Liminal Target Distance

procedure FiringThreshold
  Define $\sigma(\lambda_{\mu\mathrm{m}})$, L, C_0, d, k, l, Δt, $\mathtt{X}$, R, F (Table S1)
  $\epsilon = 10^{-4}$
  $B_\text{h} \leftarrow LW(\lambda)\bar{y}(\lambda)$
  Calculate $\widehat{R}_\text{h} \leftarrow \bar{\beta}B_\text{h}(\lambda)$
  for all $D \in [1\,,25$ (mm)$]$ **do**
    while $|P-1| > \epsilon$ **do**
      $\delta \leftarrow 10^{\lfloor \log_{10}(r) \rfloor - 4}$
      $r \leftarrow r + \delta$
      $B_\text{g}(\lambda) \leftarrow B_\text{h}(\lambda)\left(1 + C_0\mathrm{e}^{-\sigma(\lambda_{\mu\mathrm{m}})r}\right)$
      $\widehat{R}_\text{g} \leftarrow \bar{\beta}B_\text{g}(\lambda)$
      $P \leftarrow \frac{\mathrm{R}\sqrt{\widehat{R}_\text{g}S + \widehat{R}_\text{h}S + 2\mathtt{X}(TFD/rd)^2\Delta t}}{|\widehat{R}_\text{g}S - \widehat{R}_\text{h}S|}$ (Eq. 6)
    r[n] $\leftarrow r$
procedure ContrastThresholdLimit
  for all $r \in r[n]$ **do**
    $K_t \leftarrow \Psi(D,T,r,L)$ (p. 5)
    $C_R \leftarrow C_0\mathrm{e}^{-\sigma(\lambda_{\mu\mathrm{m}})r}$
    if $10^{K_t} \le |C_R|$ **then**
      r[n] $\leftarrow r$
    else
      while $10^{K_t} - C_R > \epsilon$ **do**
        $\delta \leftarrow 10^{\lfloor \log_{10}(r) \rfloor - 4}$
        $r \leftarrow r - \delta$
        $K_t \leftarrow \Psi(D,T,r,L)$ (p. 5)
        $C_R \leftarrow C_0\mathrm{e}^{-\sigma(\lambda)r}$
      r[n] $\leftarrow r$

Optical properties of water for aquatic vision estimates. One necessary modeling decision for estimating aquatic visual range is the optical properties of the simulated freshwater, whose properties vary tremendously[6](p. 29). As early tetrapods predominantly emerged from freshwater rivers, streams or estuaries[15–19], which are more turbid than coastal waters, we simulated light fields based on water with lower clarity than typical coastal oceanic waters. While it is not certain how optical properties of contemporary water bodies relate to those of the Late Devonian, terrestrial plant and forest growth—which affect the clarity of freshwater bodies through runoff—was already well established at this point[20]. Ultimately, our basic findings are not sensitive to choice of water clarity: the dominant effects are due to the heavy absorption and scattering of light even in nearly perfectly clear water with its attenuation length of 24 meters[21, 22] for the most penetrating wavelengths, in contrast to tens of kilometers for air[4, 12]. Evidence for this claim is shown in Figure S6, where the impact on visual range of a variety of water types bracketing our selected water type is plotted.

We used a custom river water model whose properties are given in Table S3 (Baseline River). To place the attenuation length properties of the Baseline River water model (0.46 m, $1/c(575\text{ nm})$) in some context, a sample of 17 New Zealand rivers showed a range of attenuation lengths from 0.02 m to 2.7 m, with a 25th percentile of 0.09 m, 50th percentile of 0.2 m, and 75th percentile of 0.8 m[23], while for 11 New Zealand lakes the range was 0.5 m to 1.8 m, with 25th, 50th, and 75th percentiles of 0.6 m, 0.8 m, and 1.7 m, respectively[24]. For a sample of 88 Alaskan lakes, medians across turbid (N=23), stained (N=21), and clear (N=44) lakes were 0.3 m, 0.9 m, and 1.4 m[25]. By these benchmarks, our chosen attenuation length is around the first quartile of lake values, and above the median of river values.

The parameters shown for Baseline River in Table S3 were used as input to the radiative transfer program HydroLight (Version 5.3, Sequoia Scientific, Inc., Bellevue, WA USA) to generate the spectral radiance values ($\mathrm{L}(z = 8\text{ m}, \theta, \phi, \lambda)$), beam attenuation ($a(\lambda)+b(\lambda) = c(\lambda)$), and diffuse attenuation coefficients for radiance in the viewing direction ($K_L(z = 8\text{ m}, \theta, \phi, \lambda)$) for a water column of depth z (8 m) at different viewing angles. The depth of 8 m was chosen as it is slightly larger than the longest range estimated for our 10 cm black target, and is likely an upper bound on the depth of the relevant freshwater habitats in the Late Devonian. The parameters resulted in water with an attenuation length of $1/c(575\text{ nm}) = 0.46$ meters. The minerals and the colored dissolved organic matter (CDOM) are strongly absorbing in the blue (and water strongly absorbs in the red), so the overall water color is yellowish green. The water is most transparent (minimum in the water inherent optical properties, K-function with $\theta = 0$ and max in $\mathrm{L}(\theta = 180^\circ)$ (up-welling radiance)) near 575 nm. Outputs of HydroLight include $c(575\text{ nm}) = 2.19\text{ m}^{-1}$ (beam attenuation), $K_d(575) = 0.566\text{ m}^{-1}$ at depth of 7 m, and Secchi depth = 2.7 m.

For the purposes of this study, down-welling radiance (defined as $\theta = 0$ relative to nadir) and horizontal radiance with direction $\phi = 180^\circ$ (solar photon travel path angle), $\theta = 90^\circ$ relative to nadir were used. Outputs from HydroLight, which include absorbtion and scattering by wavelength, diffuse attenuation coefficient (K_d) by depth and wavelength, and spectral radiance values (downwelling and horizontal), were used to calculate the absorbed spectral radiance at the depth of the eye for a given viewing direction through Eq. 6.

Daylight conditions. The solar irradiance is computed by the RADTRAN-X model, which is designed to provide accurate predictions of direct solar and diffuse sky spectral irradiances onto the sea surface, given atmospheric (environmental) conditions such as aerosol type, water vapor and ozone concentrations, solar angle, wind, etc. HydroLight solves the radiative transfer equation for the radiances, and therefore requires sky radiances ($L(\theta, \phi, \lambda)$ [$\mathrm{W\,m^{-2}\,sr^{-1}\,nm^{-1}}$]). Since that is not available from RADTRAN-X, the angular distribution of the sky radiance distribution is determined using the semi-analytic formulas of Harrison and Coombes[26]. The direct and diffuse sky parts of the sky irradiance are treated separately. The direct part (when divided by the solid angle of the sun) gives the radiance looking directly at the sun (or moon), and the diffuse part sets the scale of the background sky radiance via the Harrison and Coombes model.

Moonlight Conditions. A full-moon, sea-level radiance spectrum[27] was rescaled to give a total irradiance in the 400-700 nm band of $E_d(400\text{ nm} - 700\text{ nm}) = 1 \times 10^{-3}\mathrm{W/m^2}$, which is a typical value of total irradiance for a clear atmosphere with full moon located near zenith (40°)[28]. For simulation purposes it was assumed that the fractional contributions of direct and diffuse irradiance due to moonlight and relative angular distribution of the moonlit sky were the same as for a sunlit sky. The simulation resulted in resulted in photosynthetically available radiation (PAR) values in air of 7.8 and 4.5 μmol photons $\mathrm{m^{-2}\ s^{-1}}$, as calculated from scalar and downwelling plane irradiances, respectively. These results are in agreement with experimental data that were collected under a full moon in Hawaii, which gave a PAR of 5 μmol photons $\mathrm{m^{-2}\ s^{-1}}$[29].

Starlight Conditions. The starlight spectrum used in the HydroLight runs is the average of 4 data sets which were provided by Sönke Johnsen. The spectral shape of the starlight irradiance spectrum seen in Fig. 2C of Johnsen et al.[30] was rescaled to give a total irradiance of $E_d(400\text{ nm} - 700\text{ nm}) = 3 \times 10^{-6}\ \mathrm{W/m^2}$, which is a typical value of clear atmosphere with only starlight[28]. In HydroLight this starlight was treated as 100% diffuse, since for this case there is no single source (unlike sun and moon) and instead it comes from all directions. The wavelength of the data obtained from Sönke Johnsen ranged from 350 nm to 700 nm. The irradiance data were extended to 750 nm by using the value at 700 nm for wavelengths >700 nm. This decision was based on the fact that the extraterrestrial starlight spectrum is almost flat between 700 nm and 750 nm, and begins to decrease beyond 750 nm[31].

Aquatic vision model. This derivation will closely follow Nilsson et al.[1]. Full details are provided in that publication.

The main assumptions are:

(a) Beam and background attenuation coefficients are assumed to be depth independent

(b) Target has no bioluminescent point sources

(c) Background and target signals are at least 10 photon events different

Any other assumption about channel properties are the same as the aerial vision model firing threshold derivation.

Calculation of mean number of photons absorbed by a photoreceptor. Following Warrant[7], the photoreceptor absorption coefficient per unit length, previously denoted as k, is not wavelength independent. Therefore it can be approximated as $k(\lambda) = kA(\lambda)$ where $A(\lambda)$ refers to the rhodopsin absorbance spectrum. Stavenga's SSH rhodopsin template[7, 32] parameters were adjusted to yield an absorption spectrum ($A(\lambda)$) that had the same peak as the spectral radiance curve.

Aquatic Firing Threshold. The theory behind object detection for aquatic vision is the same as the case for aerial vision. Therefore the visual range for a given pupil diameter can be calculated using the firing threshold (Eq. 6). From HydroLight, the spectral radiance in the viewing direction for a depth ($L(z, \theta, \phi, \lambda)$, p. 3) is obtained. For notational accuracy between aerial vision and aquatic vision, spectral radiances obtained from simulation previously denoted as $L(z, \theta, \phi, \lambda)$ will be denoted as $\widehat{R}_{\mathrm{h}}(\lambda)$ (for a given depth and viewing direction), which also emphasizes parallels with the aerial vision model.

Expanding on Nilsson's original work to include contrast (Eq. 3), the illumination on the intervening atmosphere will be $\widehat{R}_{\mathrm{O}} = \widehat{R}_{\mathrm{h}}(1 + C_0 \mathrm{e}^{-(K_L(\lambda)\cos\alpha + c(\lambda))r})$, in which $K_L(\lambda)$ refers to the spectral diffuse attenuation coefficient of radiance in the viewing direction (output from HydroLight simulation), and α refers to the angle of the sighting path (e.g, $\alpha = \pi/2$ for horizontal viewing, $\alpha = \pi$ for upward viewing) .

Combining background horizon spectral radiance ($\widehat{R}_{\mathrm{h}}$) with absorbance spectra to compute background photon count, and the identical equation for combining object spectral radiance ($\widehat{R}_{\mathrm{O}}$) with absorbance spectra to compute object photon count, we get

$$K = (\pi/4)^2 D^2 (T/r)^2 \qquad [7]$$

$$\mathrm{N_x} = K \int_{\lambda_1}^{\lambda_2} \widehat{R}_{\mathrm{x}}(\lambda)(1 - \mathrm{e}^{-kA(\lambda)l})\mathrm{d}\lambda,\ x \in \{\mathrm{h}, \mathrm{O}\} \qquad [8]$$

Now that sensitivity is included with the rhodopsin absorbance, the threshold equation (6) can be rewritten back in the form of the original discrimination equation (4) (remembering that $f = MD/2$ in the aquatic case for the equation $\mathrm{N_{false}} = \mathtt{X}(Tf/rd)^2\Delta t$) which results in:

$$|\mathrm{N_O} - \mathrm{N_h}| = \mathrm{R}\sqrt{\mathrm{N_O} + \mathrm{N_h} + 2\mathtt{X}(TMD/2rd)^2\Delta t} \qquad [9]$$

Contrast threshold for aquatic vision. Apparent contrast of any object is exponentially attenuated with distance in any viewing direction, while luminous density is exponentially attenuated only with depth (along z)[33]. Similar to light, contrast varies with the inclination of the viewing path but not with the position of the light source. For a sighting path inclined at an angle of α (horizontal viewing: $\alpha = \pi/2$, upward viewing $\alpha = \pi$, downward viewing: $\alpha = 0$), contrast extinction similar to the aerial case can be written as $C_R = C_0 \mathrm{e}^{(-(K_L(z,\theta,\phi,\lambda)\cos\alpha + c(\lambda))r)}$. For this study, horizontal and upward viewing directions were considered and therefore the two equations can be written in expanded form as: $C_{R,\mathrm{horizontal}} = C_0 \mathrm{e}^{-c(\lambda)r}$ for horizontal viewing, and $C_{R,\mathrm{upward}} = C_0 \mathrm{e}^{(K_L(z,\theta,\phi,\lambda) - c(\lambda))r}$ for upward viewing.

By using the framework established for the aerial case we can calculate the range of visibility for an underwater object. Algorithm 1 (Contrast Threshold Limit, p.3) was used to calculate aquatic visual range which used the same threshold values to compare between apparent contrast and observer's contrast threshold.

Contrast threshold as a function of pupil size. By definition contrast threshold refers to the contrast at which the observer can detect an object with a probability of 50%. The original data from Blackwell[11] relates human contrast threshold to the angular diameter of the object for a given adaptation brightness. However what is of importance for the paper is to be able to provide a dependence of contrast threshold to not only the angular size of the object, but also to the angular resolution of the observer. A similar relationship was analytically derived by Aksyutov who provided contrast threshold as a function of the ratio of the angular size of the object and the operational threshold of angular resolution[13]. For our study, we instead used the diffraction limit[14] for angular resolution ($\delta_t = 1.22\lambda/D,\ \lambda = 555\,\mathrm{nm}$). Therefore the relationship that we want to establish between contrast threshold (K_t) and the ratio δ_0 ($\delta_0 = \delta_s/\delta_t$, where δ_s is the angular diameter of the stimulus in milliradians) can be formulated by using Aksyutov's analytical expression. Following the derivation closely and changing the coefficients for a smooth curve we get the following governing equations based on Fechner's Law of perception:

$$\Psi(L) = (\log(L) + 3.5)/2.75$$

$$\log\delta_0^*(L) = \begin{cases} 0.928 & \text{if } \log L > 1.535 \\ 1 - (0.5\Psi(L))^{-3.2} & \text{if } -0.75 \leq \log L \leq 1.535 \\ -0.28 + (0.1\Psi(L))^{3.2} & \text{if } -2.089 < \log L < -0.75 \\ 0.14\log L + 0.442 & \text{if } \log L < -2.089 \end{cases} \qquad [10]$$

If $\delta_0 < \delta_0^*(L)$ then we get the simple relationship $\log K_t = -2\log\delta_0$. This equation handles the linear regime (negative slope) in the contrast threshold data. Therefore, the next set of equations will relate the linear regime to the non-linear regime to account for the slowing down and stabilization of the decrease in the contrast threshold. These equations were used as is from the original paper written by Aksyutov[13].

This framework provides us with a way of calculating contrast threshold (K_t) by knowing the angular size of the object (δ_s) and the angular resolution of the observer (δ_t). By relating pupil diameter (D) and contrast threshold (K_t) together, we are able to calculate the visible range of an object through Algorithm 1 as given in the Methods Section.

Contrast extraction from images. Various images of centipedes and millipedes in their native habitats were found through Google images, as well as a collection of freshwater underwater fish images from stills and videos. The colored images were converted to gray scale for pixel luminance values since the luminance of an image is calculated by the log-average luminance which converts colored images to grayscale. In the grayscale image the object (centipede, millipede, and fish) was identified. The average luminance of the object (mean of the pixel values within the identified region) was calculated (I_{O}) and the location was then masked. The masked component in

the overall image was then removed to calculate the average luminance of the background (I_b). Contrast of the image was calculated by using Weber contrast[4], $C_0 = (I_O - I_b)/(I_b)$. This definition of contrast was used for the aerial and aquatic firing threshold (Eq. 6), and the aerial and aquatic contrast threshold limit on visual range (Eq. 2).

Reaction time with respect to visual range in finned tetrapods. Because of how rapidly light is attenuated in water, for visually guided behavior in water, having to respond within a small margin of the reaction time is the normal situation, as the following estimate confirms. Visual reaction times in fish are on the order of 200–500 ms for rapidly looming aversive stimuli[34–37], and around 1000 ms for appetitive stimuli [38]. These numbers are from modern teleost fish, whose last common ancestor with finned tetrapods lived over 400 million years ago. While the relevant muscle and neural systems are highly conserved, the true reaction times for the finned tetrapods are likely to be longer.

Consider a 1 meter long finned tetrapod such as *Eusthenopteron* moving at 1 m/s (a low estimate based on swimming speeds of comparable fish[39]) with 4 meters of visual range for a prey that is 10 cm long (Fig. 4, orbit length of 11 mm, giving pupil of 5 mm, daylight horizontal). This is for a black object (contrast = −1); most prey do not have such contrast. Examining the sensitivity of range on object contrast in Figure S7, and choosing a contrast of -0.3, a more likely range is 3.6 m. If we imagine a prey detected at 3.6 m, then depending on the direction of movement, the predator could have either no time to react before the prey is lost from sight (moving away), 3.6 times the reaction time (using the 1,000 ms appetitive reaction time) if the prey is stationary and directly ahead, and some margin more with a glancing approach. Even if *Eusthenopteron* was an ambush predator, as has been suggested based on morphological parallels to extant ambush predators[15, p. 84], and therefore stationary in the water column, the visual appearance of prey would occur at the same very short range, and predators at a slightly larger range due to their larger size, and thus have similar behavioral urgency to the moving condition.

From this perspective, the emergence of vision above the water line was an escape from the necessity of being in reactive mode, to the possibility (but not necessity) of more complex processing requiring tens to hundreds of multiples of the reaction time, and beyond, from reactive mode to the possibility of deliberative mode[40, 41]. This means that non-stimulus evoked[42], internally driven behavior[43] is able to play a larger role with respect to attacking prey or avoiding predators than may be possible when vision is restricted to being underwater.

Sensitivity Analysis. Four different sensitivity analyses were performed: 1) the effects of diel activity pattern, 2) the optical properties of the aquatic habitat for aquatic vision estimates, 3) naturalistic object contrast values (rather than the black (-1) contrast that is our baseline), and 4) visual physiology model perturbations.

For both the aquatic and aerial conditions the simulation was performed in three different light conditions (daylight, full moonlight, clear sky starlight) (Fig. 4). Details regarding the generation of the spectral information for aquatic vision in these light conditions are detailed above (SI Appendix, pg. 3).

Given that the actual intrinsic water properties and organic matter concentrations are not known for Late Devonian, we generated results for the other water types as listed in Table S3. These have attenuation lengths of 1.17 m (clear), a high absorption water model at 0.52 m, a high turbidity model at 0.31 m, and a high scattering model at 0.22 m (quoted at 575 nm, the wavelength of highest transparency for the Baseline River water model used as our reference case). Results are shown in Figure S6.

In order to test the effects of more naturalistic contrasts, we extracted millipede and centipede contrast with the method detailed above (SI Appendix, pg. 5). We ran our computational model by fixing the pupil diameter (D) to finned and digited tetrapod pupil diameters, and varied contrast from -1 (black) to 4 (snow), for daylight in both aquatic and aerial conditions (SI Appendix, Fig. S7). Contrast extraction from these images resulted in the majority of the contrasts falling between -0.3 and 0.3. As shown in Fig. S7, for the finned pupil diameter, for upward aquatic viewing this results in a drop of visual range from 6.2 m to 5.0 m (for ±0.1 constrast), and for horizontal viewing from 4.0 m to 3.1 m. In the aerial case, the corresponding decline for the digited pupil diameter is from 637.1 m to ≈333 m for ±0.1 contrast.

To test the robustness of the model to visual physiology parameter changes that are environment and animal specific, following Nilsson et al.[44] we chose alternative values for the parameters listed in Table S2. Contrast threshold (explained above, pg. 5) is a function of adaptation luminance (L), pupil diameter (D), target width (T), and sensory range (r). Therefore, finding an alternative value implies changing the relating function. The relation of target diameter, adaptation radiance and contrast threshold was found for goldfish [45][Fig. 7,9; Fig. 8 shows how human contrast threshold relates to goldfish for a single target size across adaptation radiances]. For valid comparison the adaptation brightnesses for the case of human and goldfish should be similar. The maximum adaptation radiance tested for goldfish was $85\,\mu W/cm^2/\omega$, which when converted to luminance (with $P(\lambda)$ peak at 555 nm, p. 2) is about 10^2–10^3 ft-lambert. This range corresponds well to the daylight adaptation luminance used for the human contrast threshold study, and allows us to relate goldfish contrast threshold in daylight condition to human contrast threshold under the same condition.

Data from Hester's study at $85\,\mu W/cm^2/\omega$ was extracted to relate angular size of the target to contrast threshold. Human and goldfish contrast threshold data was then interpolated to obtain overlapping angular ranges. As a conclusion of this interpolation, we saw that the curves for goldfish show similarities to the curves for the human eye. This allowed us to approximate goldfish contrast threshold as a percent shift of human contrast threshold. This shift was calculated by looking at the mean percent difference between the two curves, across angular sizes. It is important to note that the percent difference was not constant. For small objects the difference was much larger (≈50%), and for large objects the difference was smaller (≈10%). However, since the object sizes used for these experiments were not the same, it is difficult to know whether this difference is an artifact of interpolation. We selected a 15% shift up from the human contrast threshold, which most likely underestimates the goldfish contrast threshold for object sizes that we are most interested in, and therefore serves as a

conservative estimate.

For each performance parameter, percent difference caused by changes to the model parameters were calculated and is shown in Table S2. Fig. 4 in study reflects the overall (across all parameters, and across all pupil diameters) maximum and minimum performance values using a green fill zone.

Code availability. All of the non-commercial code and data for generating the results and figures in our study can be downloaded through the GitHub repository at https://doi.org/10.5281/zenodo.321923. The computational vision code is in MATLAB (version 2016a, with Curve Fitting and Image Processing toolboxes, The Mathworks, Natick MA, USA), while the phylogenetic analysis code is in R (version 3.2.4, R Foundation for Statistical Computing, Vienna, Austria). The light fields were computed using a commercial package (HydroLight version 5.3, Sequoia Scientific, Inc., Bellevue, WA USA). The underlying control code for the tennis ball example (Fig. 8), sequential action control [46] is under a provisional patent application. However we are able to share it with individual investigators. Please contact Todd D. Murphey (t-murphey@northwestern.edu).

List of R Packages

1. `ape`[47]
2. `bayou`[48, 49]
3. `geiger`[50]
4. `MASS`[51]
5. `nlme`[52]
6. `OUwie`[53]
7. `paleotree`[54]
8. `phytools`[55]
9. `slouch`[56, 57]
10. `strap`[58]

2. Supplementary Text

Estimating eye and pupil size in early tetrapods. Studies of the visual capabilities of early tetrapods require estimates of soft tissue structures such as overall eye size and the size of the pupil, both of which are key parameters in optical simulations. As in other paleontological studies[59–61] with a focus on functional morphology, it is not our goal to determine the exact size of a structure (such as muscle cross-sectional area or pupil diameter) or its exact location (such as the origin and attachment of a muscle). Rather, functional interpretations in the fossil record are built on feasible ranges that likely include the true morphology of the system under investigation. It is very difficult to nearly impossible to determine the exact size of soft-tissue structures in fossils, but detailed anatomical studies and applications of the extant phylogenetic bracket provide a robust framework for modeling approaches in vertebrate paleontology that can be tested and refined whenever new data and methods become available.

As the only attributes that fossil skulls preserve are the eye socket and the scleral ring, we focus on these skeletal structures to estimate eye and pupil size. As scleral rings are rarely preserved among the early tetrapods, we largely rely on eye socket size but use the available material on scleral rings to test the validity of our model.

The size of the bony eye socket is considered a reliable proxy for eye size, as supported by data on primates[62], birds[63], and squamates[64]. In birds, the eye becomes a bit smaller compared to the eye socket as the eye size increases. For example, an eye socket with a length of 10 mm is expected to house a 9.9 mm eyeball whereas a 20 mm eye socket should hold a 18.2 mm eyeball, on average[63]. Hence, a doubling of eye socket size returns almost twice the eye size. A similar trend is seen in lizards, using an approximation of the depth of the eye socket to estimate the distance from the pupil to the back of the eye (axial length)[64], and also primates, using volume estimates of the eye socket and the eye[62].

All three examples are taken from amniotes, but does the correlation hold for other vertebrates as well? To explore this question, we went outside amniotes and phylogenetically bracketed early tetrapods with data from teleost fish. We examined a diverse sample of teleosts, including some species with strongly protruding eyes such as jawfish or sandperch and species with unusual eye placement as seen in flounders. We also wanted to determine appropriate ranges of pupil size for a given eye socket size to inform our optical model of visual performance in early tetrapods, in which pupil diameter is one of the parameters.

Schmitz and Wainwright[65] compiled a large dataset of soft-tissue eyeball dimensions in teleosts by dissecting unpreserved ("fresh") specimens shortly after these were euthanized (details on methods and IACUC approval previously published[65]). Importantly, the eyes remained fully intact and all adhering muscle and fat tissue was removed before measurements were taken. Soft tissue measurements included the equatorial eye diameter and the major axis of the pupil, both of which we are interested in. Some specimens from that study were subsequently cleared and stained with alizarin red using standard procedures and stored in glycerin so that skeletal tissue was visible whereas all soft tissue was transparent.

We measured the anteroposterior length of the right eye socket with dial calipers to the nearest 0.1 mm for a total of 161 individuals representing 79 species. The dorsal half of the orbit, or slightly more than half, is defined by a well-ossified margin, which would complete to a circular or elliptical shape (illustrations of the head skeleton in labrid reef fishes are similar[66]). If the long axis deviated from the anteroposterior axis, we measured the long axis instead of the anteroposterior length, but in most cases anteroposterior orbit length and major axis of the fitted ellipse were similar. For statistical purposes we worked with the species averages for orbit length, equatorial eye diameter, and minimum pupil diameter (Table S6). The species averages for eye diameter were calculated with measurements for right eyes only, from exactly the same specimens that were cleared and stained. Hence, the averages for orbit length and eye diameter are derived from precisely the same specimens.

We first tested if allometric effects may influence the ratio of eye to orbit size. For example, it may be possible that if the eye becomes proportionately smaller with an overall increase of orbit size (negative allometry), the ratio of eye to orbit length will be smaller for organisms with bigger eye sockets. However, non-phylogenetic least squares regression, performed in the statistical environment R (R Core Team 2015) finds a near-isometric slope of 0.95 with a standard error of 0.02. The points are very narrowly scattered around the fitted line (Figure S4) and hence the R^2 is unsurprisingly high (0.97), which strongly suggests that eye diameter can be reliably predicted from the length of the eye socket.

Phylogenetically informed results provide very similar slope values, confirming near-isometry (Figure S4). We used the `nlme` package[52] in R to explore how a Brownian or an Ornstein-Uhlenbeck (OU) correlation structure might influence the fit of a linear model using generalized least squares regression (phylogenetic GLS, or PGLS). We used a previously published [67] time-calibrated phylogeny for the purpose of generating the correlation matrix with the Brownian (BM) and Ornstein-Uhlenbeck (OU) model. Some of the species in our dataset were not included the previously published phylogeny[67]; thus the sample size for the phylogenetically informed analysis was lower than the full dataset ($N = 55$ as opposed to $N = 79$).

A detailed description of GLS in the context of phylogenetic comparative methods is available[68], but below is a brief summary of our approach. For PGLS with BM, we used maximum likelihood to simultaneously estimate the linear model and λ. λ is a parameter that multiplies the off-diagonals of the correlation matrix. If $\lambda = 1$ the off-diagonals are exactly as determined by the branch lengths of the phylogenetic tree, which is fully consistent with the BM model. For $\lambda = 0$ the off-diagonals of the correlation matrix become zero, i.e., the phylogenetic tree collapses to a star phylogeny with a giant polytomy at the root. A λ value in between 0 and 1 indicates that the best-fitting model, as inferred from the data, is intermediate between a star phylogeny and BM. For PGLS with OU, we used maximum likelihood to simultaneously estimate the linear model and α. The α parameter in the OU model describes the strength of selection towards a trait at an adaptive peak. If $\alpha = 0$ the OU model is reduced to a simple BM process. After verifying that PGLS regressions resulted in normally distributed residuals we assessed the slopes of the fitted models. The PGLS with BM correlation matrix yielded a slope of 0.97 ($SE = 0.03$) and the slope obtained from PGLS

with an OU correlation matrix was almost exactly 1 (0.99, $SE = 0.02$).

Given the near isometric scaling of eye diameter and orbit length, overall body size should not have any biasing effects on the ratio of eye diameter to eye socket length (eye-orbit ratio). On average, the eye diameter is slightly larger than the orbit length (105%, Figure S4). Eye sizes range from 83-130% of orbit length, yet this range is mostly determined by a few outliers (Figure S4). The standard deviation of the eye-orbit ratio is 6.6%.

In summary, eye socket diameter in a diverse sample of teleost fish is almost identical to the true equatorial eye diameter (Figure S4), regardless of the eyes' position on the head and their degree of protrusion. Evidence for a tight correlation of eye sockets with eye size spanning such a broad taxonomic bracket strongly suggests that eye socket size indeed reliably captures the size of the eye across a large portion of the vertebrate tree of life. Hence we turned to eye sockets as proxies of eye size in early tetrapods.

We carefully observed whether there were any indications that may suggest deviations from a narrowly confined eye-orbit correlation in early tetrapods. Potential caveats arise whenever the eye socket is poorly defined, with non-elliptical outlines due to poor skull ossification or other skull openings joining the eye socket which are related to muscles and/or glands such as in diving birds[63].

While early tetrapods generally feature well-defined elliptical eye sockets, a more ambiguous condition is found within the baphetids, where the eye sockets open into large rostral gaps (see p. 27). However, the caudal position of the baphetid eye is readily identified by the rounded outline of the eye socket portion, whereas the antorbital fenestra are angular. Further evidence for eye positioning in baphetids is provided by scleral ossicles found *in situ*[69]. *Panderichthys* features an elliptical eye socket with a major axis that is about 60 to 70 degrees rotated compared to the body midline, which seems unusual for early tetrapods. For consistency purposes, we also measured the long axis of this eye socket.

Scleral rings, ossifications within the sclera surrounding the iris, may provide estimates of eye size with smaller error margins, but their presence is not required for obtaining approximate dimensions of the eye[63]. In birds, the outer diameter of the scleral ring is usually smaller than the full eyeball diameter, even though for very large eyes the difference becomes less pronounced. On the basis of[63], for a scleral ring of 10 mm diameter one can expect an eye with a diameter of 13 mm, and an eye of 23.3 mm for a 20 mm scleral ring. This situation appears similar to lizards, with the exception of geckos where the scleral ring covers more than a hemisphere of the eyeball (pers. obs. LS). Some marine reptiles also featured such unusual scleral rings[70].

Scleral rings appeared early in the evolution of jawed vertebrates and are common in many vertebrates (with notable exceptions such as mammals and crocodiles), yet the fossil record of scleral rings in basal sarcopterygians and early tetrapods is sparse. Mostly, all but isolated fragments of the ring are preserved, which makes an accurate reconstruction of the entire structure difficult if not impossible. Completely preserved scleral rings such as in *Acanthostega*[71], *Gephyrostegus*[72], and the temnospondyl *Isodectes*[73] are rare but demonstrate that the eyes filled large proportions of the socket. The ratio of scleral ring to eye socket diameter (long axis in both cases) is 0.95 in *Gephyrostegus*, 0.85 in *Isodectes*, and 0.72 in *Acanthostega*. It is also to be expected to find some fossils with seemingly very small scleral rings for their eye socket, reflecting the variance in this correlation. One such example may be the temnospondyl *Cacops*[74]. The scleral ring of this animal is not fully articulated but its largest diameter may equal about 55% of the length of the eye socket. Compared to extant birds and lizards ([75]($mean = 72.6\%$ and $SD = 14.1\%$) the value for *Cacops* is small.

The second optical parameter we need to gauge from skeletal structures is the diameter of the pupil. One approach would be to use the inner diameter of the scleral ring, which is considered to be highly correlated with several components of the the optical system of the vertebrate eye, including pupil, cornea, and lens[63, 70, 76]. However, this approach is not feasible because of the scarcity of well-preserved scleral rings in the fossil record of early tetrapods.

To overcome this obstacle we turned to the data on teleost reef fish with the goal of testing whether eye socket size may also provide an approximation of pupil size. Employing the same statistical approach as for the correlation between eye socket and eye size, we found that orbit length indeed serves as a good approximation of pupil diameter ($R^2 = 0.76$). There is more scatter around the fitted line (Figure S4) than for the eye-orbit correlation, but that is to be expected as the pupil is important for determining light sensitivity which in turns opens the door for behavioral drivers of pupil evolution such as diel activity patterns[65]. The slope of the fitted least-square regression line indicates the presence of isometry (0.93, $SE = 0.07$), which is largely congruent with phylogenetically informed findings (PGLS BM slope 0.80, $SE < 0.01$; PGLS OU slope 0.85, $SE = 0.05$; Figure S4), even though the latter indicate the possible presence of slight negative allometry.

Given that we require estimated ranges of pupil size to inform our optical model and we are carrying out sensitivity analyses that allow us to evaluate the effect of different pupil sizes, we ignored the possible presence of minor influences of negative allometry and proceeded to calculate the mean pupil to orbit ratio (44.9%, $SD = 6.5\%$). The total range of the pupil-orbit ratio is 17.4 to 59.8% but in most species pupil size falls in the range of 40 to 50% of orbit size (Figure S4). To account for uncertainty in estimating pupil size from eye socket measurements, our plots of visual performance show a range of pupil diameters that encompass two standard deviations around the estimated mean of both the finned and digited tetrapods pupil diameters, providing an implicit sensitivity analysis.

To further test the validity of our pupil estimates, we checked whether scleral ring dimensions in *Acanthostega* and *Gephyrostegus*, both of which are among our sampled taxa, indicate similar pupil sizes as inferred by the eye socket. The scleral ring of *Acanthostega* is squished as if it was compressed standing upright on its side, and the inner diameter is not clearly discernable[71]. However, the scleral ring of *Gephyrostegus* is well preseved and its widest inner diameter equals 61% of orbit length. As the largest pupil diameter may be approximated as 0.92 times lens diameter ([63]; see also[70]) and lens diameter equals 0.702 times the inner diameter of the scleral ring[63], the pupil's largest diameter should be approximately 0.64 times the inner diameter of the scleral ring.

Thus, we estimate the largest pupil diameter of *Gephyrostegus* at 39.0% (0.65 × 61%) of eye socket length. This value is congruent with our simplified teleost approach, with pupil size estimated as 44.9% eye socket length.

Scaling of orbit and skull length in early tetrapods. Absolute eye size is an important determinant of visual performance and ecology but when attempting to understand eye size evolution, body size may have confounding effects, as bigger animals will likely have bigger eyes. Thus, the question of how eye size evolved becomes closely entangled with the evolution of body size.

A good example for this is the question what may have driven the evolution of large eyes in giant squid[44]. There is no doubt that, in absolute terms, giant squid have giant eyes, but how does that compare to their body size? Current results, which do not account for phylogenetic relationships, demonstrate that giant squid have eyes as large as they would be predicted from their large body size[77]. Put simply, giant squid have giant eyes because they are giant. The enormous size of these eyes still provides all the expected benefits for visual performance but the question of how these eyes evolved is refocused to address what may have driven the evolution of large body size.

Hence, when exploring eye size evolution one should test whether body size is an underlying factor that (partially) controls eye size. Given that our sample of early tetrapods ranges from 15.7 to 589.7 mm in skull length (see definition of skull length in Materials and Methods) there may be noticeable effect of body size on eye size. Because the size ranges of the finned and digited tetrapods widely overlap, major effects are not expected to arise from body size alone. However, to properly control for this effect we will investigate the scaling between orbit and skull length further.

When plotting the $\log_{10}$-transformed orbit length versus our measure of body size, the $\log_{10}$-transformed skull length, we indeed found a pattern of increasing eye size with skull size A convenient and easily accessible way to express relative eye size may be to simply divide eye size by a body size proxy such as body length or others. But another problem arises when using ratios as correction for size effects: the proportions of structures such as eyes may change with an increase overall body size. It is well-known throughout vertebrates that eyes tend to scale with negative allometry, i.e., they become proportionately smaller[78]. Accordingly, with an increase of overall size the ratio of eye-to-body size will become smaller.

Scaling analyses of the early tetrapod data confirm negative allometry of orbit length compared to skull length. We assessed this by phylogenetically informed generalized least squares models (PGLS) that were fitted to the data. For source and time-scaling of the phylogeny, which yielded a set of 1000 trees, please Materials and Methods in the main document. We tried two different approaches: one with a Brownian motion (BM) process to generate the correlation matrix that was passed on to the GLS model, and one with an Ornstein-Uhlenbeck (OU) process. The relevant parameters for BM and OU, λ and α, respectively, were jointly estimated with the GLS model using maximum likelihood. Some more information on this approach is provided in Section 2 above, but more details are available in a prior publication[68]. When iterating the PGLS (OU) over the entire tree sample for some instances problems with the likelihood calculations arose when estimating the best fitting model parameters. We attempted to mitigate this by using different starting values of α. If there was any indication of false convergence (e.g., flat likelihood distribution over a range of parameters and/or poor Akaike Information Criterion (AIC) scores) we discarded the result for that specific tree. PGLS with BM correlation structure did not cause problems to that extent. Comparisons between the BM and OU version of PGLS by means of AIC scores did not strongly favor one approach over the other so we continued with both.

The full exploration of the data yielded negative allometry regardless of the choice of the correlation matrix (BM or OU) and tree. We summarized the estimated slopes and their standard errors in Figure S5. The mean of PGLS (OU) slopes is 0.71 while the PGLS (BM) slopes are slightly steeper (0.78). While the orbit-to-skull size ratio is useful for illustrative purposes and initial assessments, the presence of negative allometry makes it prone to bias from scaling effects. Indeed, PGLS with correlation matrices derived from OU and BM models demonstrates that $\log_{10}$-transformed skull length has a significant negative effect on the ratio (slopes of -0.1 and -0.09, respectively). This potential problem can be accounted for by calculating the residuals from the fitted lines, which show whether a taxon has larger or smaller eyes than predicted by the independent variable. The residuals, which are still phylogenetically patterned[79] and hence still require phylogentically informed statistical analyses, are no longer biased by skull length as demonstrated by PGLS (slopes< 0.001). We passed on the residuals obtained from PGLS (OU) and PGLS (BM) to all subsequent analyses described in the Methods

Detecting eye size differences in a phylogenetic comparative framework—additional tests. In addition to the methods outlined in the study we performed other tests to check the reliability of our results. We specifically tested whether the inferred adaptive model using the unconstrained approach described earlier has better support than a simple, non-adaptive Brownian motion model, which we enforced by fixing all priors except for σ^2. We compared these two models by means of the Bayes factor, which was calculated from marginal likelihoods estimated by the steppingstone algorithm implemented in `bayou`. As this method is computationally very expensive, we randomly chose 10 trees and found very strong support in favor of the unconstrained model that infers the presence of multiple adaptive peaks of relative eye socket size.

We also considered the possibility that the rather long phase of likely regime shifts near the origin of digited tetrapods may be an effect of the inability of `bayou` to properly locate the exact position of the true shift. This may appear as a trickle-down or trickle-up pattern in the estimated position of shifts. We tested this by a simulation approach. Using the inferred σ^2 and α values of the fitted model, we simulated traits with the `OUwie` package [53] in R. We performed two different sets of simulations, differing only in the position of fixed regime shifts near the origin of digited tetrapods. One set of simulations placed the shift on the branch leading to elpistostegalians, the other set of simulations were carried out with the shift fixed on the branch defining digited tetrapods. We generated simulations over a set of 100 trees and subsequently analyzed the simulated traits with `bayou`. In both cases `bayou` identified the true position of the shift but only with marginally better support compared to the next deeper (when shift was fixed on the digited tetrapod branch) or higher branches (true shift

on elpistostegalian branch). This does confirm the presence of minor trickle-effects. To summarize, the exact position of the shift within the narrow window defined by `bayou` cannot be determined, and one also should not forget that the observed pattern may in fact be a true biological signal, with a gradual transition towards a new selective regime, which very much would mirror the gradual change in the tetrapod bauplan in this phase of evolution.

Finally, we performed an independent test of differences in eye socket size between digited and finned tetrapods. We analyzed the data with the R package `slouch`[56, 57], which uses the Ornstein-Uhlenbeck process to model trait changes over time and takes the phylogenetic history of a predictor variable into account when estimating the relation between environment and the peak state[56, 80]. The full model with relative eye socket size (orbit length residuals obtained from PGLS) as response variable, skull length as covariate, and taxonomy (digited vs. finned tetrapods) as a predictor variable experienced computational difficulties and very frequently approached parameter bounds without properly converging on a solution. However, a simplified approach yielded very strongly supported results. We compared two different models, one with and one without a predictor (digited or finned tetrapod). We set a wide parameter grid to ensure we did not miss any likelihood peaks and iterated `slouch` over the entire set of 1000 time-calibrated trees. As demonstrated by the Akaike weights (results not shown), the model with predictor variable is very strongly supported which suggests that the adaptive peaks of eye sizes in finned and digited tetrapods differ. The estimated adaptive peaks of relative eye socket size are similar to the means of the orbit length residuals of the respective groups. Estimates of the phylogenetic half-lives across the tree sample indicate that it would take 4.28 Ma or 6.71 Ma to evolve halfway from the ancestral value to the primary adaptive peak, depending on what type of residuals are used (PGLS with BM or OU correlation matrix). These halflife values are congruent with the `bayou` findings.

Vision model limitations and sensitivity analysis. As discussed above and elsewhere[59–61], functional interpretations in the fossil record are built on feasible ranges that are likely to include the true morphology of the system under investigation. Analyzing sensory consequences of the morphology is no different, but now the scope of variables whose feasible ranges need to be assessed extends from taxon morphology to select portions of visual physiology, hydrologic optics, atmospheric optics, radiative transfer physics with solar, star, and lunar spectra, and limnology.

The central finding of our study is the increase in eye socket size and change in socket position near the origin of terrestrial vertebrates, and that this, combined with the shift to aerial vision, resulted in a large jump in visual range. Our range calculation is based on a vision model that makes a number of idealizations, some described in more detail in the Methods, and the section below. The effect of these idealizations is a calculation that provides an upper bound on visual range, whether in water or in air. In prescribing what photons arise from an empty background, and those arising from a black 10 cm target, and then integrating across the photon counts for these two channels, we prescind from several important questions that we are not in a position to answer, including: a) whether the eye in question was optimized for sensitivity or acuity, and b) whether, if the background was not assumed to be empty (as it was unlikely to be in the terrestrial case), the visual system could actually resolve the target, an operation that depends on acuity and motion detection, among other aspects not incorporated in the model. We also assume that a modification of the optomechanics of the eye to account for the different accomodative needs of aerial vision compared to aquatic vision[6, 14], due to the different refractive indices of air and water, evolved by the time of the Elpistostegalians, 385 Ma ago. Eye evolution modeling studies suggest this may have happened relatively rapidly[81].

The biggest effect on visual range by far is simply due to how rapidly pure water absorbs light, and in that sense our result about the dramatic change in visual range makes no assumptions about Late Devonian conditions beyond that there was in fact a shift from aquatic to aerial vision—which is already known to be true based on fossil data. Substantial variations in water clarity were nonetheless tested, as shown in Fig. S6, and the differences shown there between the baseline river water model and four other types do not affect our conclusions. Importantly, the dramatic change in range is also robust to whatever diel activity pattern early tetrapods preferred: in the worst case, if an aquatic early tetrapod only used vision underwater in full daylight, and then engaged in aerial vision only on moonless nights, the increase in range is still over a factor of ten (Table S4).

We also analyzed whether more naturalistic values of contrast than -1 (black) used for our calculations would affect our result. This analysis is shown in Figure S7. As shown with our sample of naturalistic images in that figure, a more realistic contrast value for the context of predation is around ±0.3. In the aquatic case, a contrast of -0.3 results in a drop in range from 4.0 m for horizontal vision and 6.2 m for upward vision, to 3.6 m and 5.5 m, respectively. In the aerial case, the same contrast level leads to a drop from 637 m to 474 m. As our analysis primarily concerns differences between aquatic and aerial vision, this slightly higher penalty for aerial viewing is a relatively minor effect given the size of the range differences between water and air. To model contrast threshold, we use human psychophysical data (see below, p. 5). Human contrast threshold is slightly lower than that found for goldfish[45, Fig. 8]. Therefore, the decrease in range with reduced contrast that we show in Figure S7 will be slightly higher for goldfish.

Due to the low attenuation lengths of the aquatic conditions, the difference in the number of photons between the background and the object goes below our criterion of detection before the contrast threshold is reached. Thus, the contrast portion of our algorithm (Methods, p. 3) is never entered for the aquatic simulations, and are therefore not affected by uncertainty in contrast threshold value.

Finally, we examined the effect of perturbations (taken one at a time) of critical visual physiology model parameters, as described in Materials and Methods and Supplementary Materials and Methods. The minimum and maximum effect off all these perturbations composes the green fill of Fig. 4. These alterations of the vision model do not significantly impact our conclusions.

Visual sensitivity and resolution. In the framework of this model, the visual system has only two channels: one which sees only an empty background, and one which sees only a given target[1]. In neural terms, it would be as though all

the photoreceptors of the eye were divided into two groups, with all the signal from one group aimed at the background scene going to a single ganglion cell, and all the signal from another group aimed at the target going to a second ganglion cell. While a real eye with millions of photoreceptors samples a visual scene more or less proportionate to target size in relation to background, the simplified 2-channel model enforces that target and background are given equal weight. For a close target, this could result in an assumption of convergence of signal related to the target across more of the retina than is typically seen in vertebrate eyes, while for a distant target, it could result in an assumption of convergence of signal related to the background across more of the retina than is typically the case. In this approach, there is no representation of an eye's resolution, which determines resolvability of a target: target-object separation is prescribed the allocation of incoming photons to either the background or target channel, and in the assumption of an empty background (Methods, p. 2).

To better understand relationships between the visual range predicted by the model, eye size, acuity, and sensitivity, we need to consider how these constituents of visual performance are regulated for real eyes. Visual sensitivity and acuity can be estimated with equations that represent first-order properties with several simplifications.

The sensitivity of an eye, defined as the number of photons (n) caught per receptor when the eye views a scene of standard radiance (R), is given as $S = n/R = 0.62D^2\Delta\rho^2 P_{\text{abs}}$[14](Eq. 3.6), where D is the diameter of the pupil, $\Delta\rho$ is the angle in space over which each receptor accepts light, and P_{abs} is the proportion of photons entering the receptor that are absorbed by the photopigment. As $\Delta\rho$ is given by d/f, where d is the diameter of the photoreceptor, and f is the distance from the nodal point (near the center of the lens) to the retina, we can simplify this to $S = k(D/f)^2 d^2$ where k is a constant (assuming that the receptor length does not change). Two important factors for sensitivity are therefore $(D/f)^2$, equivalent to $(1/F\text{-number})^2$, and d^2. The F-number of humans is 8 in daylight and 2 at night. The F-number of fish is around 1, and pupillary responses changing D are typically quite limited in extent, reflective of the less bright conditions in aquatic habitats, but there are important exceptions in animals that sit on the substrate with dorso-ventrally flattened bodies and eyes situated at the top of the head[82], and several other cases. In the closest living relatives to the land vertebrates, the lungfish, the pupillary response is modest and slow[83]. The second factor, the diameter of receptors d, is larger in dim light specialists. For example, lungfish rod diameters are 18.6 μm, in contrast to the typical 2–6 μm diameter for most fish rods cones[1, 84], giving a sensitivity increment 10–80 times over typical values. Further gains can be achieved by pooling signals across photoreceptors, making a larger effective d, and through integrating signal over a larger time period[85]. In some vertebrate eyes, for example, the peripheral visual field has a large convergence ratio to maximize sensitivity, while the center of the visual field (fovea or area centralis if present) has a low or even negative convergence ratio.

Visual acuity is the minimum distance between equally wide black and white strips before the ability to distinguish these strips fails. An equivalent number is the sampling frequency, how many black-white cycles can be resolved per visual radian. That is given by $v_s = f/(2s) = 1/(2\Delta\phi)$[14](Eq. 3.2), where s is the separation of receptor centers, f is the distance from the nodal point to the retina as before, and $\Delta\phi$ is the inter-receptor angle equal to s/f at the nodal point. As mentioned before, acuity is not represented in our model. Provided the net difference in photons between, for example, a rectangle of alternating white and black bars (the "target", $C_O = -0.5$, Methods Eq 2) and an empty background of defined luminance meets the detection threshold (set by the firing threshold equation, Methods Eq. 6), then the visual grating would be in range. However, if the grating is in range, but the bars of the grating can not be resolved because acuity is too low, then the grating would just be perceived as a gray object.

For concreteness, let's consider a baseline case consisting of the eye of the Australian lungfish, *Neoceratodus forsteri*[83, 84, 86], a member of the group of living animals that are closest to the tetrapods. The retinal array is "packed," meaning that an increase in the diameter d of a photoreceptor to increase sensitivity comes at the expense of increasing the distance s between receptor centers, thereby decreasing resolution. If we triple the eye diameter while keeping d and s constant, then by inspection we can triple acuity while maintaining the original sensitivity, enabling resolving a distant target at three times the distance. Instead of tripling acuity, if the original acuity level is adequate, then sensitivity could be increased by a factor of 3^2 through either tripling d, or by effectively tripling d through pooling of receptor signals through convergence. Under this scenario, if we are just able to detect an object, increasing sensitivity by a factor of 9 in this way would triple the distance of detection because range depends on the square root of sensitivity in good viewing conditions (see Eq. 6 without dark noise, Methods). As light levels reduce, the increase in range will be less than the square root of sensitivity.

Thus, as the eye triples in size, we can think of two poles on a continuum of eye designs between those maximizing final acuity while not changing initial sensitivity, and maximizing final sensitivity while not changing initial acuity: A tripling of acuity (leading to a tripling of distance an object can be resolved with a cluttered background), or a nine times increase in sensitivity (leading to a tripling of distance to detect an object, at best). An example of how tripling sensitivity might have been beneficial is that certain terrestrial prey, such as the millipedes that preceded the tetrapods on land[87], may have been nocturnal or rapidly switched to a nocturnal lifestyle under diurnal predatory stress; alternatively, they may have reduced their contrast to their background. In either case, heightened sensitivity would have been a great advantage, and at best let the animal see its target from three times the distance. As an example of how tripling acuity might have been beneficial, imagine a prey whose size is at the limit of resolution in terms of being able to identify it against a background of vegetative clutter at similar spatial frequency, with no lack of light to see target or background adequately. With a tripling of eye size, the prey could be resolved at three times the distance, rather than its presence being lost in the background due to undersampling.

Between these two poles, there are reasonable arguments favoring bigger eyes for better sensitivity, as well as bigger eyes for higher acuity. Regardless of specialization for acuity or sensitivity, however, the visual range increases with eye size. On the side of better sensitivity, nocturnality is often

viewed as a response to diurnal predatory stress. But at least on land, vertebrates had not yet arrived in force at the time of the elpistostegalians and early digited tetrapods. In water, it is possible that the elpistostegalians were dim light hunters to avoid predation by large diurnal aquatic predators (hiding during the day) known to be present at that time, with corresponding visual specializations for low light over sensitivity similar to extant crocodiles[88]. Yet, the aquatic eye is already one geared to the relatively lower light levels of aquatic scenes, as witnessed by their low F-number. On the side of better acuity, while visual range in the aquatic habitats that terrestrial vertebrates emerged from was so short that visual interference by clutter may not have been problematic, once range is greatly amplified by vision through air this changes. When viewing a terrestrial habitat full of vegetation, as they were by the Late Devonian[20], perception of targets amidst clutter is very likely to be crucial, an operation that depends on acuity.

A final point can be made on the side of the importance of acuity with emergence on to land. The body's mechanical abilities transformed with emergence on to land, transforming the complexity of the visual stimulus for prey and predators alike (herbivores only arose tens of millions of years later[89]). For example, the shape of a fish, and therefore, with projective geometry, its visual appearance, can be captured by applying as few as eight degrees of freedom to a deformable model of its body, not including fin shape (three for position, three for orientation, and two non-rigid degrees of freedom for axial bending)[90]. This changes greatly as the body plan of early vertebrates gained additional degrees of freedom for forays on to land. With *Tiktaalik* we have the first mobile neck[18], enabling rapid lateral snapping motions to capture prey as well as wider sampling of visual space without full body rotation. The pectoral and pelvic fins are adapted into proto-limbs[18, 91] with new directions of movement. By the amniote-like *Casineria*, 40 million years after *Tiktaalik*, there is a fully pentadactyl forelimb, a hand capable of flexing with claw-like terminal elements, and adaptations to limb bones—such as a 90 degree twist in the upper forelimb that allowed what was once a lateral paddle-like pectoral fin to be a limb that could support a forward-facing foot—that enabled efficient movement over ground[92, 93]. The hand of *Casineria* alone, inasmuch as it is similar to a contemporary hand, may have required 30 degrees of freedom[94] applied to a model to obtain the correct shape. These additional mechanical degrees of freedom of the axial and appendicular musculoskeletal systems would have necessarily led to a much larger range of "indicative motion" (subtle movements that can indicate what behavior is about to occur), potentially observable by sufficiently acute eyesight. Subtle changes in body shape that identify a potential predator crouching to hide, preparing to run, or turning its head toward you would advantage higher visual acuity.

How temporal/spatial range affects optimal decision making. While prior theories of planning have suggested that computation expands exponentially with the complexity of the environment—including optimal control[95] and probabilistic planning[96]— recent model predictive control methods[46, 97] predict computational burden roughly proportional to environmental complexity. For example, sequential action control only requires optimization of a single decision and its impact on the long time horizon evolution of a system, taking into account measurements acquired as the sensory volume changes.

An idealized scenario to illustrate the relationship between spatial sensing range, temporal reasoning ability, and environmental complexity is as follows. Consider holding a ball, at a height of roughly 1 m (Figure S8). If one drops the ball, it accelerates towards the ground and then rebounds with a coefficient of restitution; in the case of a tennis ball, roughly 0.8 of the energy is captured after rebound. If the goal is to have the ball at a height of 1 m ten seconds later, what is the best control strategy? First, the control decision-making can only depend on the ground if it is within visual range. If it is outside visual range, the solution has to be to simply hold the ball in place. If the control system can only reason about its physical future for a short period into the future, the effect of dropping the ball cannot be taken into account long enough to see any energetic advantage associated with the ball bouncing. Hence, it is only when the temporal horizon becomes sufficiently long that one can expect to see exploitation of the ground to minimize force (and energy) expenditure. Figure S8 illustrates this trade-off. For different time horizons, control was computed using the sequential action control method[46] (for this example many optimal control algorithms would provide the same result). As the time horizon increases, the total force required to manipulate the ball over the total experiment time goes down to 8% of the value needed for simply holding the ball against gravity. Animals emerging onto land would have experienced much more dramatic decisions, but the main conclusion still holds—the longer they could reason into the future, and the more of their spatial environment they could perceive, the more efficient they could be.

3. Supplementary Figures

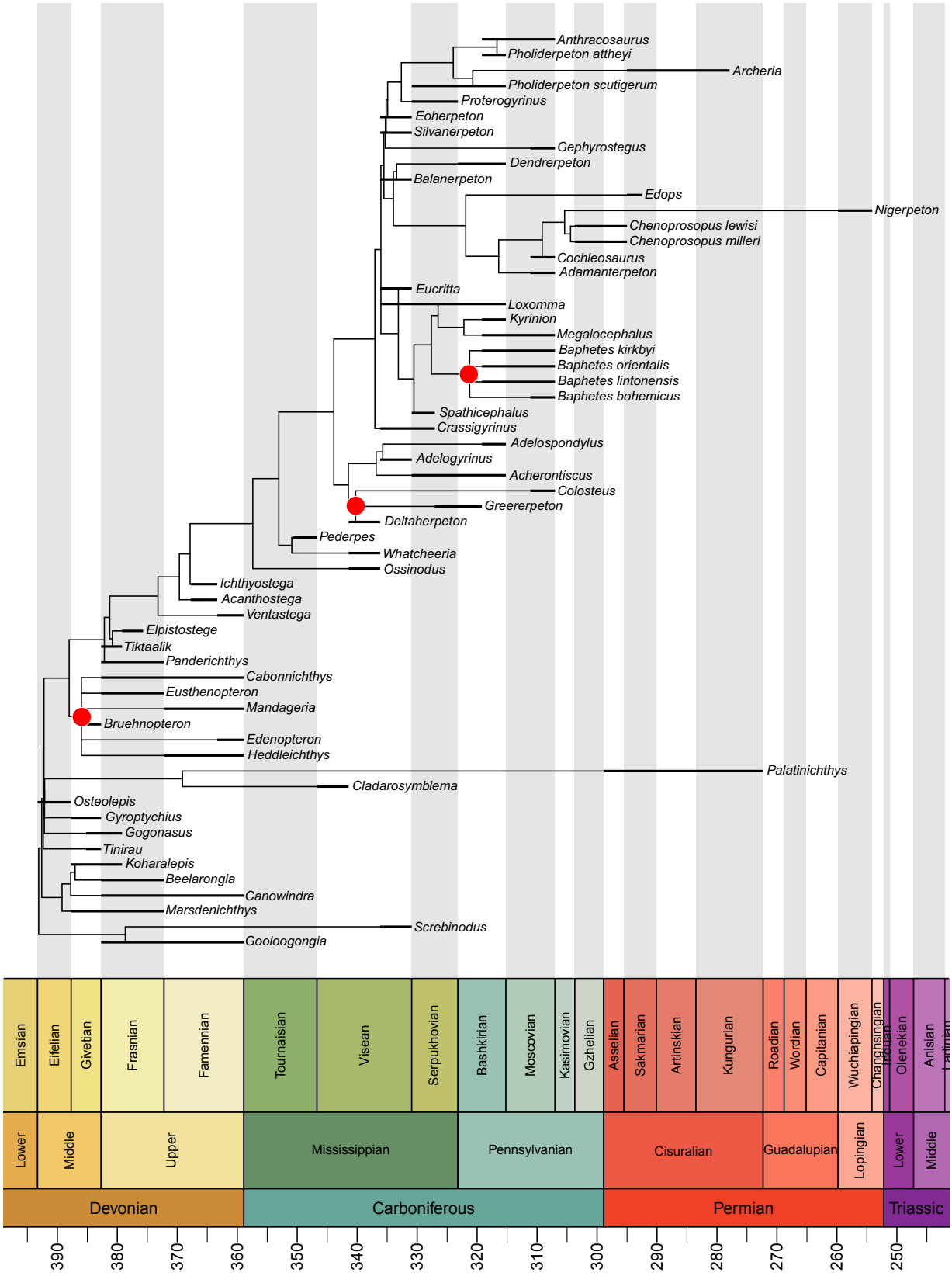

Supplementary fig. 1. The basic time-calibrated phylogeny, including polytomies (indicated by red dots), plotted against geologic time in millions of years. The stratigraphic ranges of all taxa in our analysis are superimposed. For all comparative analyses, the polytomies were resolved in a random fashion.

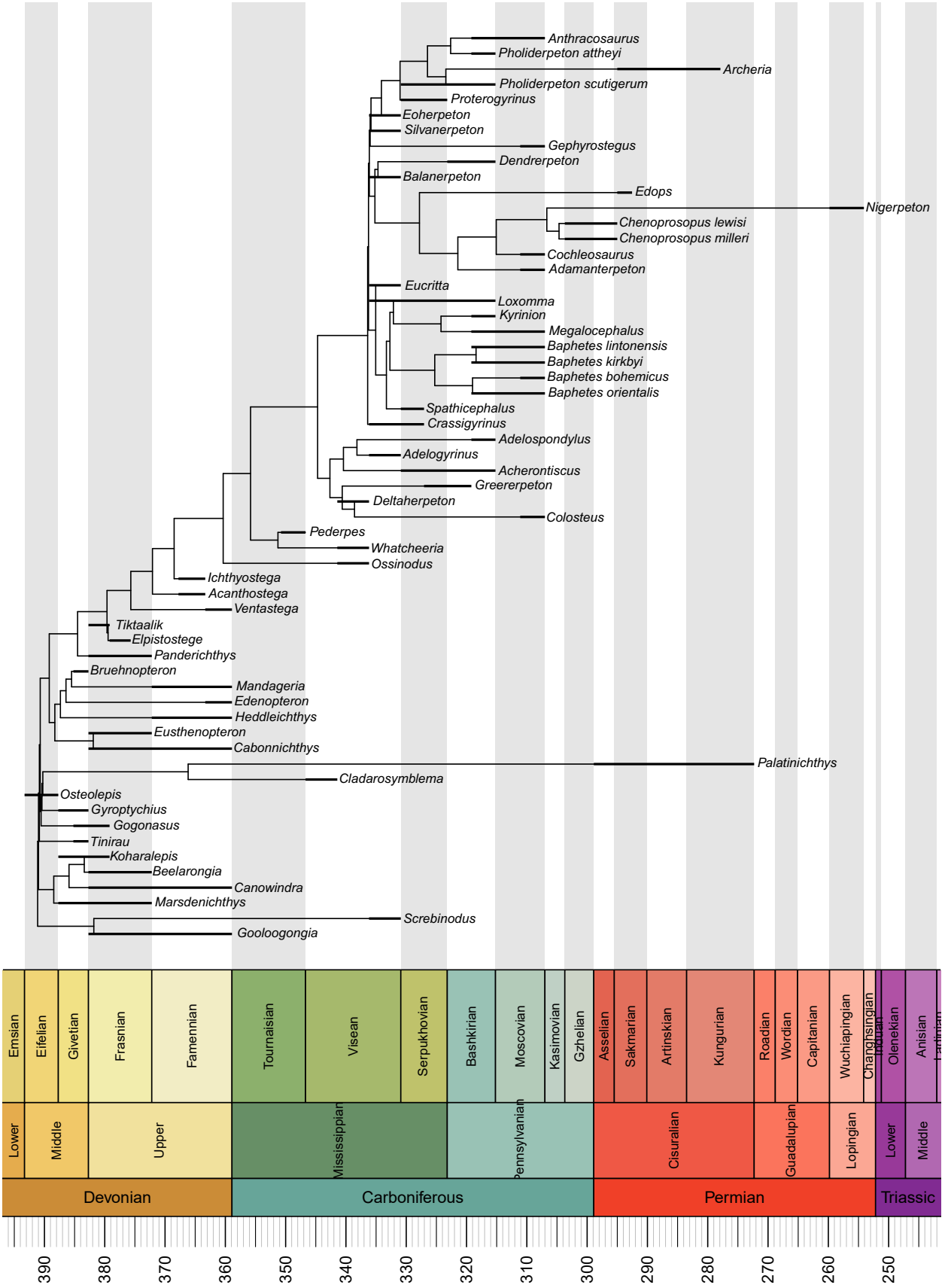

Supplementary fig. 2. The time-scaled and randomly resolved phylogeny of taxa in our sample. We generated 1000 such trees to account for the uncertainty of phylogenetic inferences that may influence our analyses.

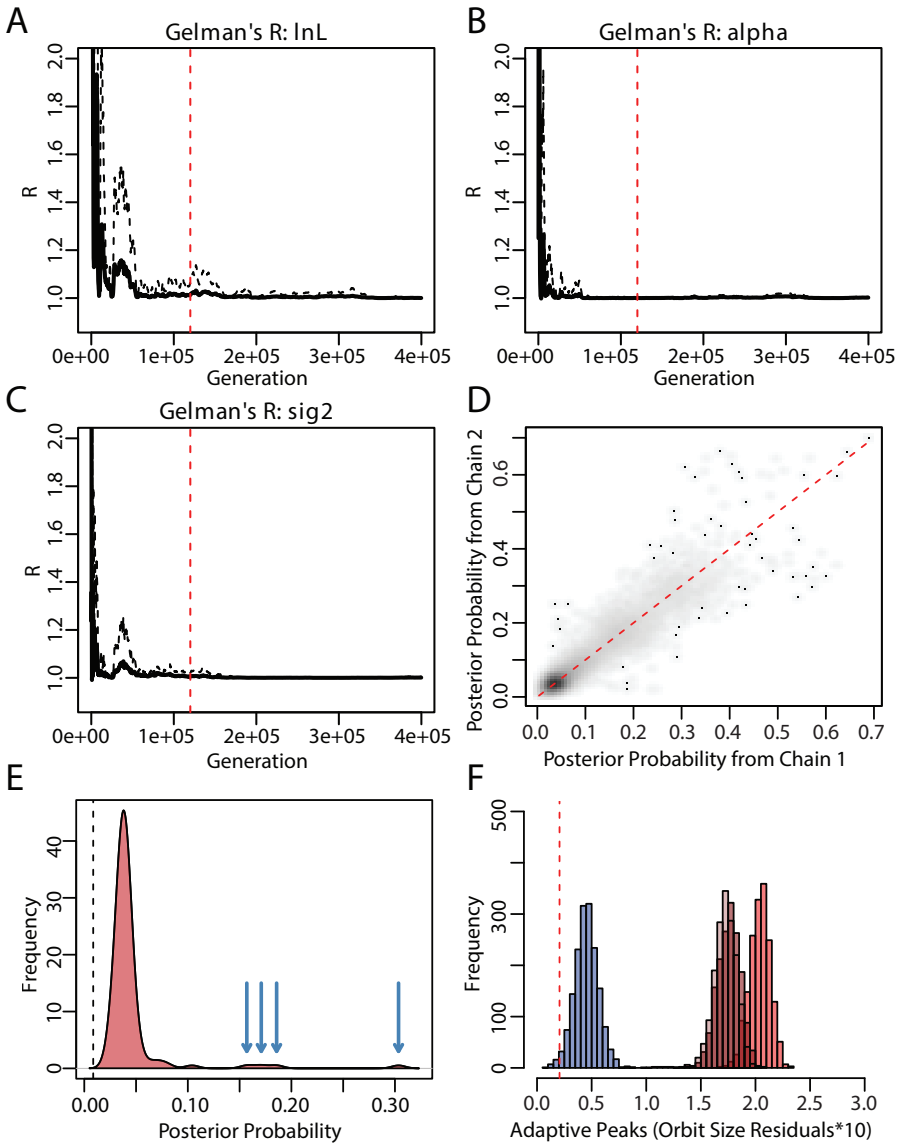

Supplementary fig. 3. Evaluation of the results from the bayOU analysis with BM residuals from PGLS. Panels a-c show Gelman's R plots for log likelihood, α, and σ^2 estimates from one example tree in our sample. If convergence is achieved the two lines should almost completely overlap. The dashed red line is the cut-off for burnin. All chains to the left are discarded. Another strong sign of convergence of the MCMC chains is presented in (d), a smooth scatter plot of posterior probabilities of shifts obtained from independent runs across all 1000 tress. If convergence is achieved the points should fall along the line of slope 1 (dashed red line). The posterior probabilities of shifts along four branches stand out from all others (e) which indicates strong support; the dashed line represents the prior probability of a shift to occur. The corresponding adaptive peaks in relative eye size (residuals10) are shown as histograms in (f). The ancestral adaptive peak in relative eye size is indicated by the red dashed line.

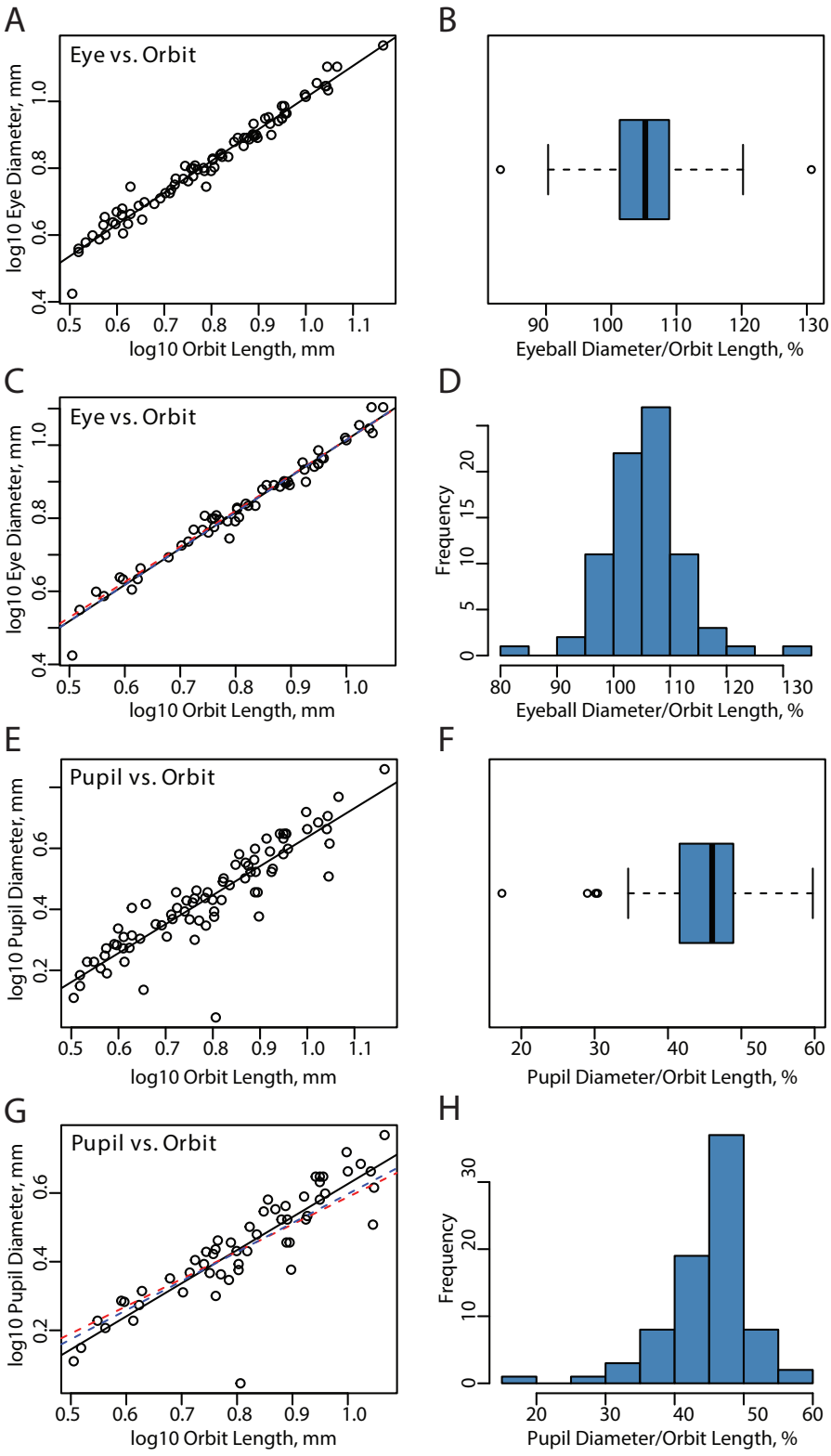

Supplementary fig. 4. Investigations of teleost fish suggest that the well-known eye-socket/eye correlation in amniotes can be extended to a broader range of vertebrates. Orbit length is a proxy for both equatorial eye diameter (a-d) and pupil diameter (e-h). We assessed the utility of the eye socket as a proxy for eye dimensions by GLS models, both in the conventional (a and e) as well as with phylogenetic correlation structures (c and g). Black solid lines in the bivariate plots indicate conventional GLS, red dashed lines are PGLS models with a BM correlation structure, while blue dashed lines signify that an OU correlation matrix was passed to the model. We also used box plots (b and f) and histograms (d and h) of the eye-orbit and pupil-orbit ratio to illustrate what range of eye and pupil sizes, respectively, can be expected for given size of the eye socket.

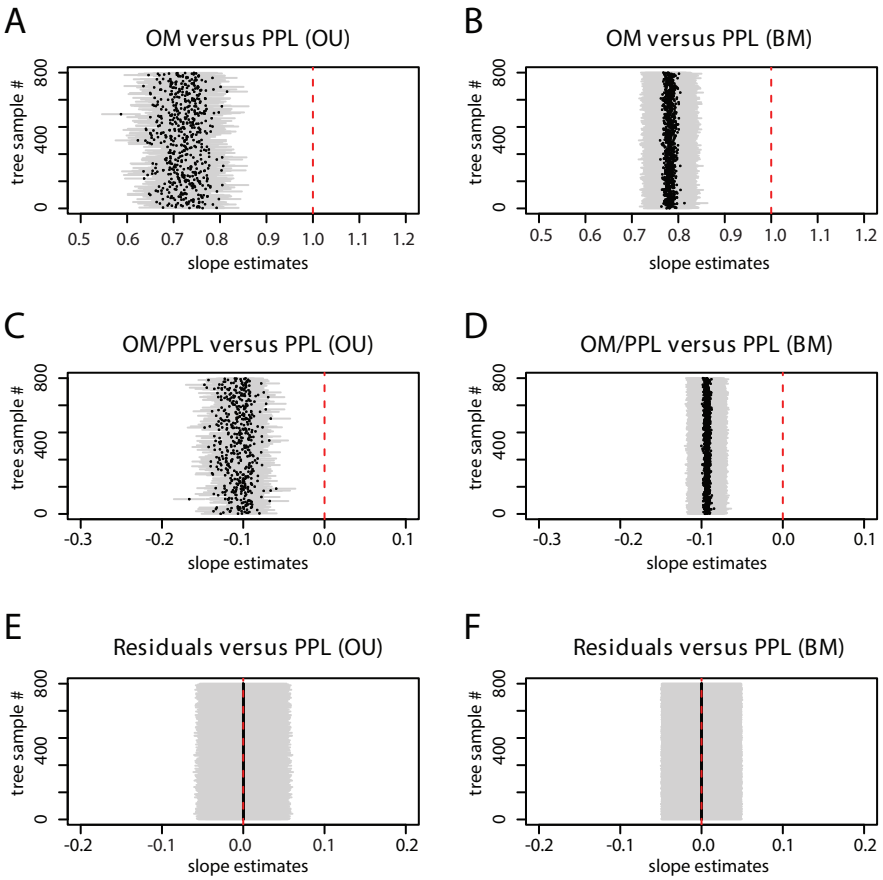

Supplementary fig. 5. Orbit length (OM) does not increase at the same rate as skull length (PPM) as is demonstrated by slope estimates from a PGLS model with either OU (a) or BM (b) correlation matrix. The plots in (a) and (b) show the slope estimates (black dots) and the associated standard error (grey bars) over all 1000 trees. If orbit length increased at the same rate as skull length, the estimated slopes should be 1 (dashed red line). As a consequence, the ratio of orbit length/skull length becomes smaller with an overall increase of size, as indicated by the negative slopes for the correlation of the ratio (OM/PPL) and skull length (PPL; c and d; in this case the dashed red line indicate the expected slope for proper size correction). We resolved this scaling bias by using residuals from a PGLS model, which are void of size effects as evidenced by slope estimates of 0 (e and f).

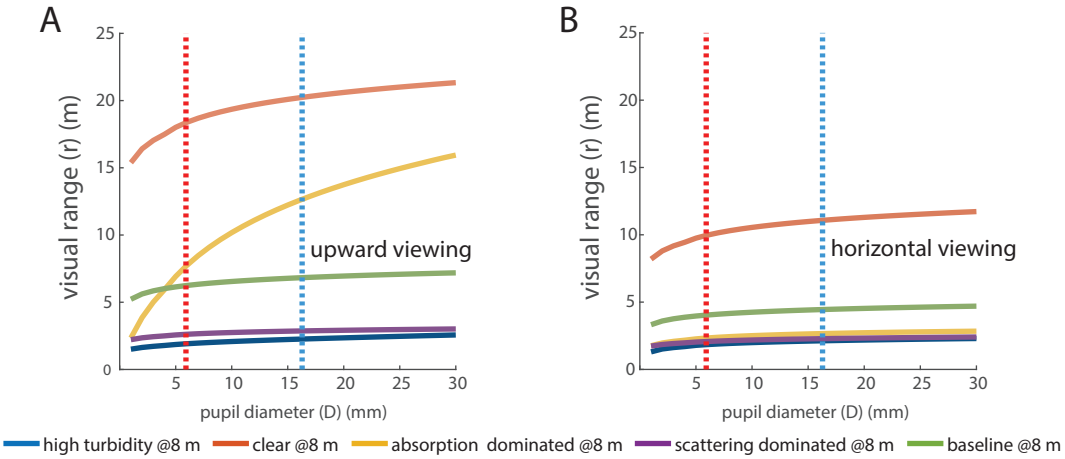

Supplementary fig. 6. Visual range when looking up toward the water surface (left) and when looking horizontally, at 8 m depth, for each water type in Table S3. The vertical lines indicate the mean finned (red) and digited (blue) pupil diameters.

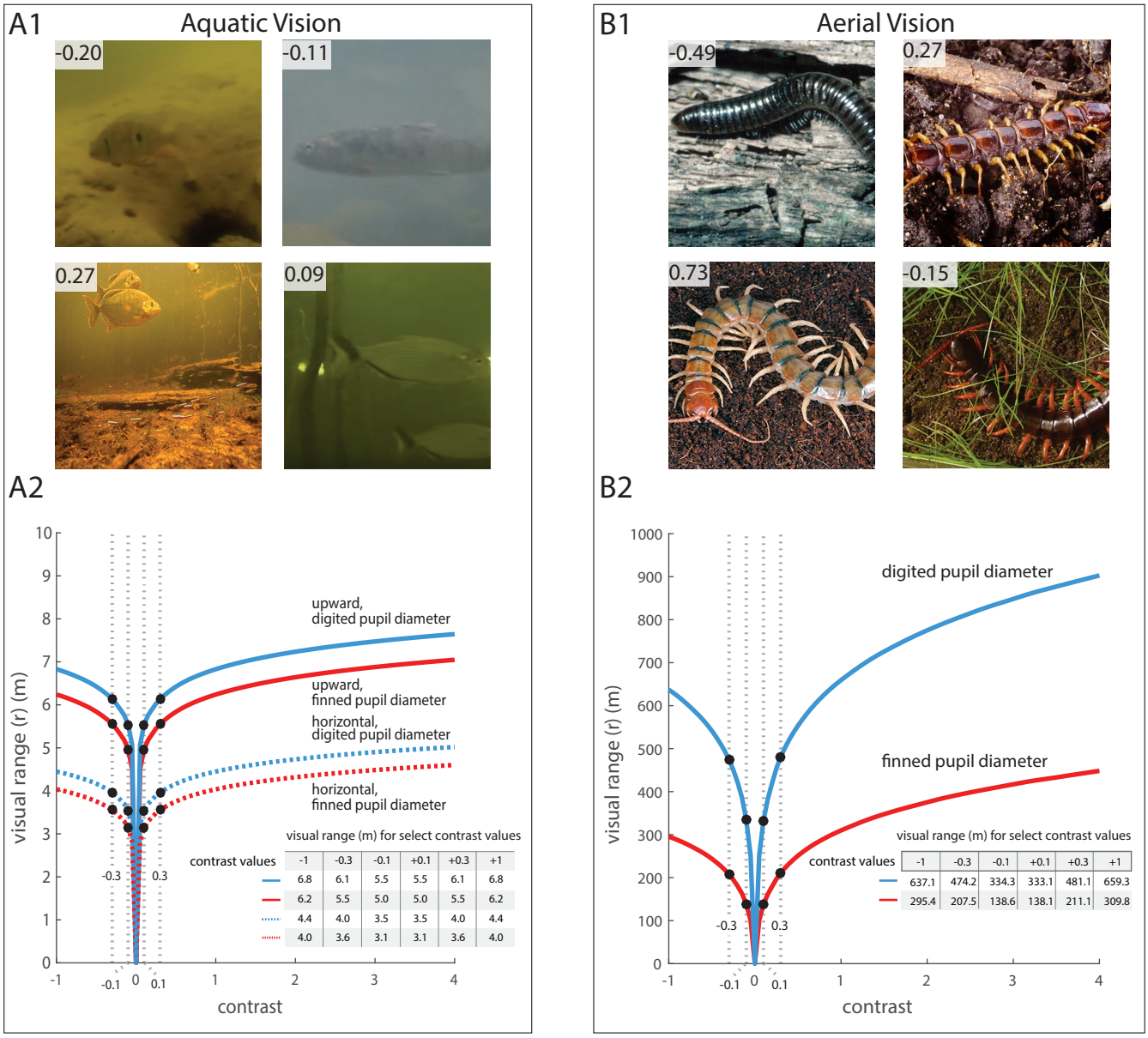

Supplementary fig. 7. Visual range in daylight conditions for aerial and aquatic vision with respect to the contrast of a 10 cm diameter disk. A contrast value of -1 is black, and +1 is white. **a1**, Sample images of fish for illustrating relevant aquatic contrast values. The contrast extraction procedure is explained in Methods, p. 5. **a2**, The contrast and visual range relationship for aquatic vision. Visual range was calculated for the baseline river water model in daylight conditions for upward viewing, by using Eq. 9 with contrast threshold limitations (p. 5). Both the firing threshold and contrast threshold were taken into account in calculating visual range (Methods p. 3). **b1**, Sample images of centipedes and millipedes used for illustrating relevant aerial contrast values. The same procedure outlined in p. 5 was used to calculate contrast values of aerial images. **b2**, Contrast and visual range relationship based on the aerial vision model. Visual range was calculated for the daylight condition by using the algorithm given in Methods p. 3, which implements both firing and contrast thresholds.

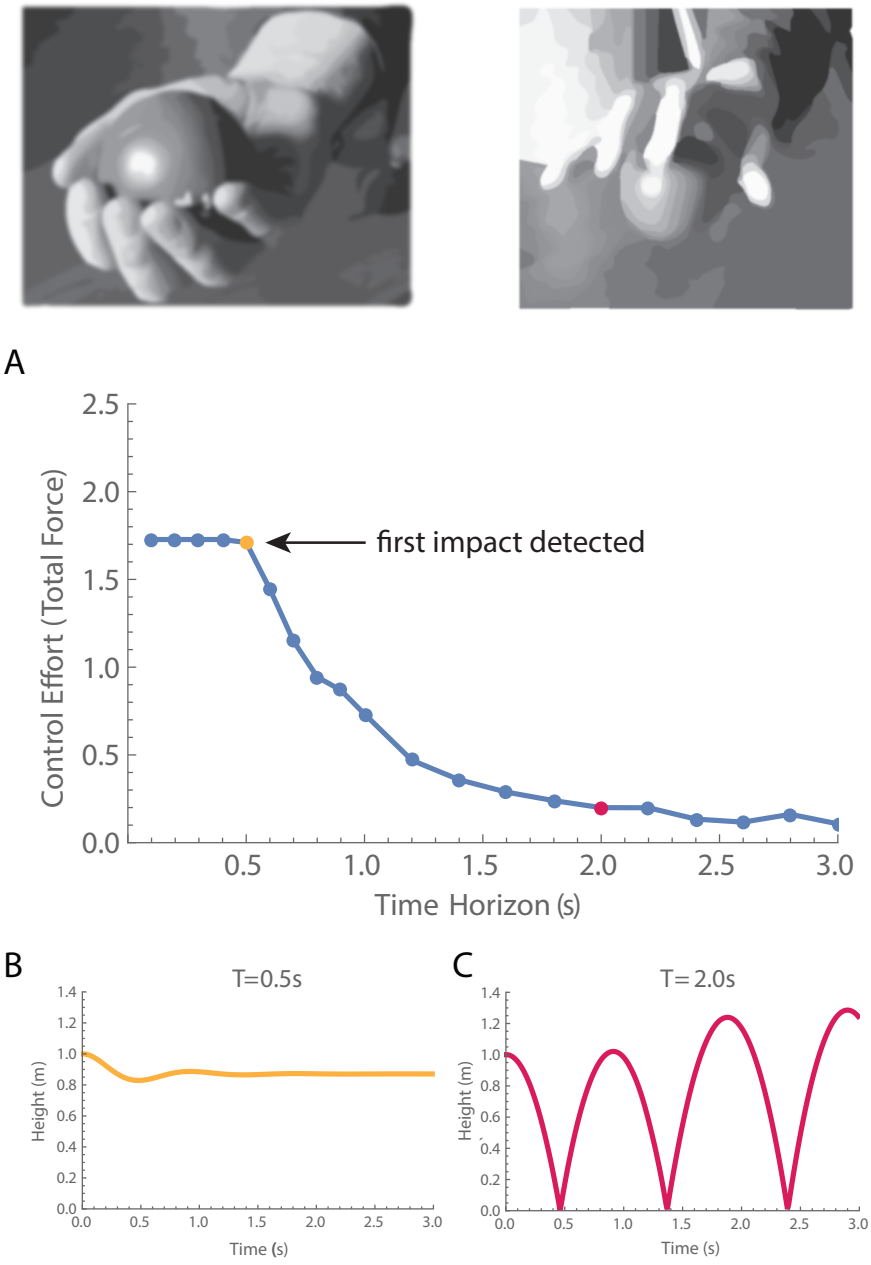

Supplementary fig. 8. Two strategies for holding a ball at a given height. **a,** Numerically approximated optimal control solutions for controlling a ball starting at rest at $y = 1.0$ m to the same state $y = 1.0$ m four seconds later (only horizons up to $t = 3.0$ s are shown). Each point on the plot represents a simulation that minimizes total force ($\int_0^T \frac{1}{2}\text{force}(t)^2 dt$) over the four second experiment time, while predicting over the corresponding time horizon T (starting at a plausible small planning horizon of $T = 0.2$ s). The dynamics of the ball include gravity and a coefficient of restitution of 0.8 (the coefficient of restitution of a tennis ball). When the horizon T is short, for instance below $T = 0.5$ s, the most energetically efficient solution is to hold the ball in hand against the force of gravity at the desired height, such as the $T = 0.5$ s solution shown in **b**. However, with a high coefficient of restitution, the more efficient solution is to bounce the ball, such as the the $T = 2.0$ s solution shown in **c**, and then use a smaller amount of force to correct any height loss due to energy dissipation during impact. However, this solution requires more than $T = 0.5$ s look-ahead time since otherwise the advantageous effect of the floor cannot be incorporated into the strategy. The longer time horizons eventually only use 8% of the total force required by the short duration holding strategy. For further details, see p. 13.

4. Supplementary Tables

	Parameter	Value	Definition	Reference
All Models	γ	0.449	socket length to pupil diameter conversion factor	current study
	k	0.035	photoreceptor absorption coefficient (μm^{-1})	[98] via [7]
	l	57	photoreceptor length (μm)	[1]
	d	3	photoreceptor diameter (μm)	[14] via [1]
	R	1.96	95% confidence level for firing threshold	[99] via [1]
	T	0.1	target width (diameter for circular objects) (m)	
	C_0	-1	object/target contrast (Weber contrast)	
	D	[1 25]	range of pupil diameters used in calculations (mm)	current study
Aerial Vision Model, All	$\mathtt{X}$	0.08	dark noise rate @23.5° C (photoisomerizations per rod s^{-1})	[10]
	$\sigma(\lambda_{\mu m})$	$(0.0011\lambda_{\mu m}^{-4} + 0.008\lambda_{\mu m}^{-2.09})/1 \times 10^3$	extinction factor (m^{-1})	[4]
	$\bar{\beta}$	1.47×10^{15}	intensity parameter coefficient	[8] via [9]
Aerial Vision Model, Daylight	η	0.5	detection efficiency	[100]
	Δt	0.27	integration time (s)	[101]
	F	8.8	F-number, ratio of focal length and pupil diameter	[9]
	L	10^3	daylight luminance (cd m^{-2})	[4]
Aerial Vision Model, Moonlight	η	0.36	detection efficiency	[1]
	Δt	2.40	integration time (s)	[101]
	F	2.1	F-number, ratio of focal length and pupil diameter	[102]
	L	10^{-2}	moonlight luminance (cd m^{-2})	[4]
Aerial Vision Model, Starlight	η	0.36	detection efficiency	[1]
	Δt	5.75	integration time (s)	[101]
	F	2.1	F-number, ratio of focal length and pupil diameter	[102]
	L	10^{-4}	starlight luminance (cd m^{-2})	[4]
Aquatic Vision Model	η	0.36	detection efficiency	[1]
	Δt	1.16	integration time (s)	[101] via [1]
	F	1.275	F-number, ratio of focal length and pupil diameter, based on Matthiessen's ratio (2.55)	[1]
	$c(\lambda)$	$c(\lambda) = b(\lambda) + a(\lambda)$	beam attenuation coefficient (m^{-1})	[4]
	$\mathtt{X}$	0.011	dark noise rate @16.5° C (photoisomerizations per rod s^{-1})	[10]

Supplementary table 1. Parameters for visual ecology calculations

Parameter	Original Value		Alternative Value		$\underset{D\in[1,25]}{\text{ext}}\{\%\Delta r(D)\}$		$\underset{D\in[1,25]}{\text{ext}}\left\{\%\Delta \frac{dr(D)}{dD}\right\}$		$\underset{D\in[1,25]}{\text{ext}}\{\%\Delta V(D)\}$		$\underset{D\in[1,25]}{\text{ext}}\left\{\%\Delta \frac{dV(D)}{dD}\right\}$		References
	Aquatic	Aerial	Aquatic	Aerial	Aquatic	Aerial	Aquatic	Aerial	Aquatic	Aerial	Aquatic	Aerial	
$\mathtt{X}$ (photoisomerizations per rod s^{-1})	0.011 @16.5 °C	0.08 @23.5 °C	0.08 @23.5 °C	0.011 @16.5 °C	-1.5%	-6.8%	-13.1%	-7.4%	-4.5%	-19.1%	-13.9%	-19.4%	[10]
η	0.36	0.5	0.5	0.3	+1.8%	-12.4%	-12.8%	-15.9%	+5.4%	-32.9%	-1.7%	-33.9%	[9, 44]
Δ t (s)	1.16	0.27	0.0116		-24.5%	-6.8%	-16.3%	-11.2%	-57.0%	-19.0%	-51.9%	-19.5%	[44]
			1.6		+1.8%	+28.9%	-12.9%	+42.0%	+5.3%	+113.9%	-10.8%	+135.0%	[44]
d (μm)	3		10		-1.5%	-31.8%	-13.1%	-34.1%	-4.5%	-68.3%	-13.9%	-69.3%	[84]
F	1.275	8.8	1.5		-1.5%	-12.4%	-13.1%	-16.0%	-4.5%	-32.9%	-13.9%	-33.9%	[44]
K_t	$\Psi(D,T,r,L)$		+15%		-51.6%	-12.5%	-101.3%	-16.0%	-88.7%	-32.9%	-100.3%	-33.9%	[45]

Supplementary table 2. Definition: $\underset{i\in[a,b]}{\text{ext}}\{x(i)\} := \text{sgn}(x(i)) \max_{i\in[a,b]}\{\text{abs}(x(i))\}$**. Alternative values for select parameters and their effect on the results of the computational model (visual range, derivative of visual range, visual volume, derivative of visual volume), given as the extrema (maximum/minimum) in percentage change for each parameter across all pupil sizes for aquatic daylight upward viewing, and aerial daylight viewing conditions. The parameters that were chosen to vary are dark noise ($\mathtt{X}$), efficiency (η), integration time (Δ t), photoreceptor diameter (d), F-number (F), and contrast threshold value (K_t). The entire function ($K_t = \Psi(D,T,r,L)$) was shifted in y-axis by the given perturbation percentage.**

	Water Type				
	Clear	**Absorption Dominated**	**Baseline River**	**High Turbidity**	**Scattering Dominated**
Concentration parameters					
Chlorophyll-*a*, mg/m^3	0.50	0.20	0.50	3.00	0.20
"brown earth" mineral particles, g/m^3	0.50	0.20	2.00	2.00	5.00
CDOM absorption, 1/m at 440 nm	0.20	10.00	0.50	0.50	0.10
IOPs at 575 nm					
a, 1/m	0.25	1.65	0.35	1.00	0.31
b, 1/m	0.60	0.27	1.84	2.22	4.25
c, 1/m	0.86	1.92	2.19	3.22	4.56
Attenuation length (1/*c*), m	1.17	0.52	0.46	0.31	0.22
ω_o	0.70	0.14	0.84	0.83	0.93
Secchi depth, m	5.92	2.15	2.73	0.35	1.15

Supplementary table 3. Parameters for the primary water model (Baseline River) reported in study, as well as four other water types tested for sensitivity analysis. Inherent optical properties (IOPs) at the wavelength of maximal transparency of the Baseline River water, 575 nm, are shown: absorbtion (a), scattering (b), and their sum (beam attenuation coefficient), (c). ω_o is the albedo of single scattering. Secchi depth computed according to[103].

#	Aquatic Condition	Aerial Condition	Aquatic-Aerial Range Multiplier	Aquatic-Aerial Range Derivative Multiplier	Aquatic-Aerial Volume Multiplier	Aquatic-Aerial Volume Derivative Multiplier
1	Daylight 8 m depth, horizontal viewing, Finned tetrapod pupil	Daylight, Finned tetrapod pupil	73	536	197,327	1,399,771
2	Daylight 8 m depth, horizontal viewing, Finned tetrapod pupil	Daylight, Digited tetrapod pupil	158	393	1,978,002	4,747,605
3	Daylight 8 m depth, horizontal viewing, Digited tetrapod pupil	Daylight, Digited tetrapod pupil	143	1,146	1,476,289	11,737,795
4	Daylight 8m depth, upward viewing, Finned tetrapod pupil	Daylight, Finned tetrapod pupil	47	376	53,371	409,071
5	Daylight 8m depth, upward viewing, Finned tetrapod pupil	Daylight, Digited tetrapod pupil	102	275	534,994	1,387,447
6	Daylight 8m depth, upward viewing, Finned tetrapod pupil	Moonlight, Finned tetrapod pupil	20	191	4,283	42,372
7	Daylight 8m depth, upward viewing, Finned tetrapod pupil	Starlight, Finned tetrapod pupil	10	100	504	5,659
8	Daylight 8m depth, upward viewing, Finned tetrapod pupil	Moonlight, Digited tetrapod pupil	51	156	65,451	193,988
9	Daylight 8m depth, upward viewing, Finned tetrapod pupil	Starlight, Digited tetrapod pupil	27	99	10,327	36,543
10	Daylight 8m depth, upward viewing, Finned tetrapod pupil	Moonlight, Finned tetrapod pupil	46	217	50,605	260,812
11	Moonlight 8m depth, upward viewing, Finned tetrapod pupil	Moonlight, Digited tetrapod pupil	116	177	773,350	1,194,053
12	Moonlight 8m depth, upward viewing, Finned tetrapod pupil	Starlight, Finned tetrapod pupil	36	126	79,262	34,835
13	Starlight 8m depth, upward viewing, Finned tetrapod pupil	Starlight, Digited tetrapod pupil	98	125	1,624,793	224,934

Supplementary table 4. The aquatic to aerial range, derivative of range, volume and derivative of volume multipliers for various combinations of pupil size and illumination conditions.

Taxon	Group	Orbit Length (mm)	Skull Length (mm)	Orbit/Skull, %	Reference
Beelarongia patrichae	Finned	8	95	8	[104]
Bruehnopteron murphyi	Finned	11	57	20	[105]
Cabonnichthys burnsi	Finned	6	87	7	[106]
Canowindra grossi	Finned	6	74	8	[107]
Cladarosymblema narrienense	Finned	12	84	14	[108]
Edenopteron kiethcrooki	Finned	37	302	12	[109]
Elpistostege watsoni	Finned	16	179	9	[110]
Eusthenopteron foordi	Finned	11	72	15	[111]
Gogonasus andrewsae	Finned	7	46	15	[112]
Gooloogongia loomesi	Finned	26	124	21	[113]
Gyroptychius milleri	Finned	7	52	13	[114]
Heddleichthys dalgleisiensis	Finned	9	64	14	[115]
Koharalepis jarviki	Finned	8	116	7	[116]
Mandageria fairfaxi	Finned	21	263	8	[117]
Marsdenichthys longioccipitus	Finned	6	42	15	[118]
Osteolepis macrolepidotus	Finned	6	33	19	[119]
Palatinichthys laticeps	Finned	15	86	17	[120]
Panderichthys rhombolepis	Finned	32	251	13	[121]
Screbinodus ornatus	Finned	17	137	13	[122]
Tiktaalik roseae	Finned	24	168	15	[18]
Tinirau clackae	Finned	24	192	12	[123]
Acanthostega gunnari	Digited	21	107	20	[71, 124]
Acherontiscus caledoniae	Digited	2	16	15	[125]
Adamanterpeton ohioensis	Digited	104	590	18	[126]
Adelogyrinus simnorhynchus	Digited	9	42	21	[127]
Adelospondylus watsoni	Digited	13	67	19	[128]
Anthracosaurus russelli	Digited	70	299	23	[129]
Archeria crassidisca	Digited	29	154	19	[15]
Balanerpeton woodi	Digited	14	40	34	[130]
Baphetes bohemicus	Digited	33	175	19	[131]
Baphetes kirkbyi	Digited	40	277	15	[131]
Baphetes lintonensis	Digited	14	71	20	[131]
Baphetes orientalis	Digited	16	69	24	[69]
Chenoprosopus lewisi	Digited	18	91	19	[132]
Chenoprosopus milleri	Digited	32	284	11	[133]
Cochleosaurus bohemicus	Digited	27	204	13	[134]
Colosteus scutellatus	Digited	11	89	12	[135]
Crassigyrinus scoticus	Digited	50	217	23	[136]
Deltaherpeton hiemstrae	Digited	25	133	19	[137]
Dendrerpeton acadianum	Digited	18	88	20	[138]
Edops craigi	Digited	50	515	10	[139]
Eoherpeton watsoni	Digited	29	136	21	[140]
Eucritta melanolimnetes	Digited	23	66	35	[141]
Gephyrostegus bohemicus	Digited	5	17	33	[72]
Greererpeton burkemorani	Digited	24	153	15	[142]
Ichthyostega	Digited	29	140	21	[142]
Kyrinion martilli	Digited	64	232	27	[143]
Loxomma acutirhinus	Digited	41	247	17	[131]
Megalocephalus pachycephalus	Digited	42	313	13	[131]
Nigerpeton ricqlesi	Digited	49	487	10	[144]
Ossinodus pueri	Digited	60	274	22	[145, 146]
Pederpes finneyae	Digited	29	140	20	[147]
Pholiderpeton attheyi	Digited	46	331	14	[148]
Pholiderpeton scutigerum	Digited	47	281	17	[149]
Proterogyrinus scheelei	Digited	36	128	28	[150]
Silvanerpeton miripedes	Digited	26	72	37	[151]
Spathicephalus mirus	Digited	41	190	22	[152]
Ventastega curonica	Digited	35	170	21	[153]
Whatcheeria deltae	Digited	22	96	22	[154]

Supplementary table 5. Finned and digited tetrapods included in this study

Taxon	OM (mm)	ED (mm)	PD (mm)	taxon	OM (mm)	ED (mm)	PD (mm)
Acanthurus bahianus	6.58	6.91	2.70	*Paranthias furcifer*	7.72	7.97	3.65
Acanthurus coeruleus	7.75	7.94	2.86	*Parapercis millepunctata*	4.50	4.43	1.37
Apogon maculatus	7.18	7.78	3.81	*Pempheris schomburgki*	14.58	14.70	7.23
Apogon melas	7.75	8.57	3.97	*Pomacanthus paru*	7.78	7.86	3.33
Bothus ocellatus	6.40	6.35	1.11	*Prionurus microlepidotus*	8.75	8.73	4.44
Caesio teres	11.05	11.11	5.08	*Pseudanthias bartlettorum*	4.08	4.57	1.87
Cephalopholis miniata	6.65	6.82	3.17	*Pseudanthias evansi*	3.75	4.51	1.87
Cephalopholis polleni	8.40	8.57	3.33	*Pseudanthias fasciatus*	7.50	7.78	3.49
Cephalopholis urodeta	8.45	7.94	3.41	*Pseudanthias hutchii*	5.15	5.31	2.42
Cheilinus chlorourus	7.90	7.78	2.38	*Pseudanthias pleurotaenia*	5.83	6.43	2.90
Cheilinus fasciatus	7.85	7.94	2.86	*Pseudanthias squamipinnis*	5.55	6.41	2.68
Cirrhitichthys oxycephalus	4.92	5.13	2.23	*Pseudocheilinus evadinus*	3.76	3.98	1.55
Clepticus parrae	3.95	4.29	1.92	*Pseudogramma gregoryi*	3.20	2.66	1.29
Cromileptes altivelis	7.40	7.78	3.57	*Rypticus maculatus*	5.28	5.63	2.86
Cryptocentrus sp.	4.25	5.55	2.54	*Sargocentron coruscum*	11.65	12.70	5.87
Cyprinocirrhites polyactis	6.08	6.32	2.74	*Sargocentron diadema*	10.55	11.35	4.84
Diplectrum formosum	11.15	10.79	4.13	*Sargocentron vexillarium*	10.00	10.32	4.60
Epibulus insidiator	6.10	6.19	2.22	*Scarus iseri*	5.90	6.25	2.31
Epinephelus fulvus	6.63	6.98	3.09	*Serranocirrhites latus*	4.43	4.87	2.01
Epinephelus guttatus	8.90	9.68	4.28	*Serranus annularis*	3.73	4.27	1.77
Epinephelus ongus	7.05	7.56	3.52	*Serranus baldwini*	4.20	4.30	1.88
Gramma loreto	3.53	3.97	1.69	*Serranus chionaraia*	4.08	4.78	2.04
Halichoeres pictus	5.04	5.31	2.04	*Serranus phoebe*	5.50	5.86	2.47
Hemigymnus melapterus	6.15	5.55	2.86	*Serranus tabacarius*	5.72	6.30	2.65
Hypoplectrus chlorurus	9.10	9.20	3.97	*Serranus tigrinus*	5.63	5.77	2.33
Hypoplectrus puella	7.59	7.70	3.33	*Serranus tortugarum*	4.78	4.93	2.25
Hypoplectrus unicolor	8.34	8.97	3.89	*Siganus magnificus*	9.03	9.20	4.44
Inermia vittata	11.00	11.11	4.60	*Siganus puellus*	9.95	10.47	5.24
Labrisomus nuchipinnis	5.77	5.97	2.73	*Siganus tetrazonus*	8.20	8.89	4.28
Liopropoma carmabi	3.30	3.54	1.41	*Siganus unimaculatus*	8.90	8.89	4.44
Liopropoma eukrines	4.10	4.03	1.69	*Sparisoma aurofrenatum*	6.35	6.74	2.47
Liopropoma mowbrayi	3.30	3.62	1.53	*Sparisoma chrysopterum*	5.78	6.31	2.00
Liopropoma rubre	3.42	3.78	1.69	*Sparisoma viride*	6.35	6.68	2.37
Luzonichthys waitei	3.65	3.86	1.61	*Stegastes fuscus*	7.38	7.35	3.17
Neoniphon sammara	11.10	12.70	3.22	*Stegastes leucostictus*	6.85	6.82	3.02
Novaculichthys taeniourus	6.30	6.19	2.70	*Stegastes partitus*	5.18	5.45	2.33
Odontanthias borbonius	9.00	9.68	4.44	*Stegastes variabilis*	4.25	4.60	2.06
Opistognathus aurifrons	8.90	8.89	3.81	*Variola louti*	5.30	5.87	2.54
Oxycirrhites typus	3.98	4.67	2.17	*Zoramia leptacantha*	4.55	4.99	2.62
Paracirrhites arcatus	3.90	4.35	1.93				

Supplementary table 6. Orbit length (OM), eye diameter (ED), and minimum pupil diameter (PD) of teleost fishes included in this study.

5. Supplementary Data

Measured skull images. Annotations: "actual size" refers to size as printed on 215.9 by 279.4 mm (8.5 by 11 in) paper, printed at actual size. Legend for measurement labels: OML - left orbit major axis length; OMR - right orbit major axis length; OM - mean of OML and OMR; PPL - length of skull as defined in Methods; PPW - width of skull at PPL; MHW - maximum skull width; LMH - length of skull at maximum skull width. All units are millimeters. The first appearance datum and last appearance datum for each fossil, based on stratigraphy and converted to absolute time through the International Chronostratigraphic Chart[155], are shown below each taxon name, in millions of years (Ma).

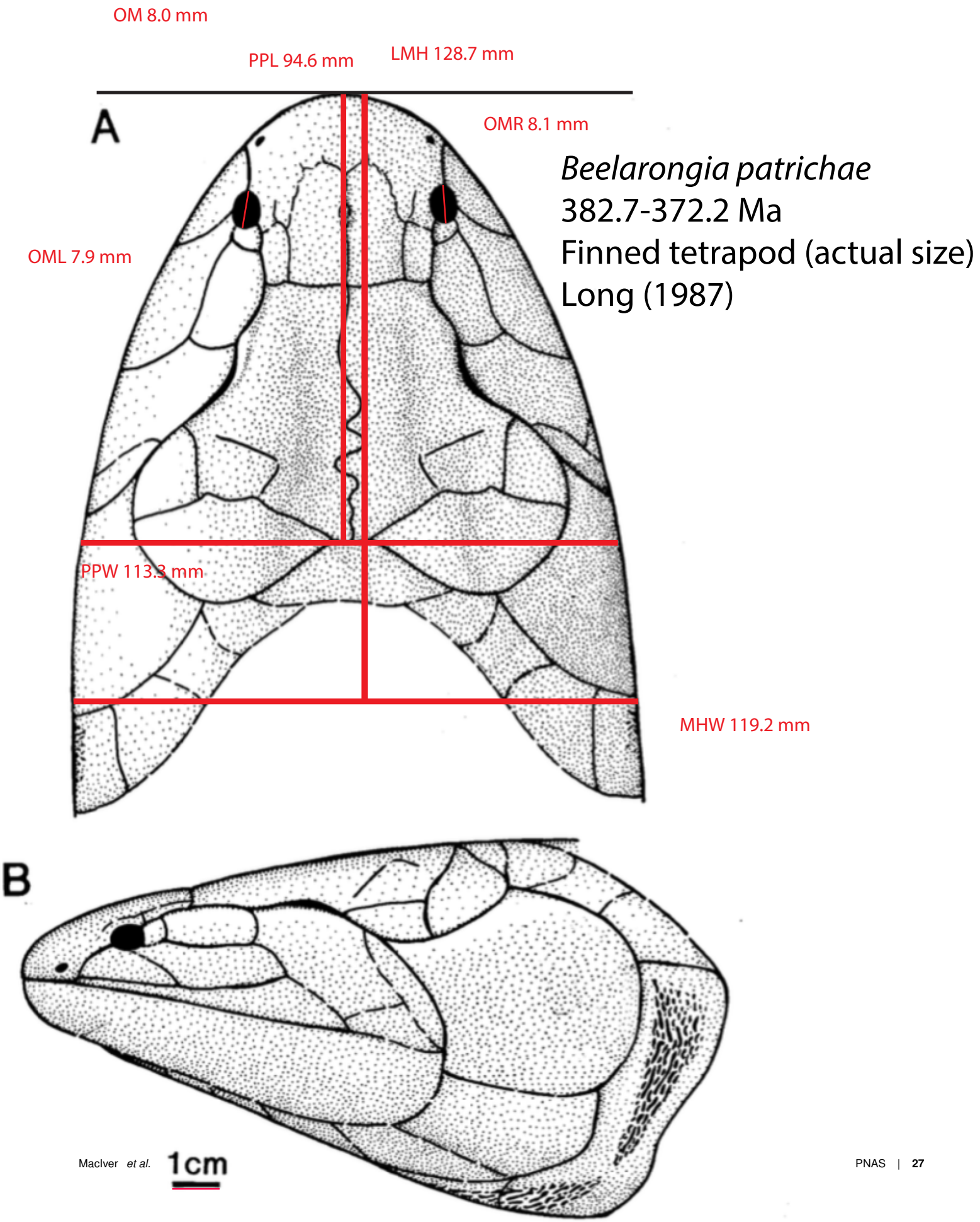
OM 8.0 mm
PPL 94.6 mm
LMH 128.7 mm
A
OMR 8.1 mm
OML 7.9 mm
PPW 113.3 mm
MHW 119.2 mm
Beelarongia patrichae
382.7-372.2 Ma
Finned tetrapod (actual size)
Long (1987)
B
1cm

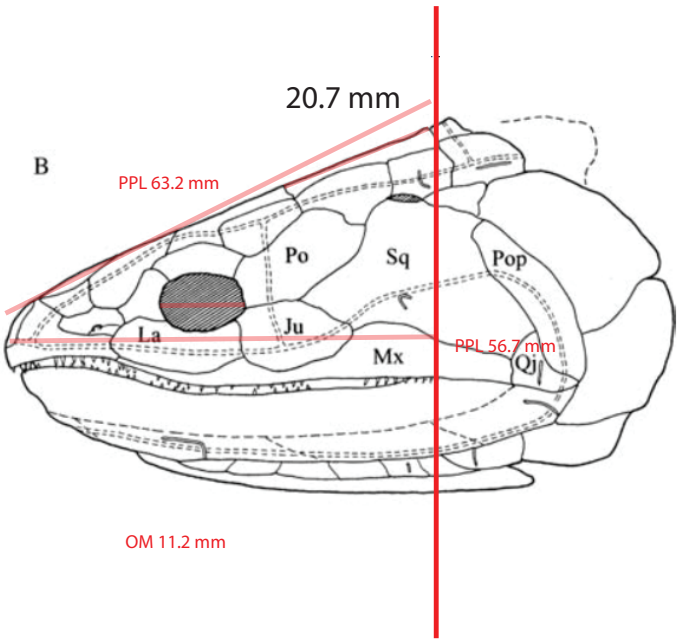

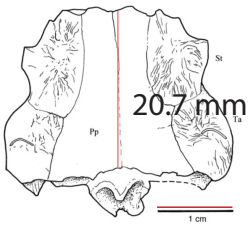

Bruehnopteron murphyi
385.2-382.7 Ma
Finned tetrapod (actual size)
Schultze and Reed (2012)

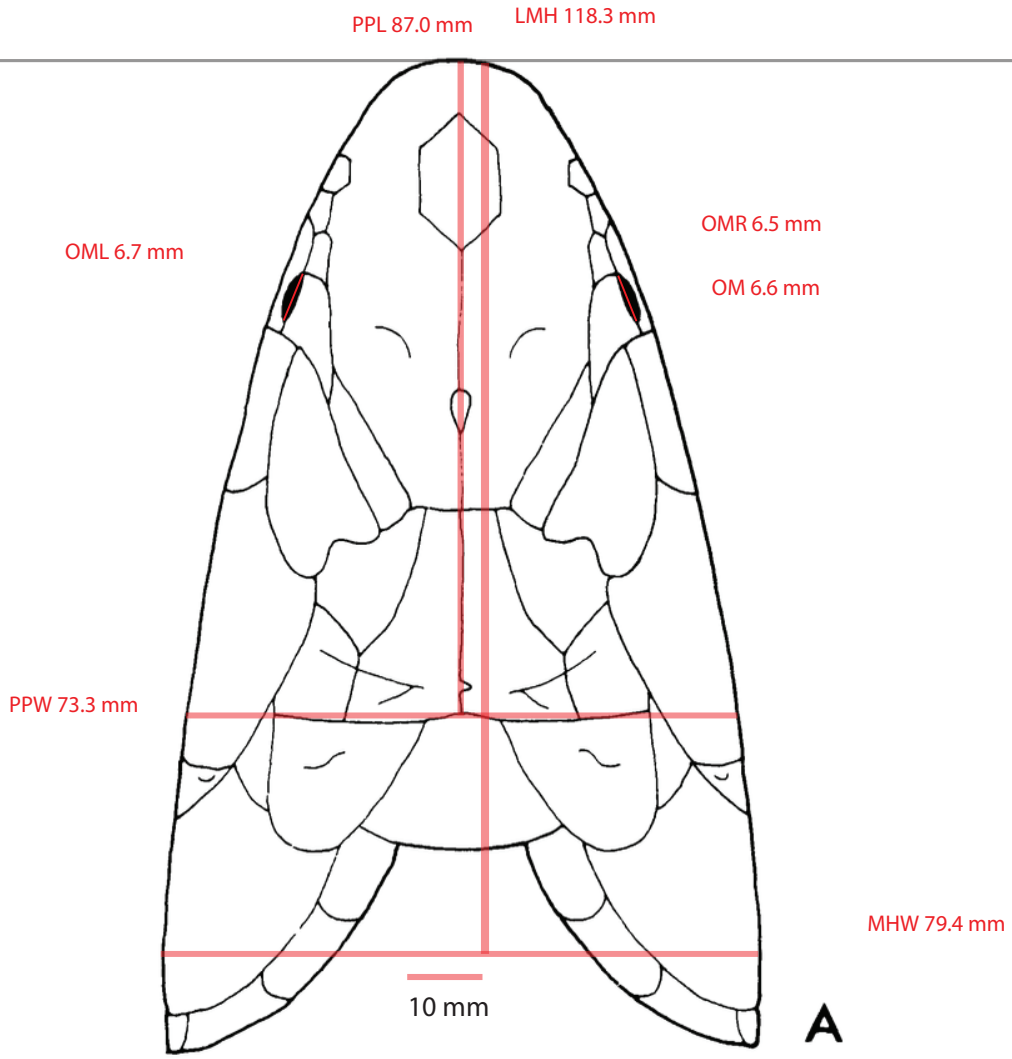

Cabonnichthys burnsi
382.7-358.9 Ma
Finned tetrapod (actual size)
Ahlberg and Johanson (1997)

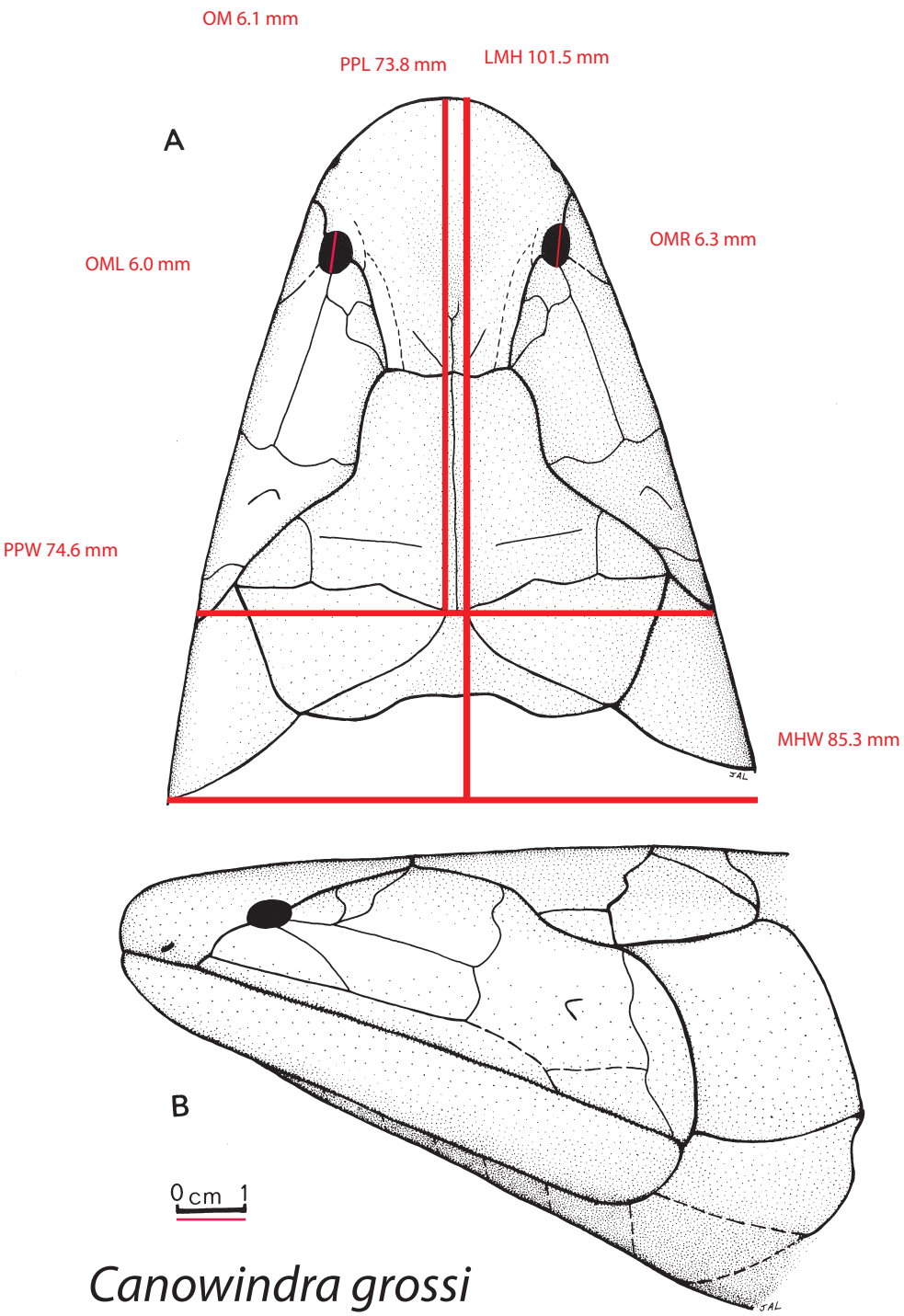

Canowindra grossi
382.7-358.9 Ma
Finned tetrapod (actual size)
Long (1985)

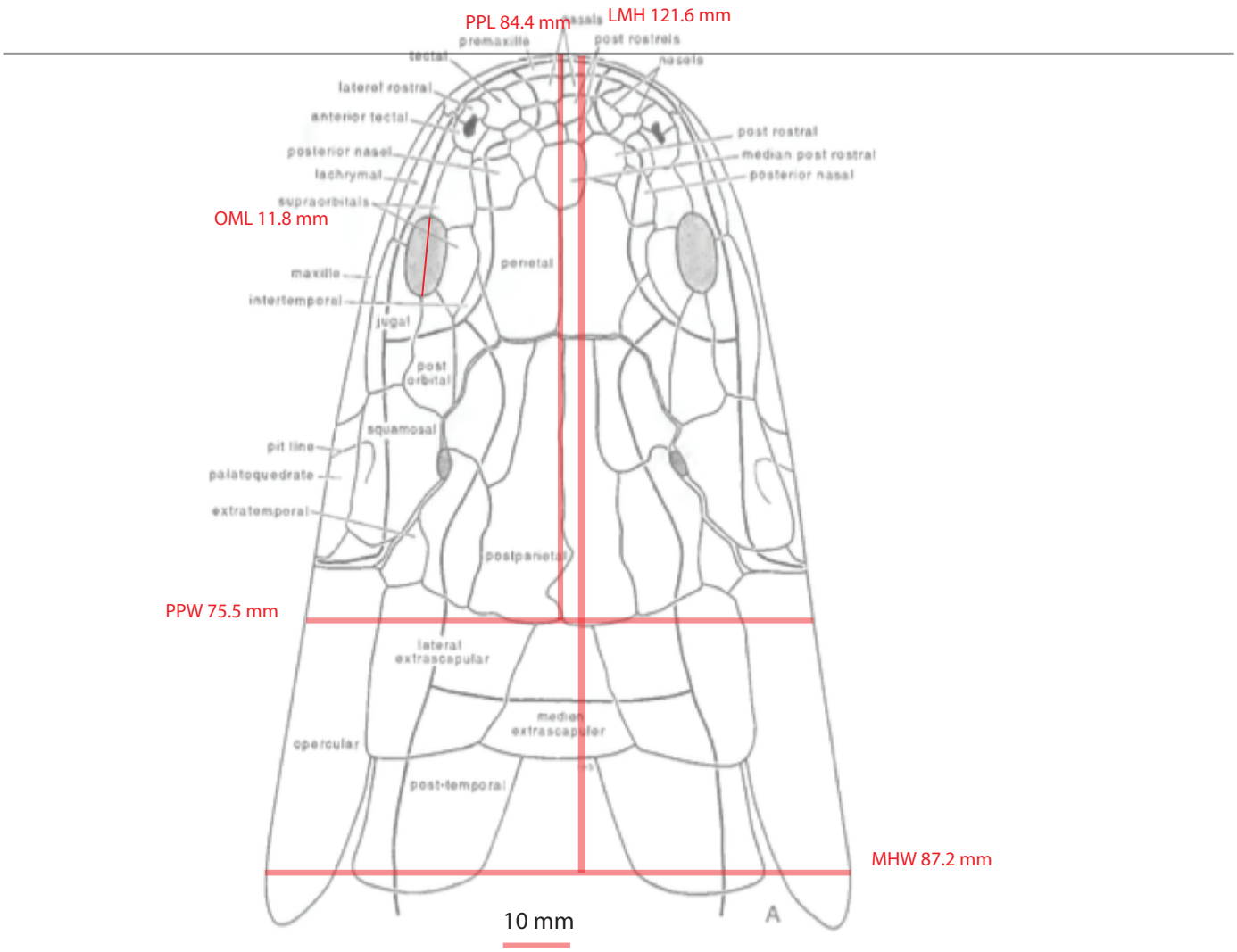

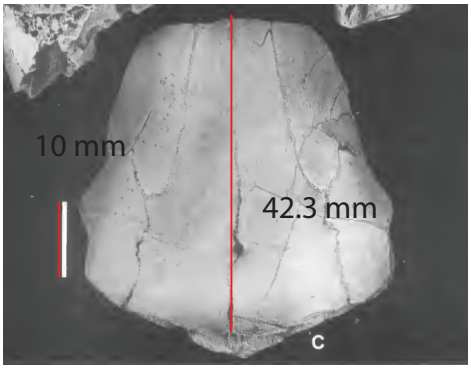

Cladarosymblema narrienense
346.7-341.4 Ma
Finned tetrapod (actual size)
Fox et al. (1995)

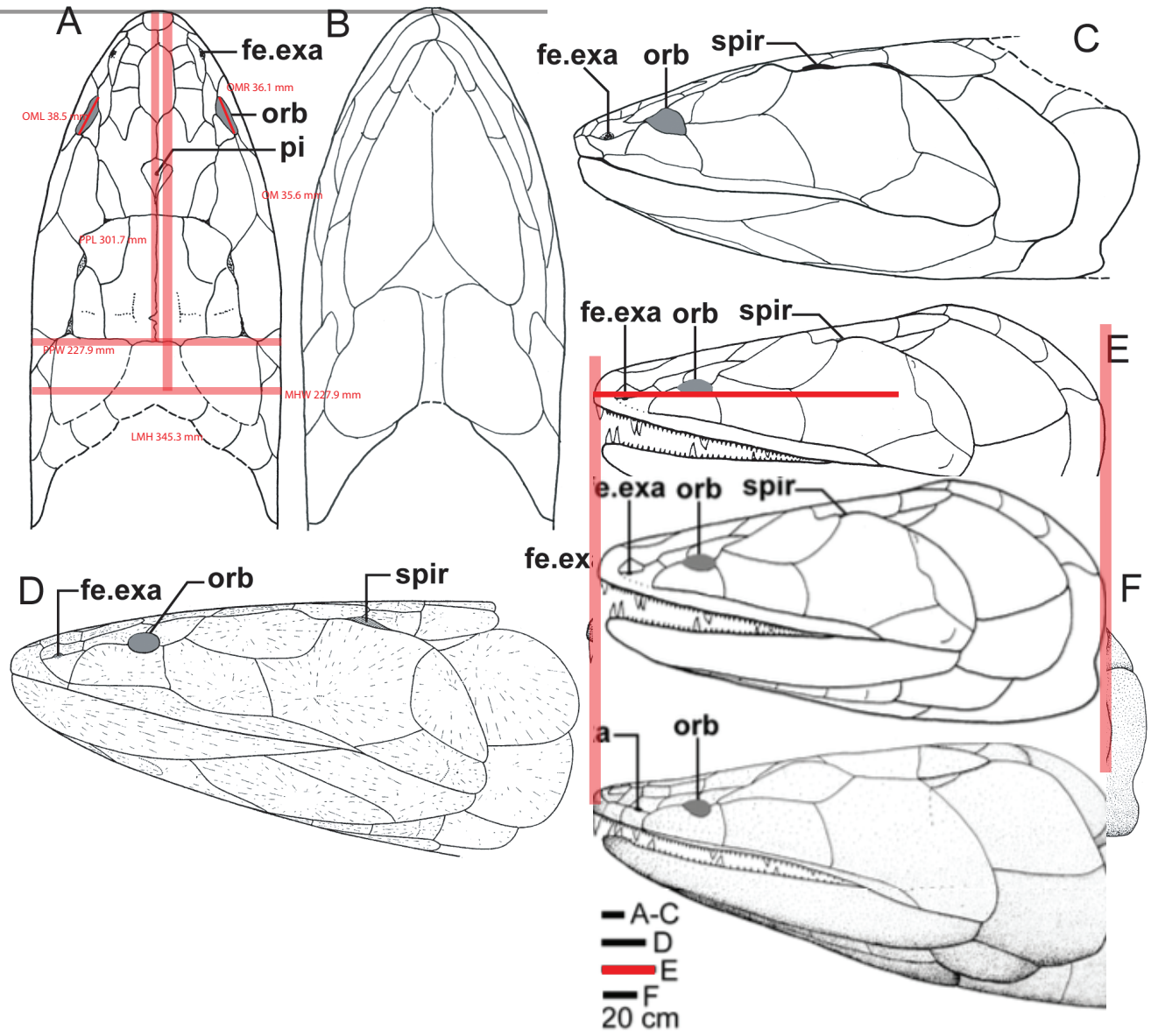

Edenopteron kiethcrooki
363.3-358.9 Ma
Finned tetrapod (scaled 40%)
Young et al. (2013)

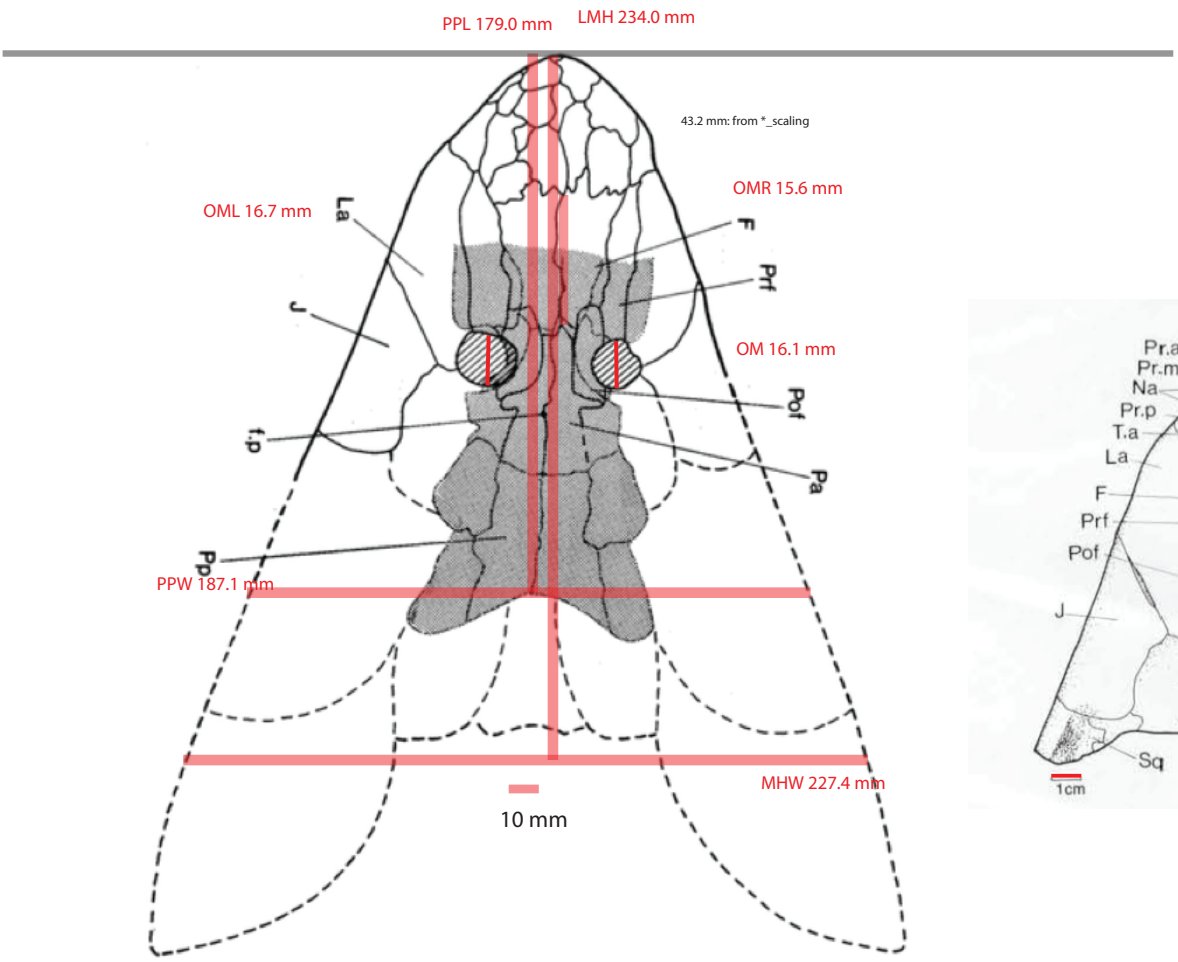

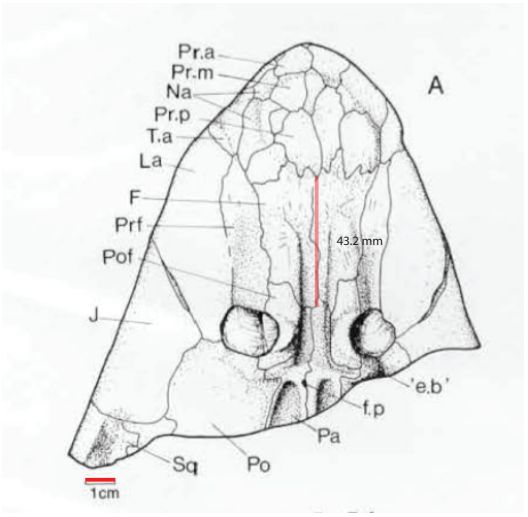

Elpistostege watsoni
379.2-375.7 Ma
Finned tetrapod (scaled 40%)
Schultze and Arsenault (1985)

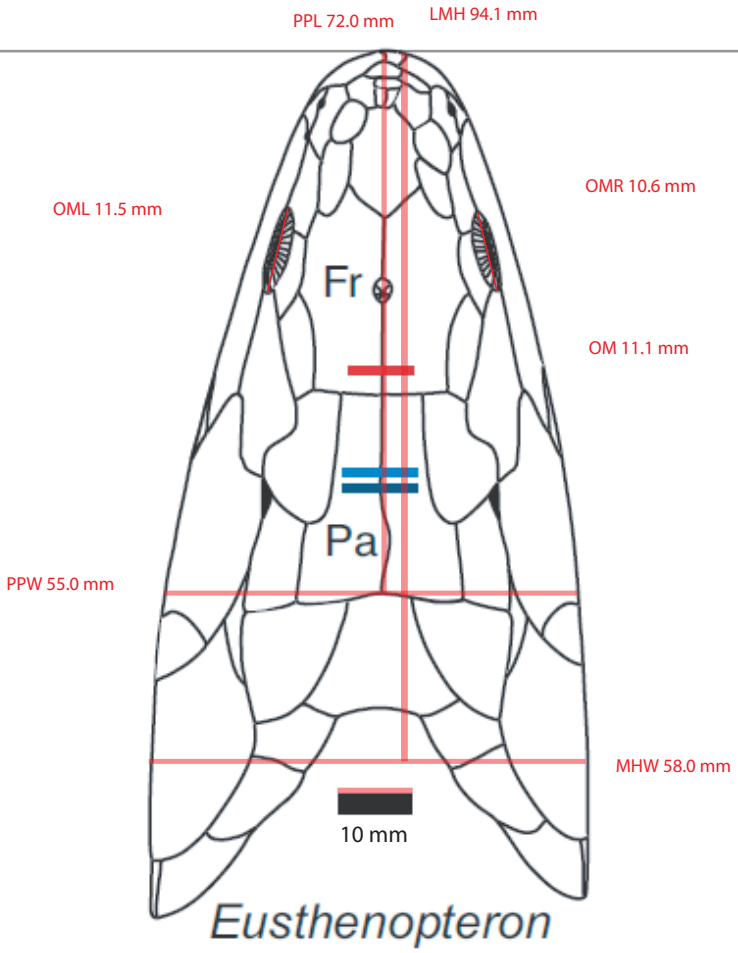

Eusthenopteron foordi
382.7-372.2 Ma
Finned tetrapod (actual size)
Markey and Marshall (2007)

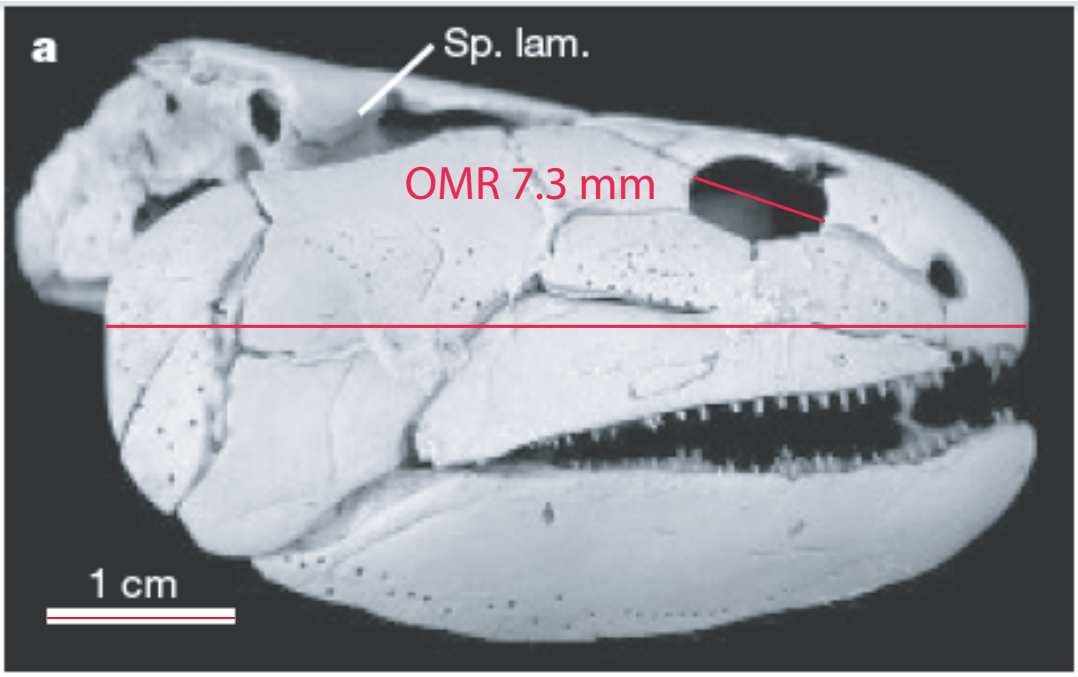

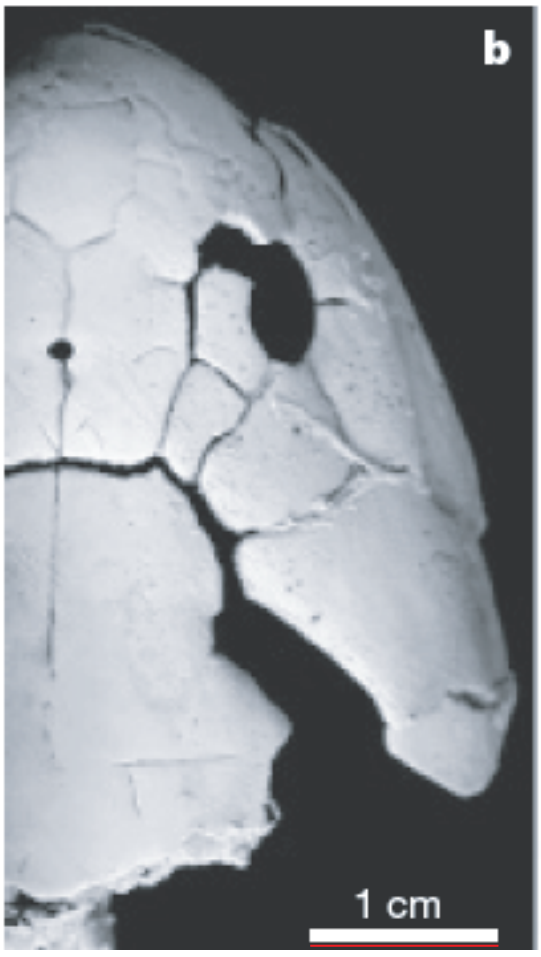

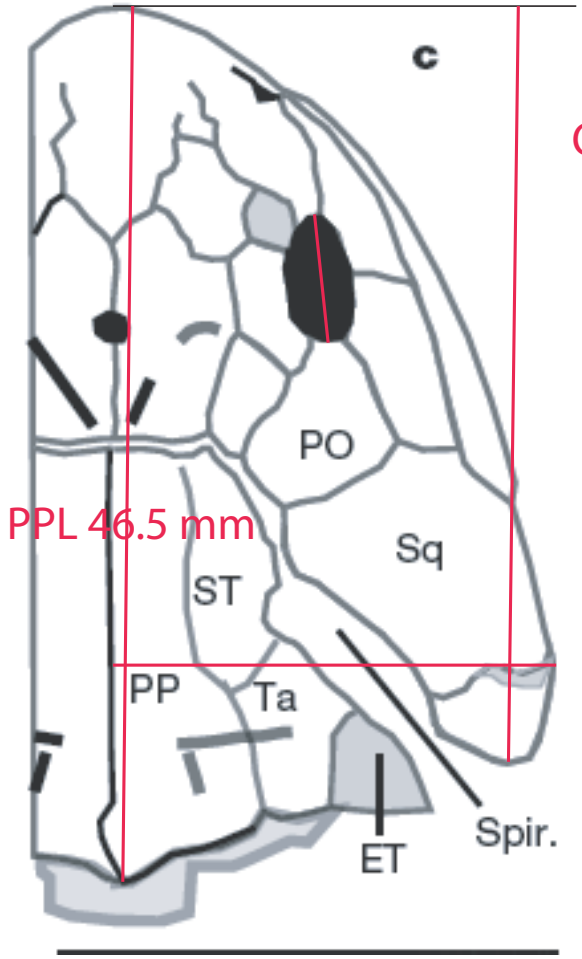

OM 7.0 mm

OMR 6.8 mm

PPL 46.5 mm

PPW 47.1 mm

Gogonasus andrewsae
385.2-379.2 Ma
Finned tetrapod (scaled 250%)
Long et al. (2006)

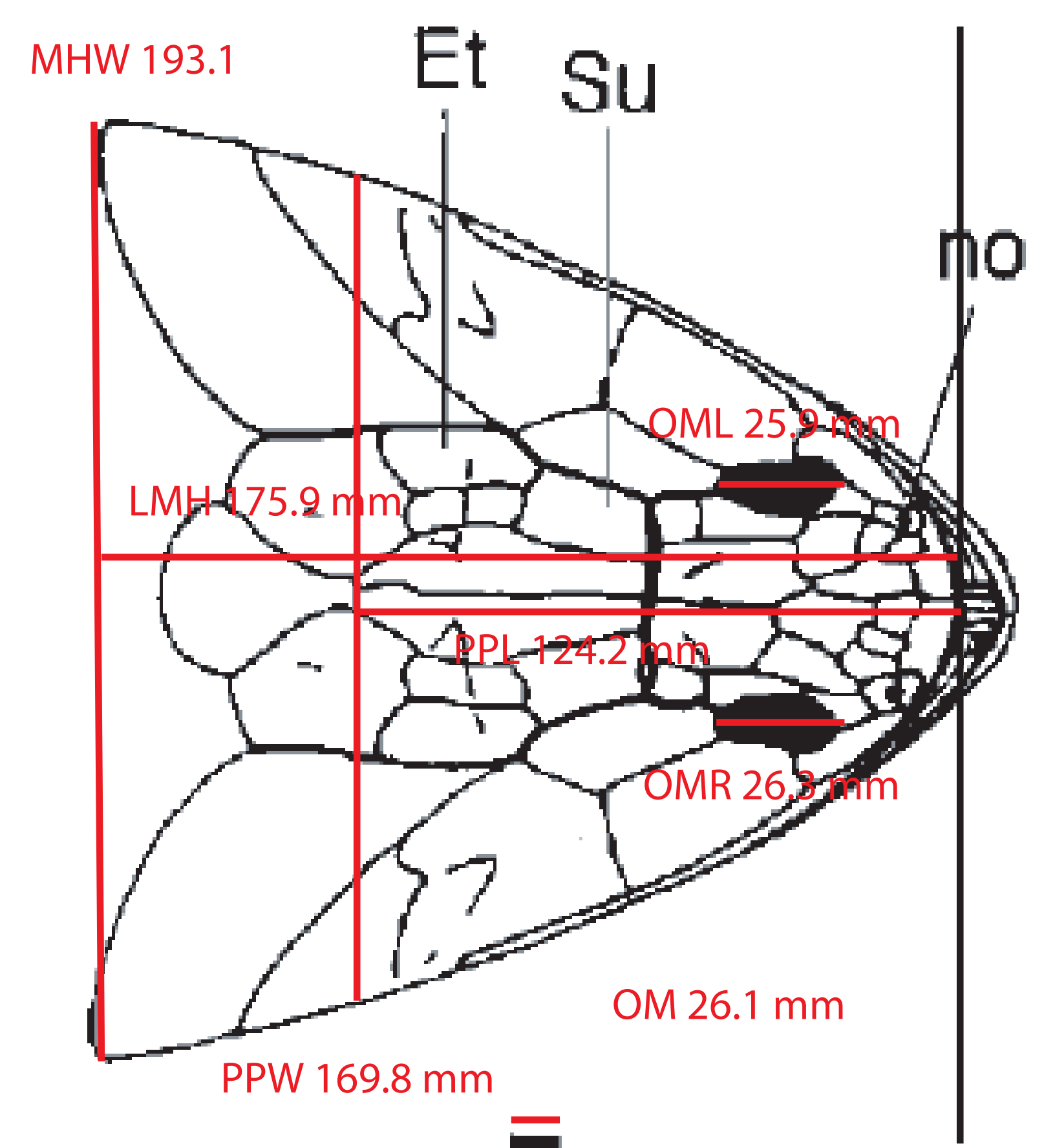

Gooloogongia loomesi
382.7-358.9 Ma
Finned tetrapod (actual size)
Johanson and Ahlberg (1998)

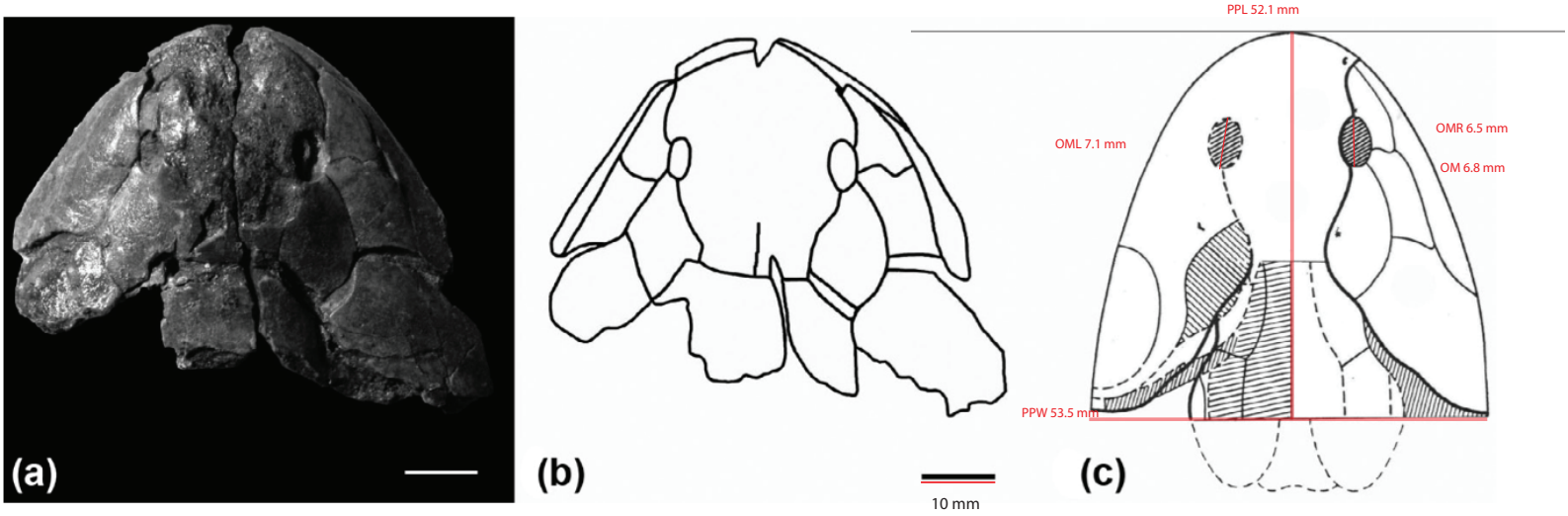

Gyroptychius milleri
387.7-382.7 Ma
Finned tetrapod (actual size)
Newman et al. (2015)

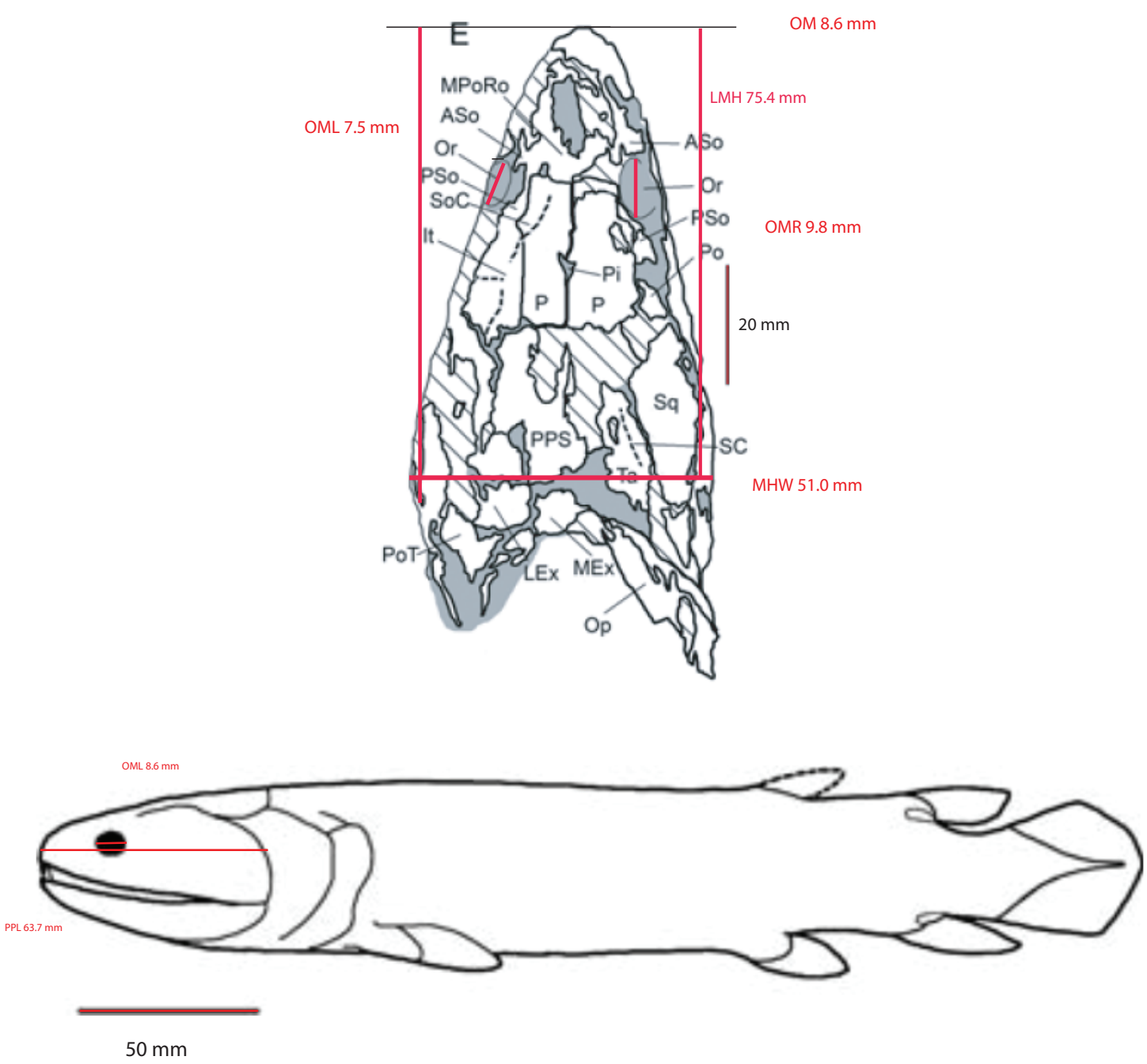

Heddleichthys dalgleisiensis
372.2-358.9 Ma
Finned tetrapod (lateral view scaled 60%, dorsal view actual size)
Snitting (2009)

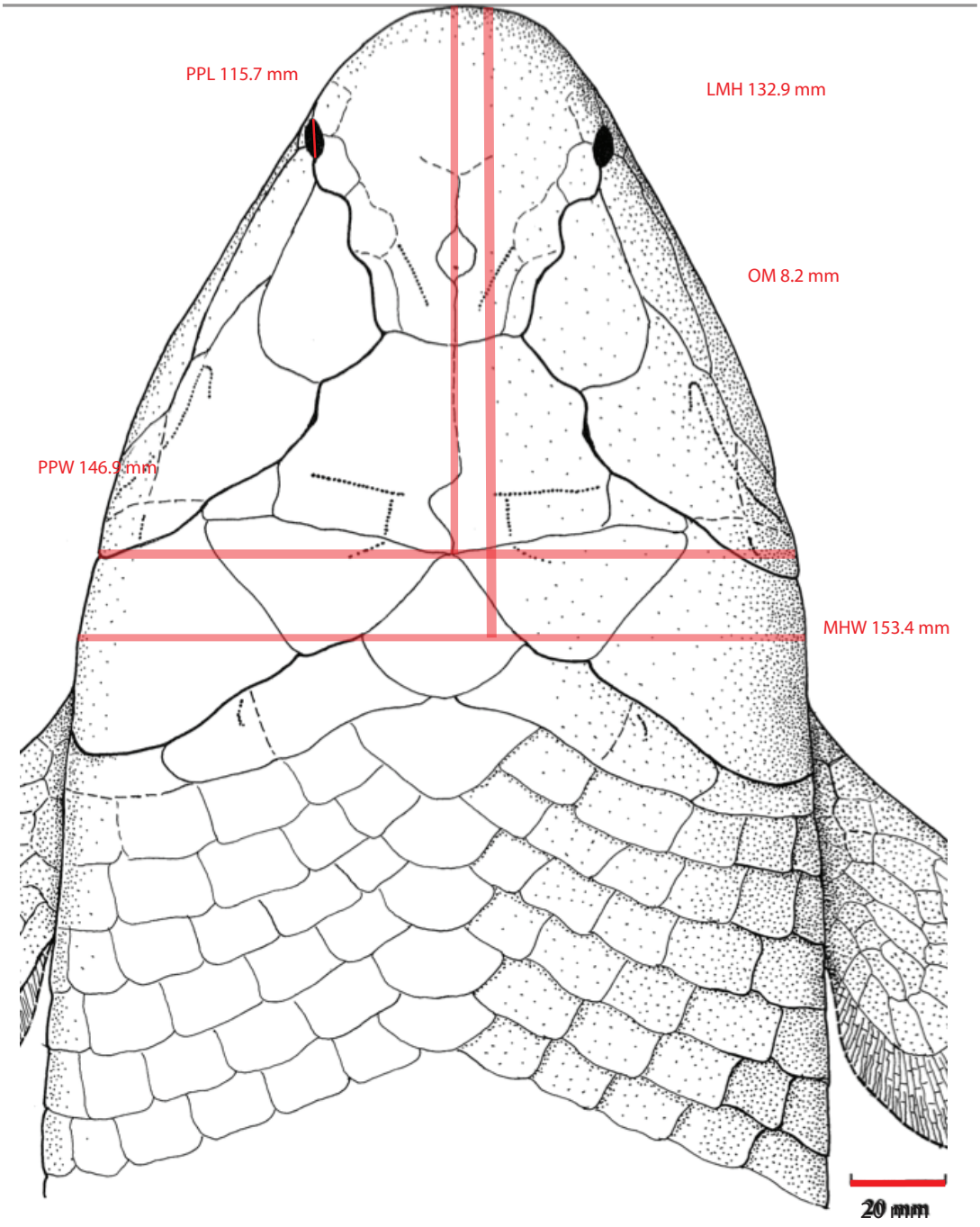

Koharalepis jarviki
387.7-379.2 Ma
Finned tetrapod (scaled 70%)
Young et al. (1992)

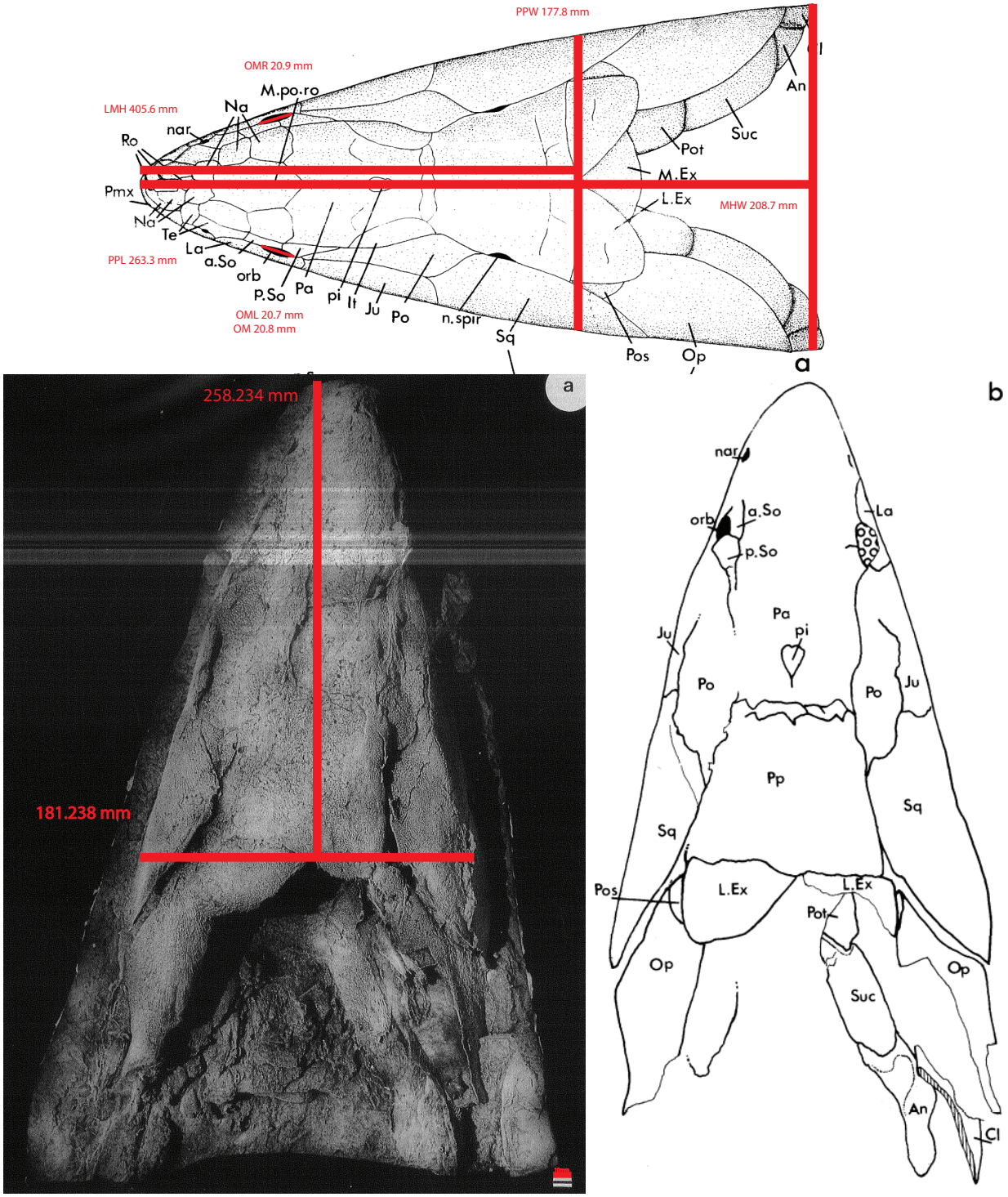

Mandageria fairfaxi
372.2-358.9 Ma
Finned tetrapod (scaled 30%)
Johanson and Ahlberg (1997)

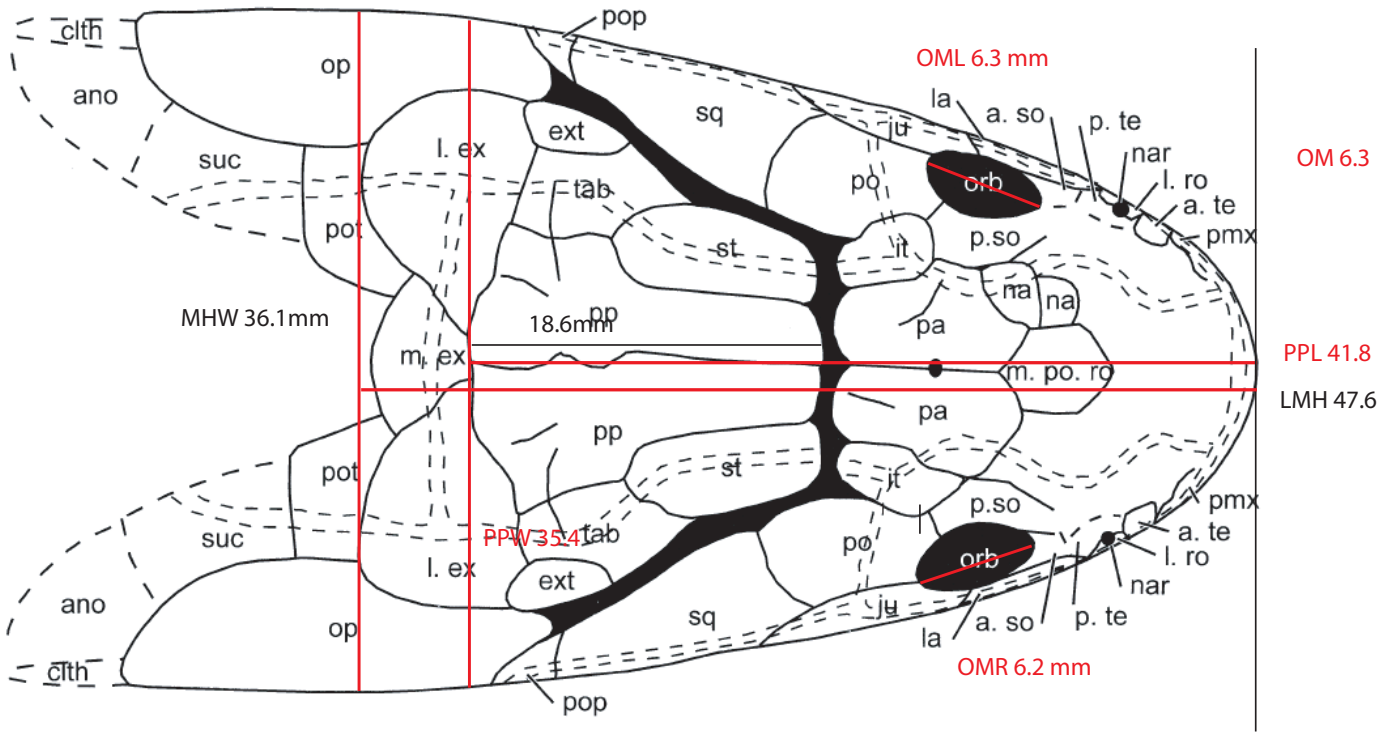

Marsdenichthys longioccipitus
387.7-372.2 Ma
Finned tetrapod (scaled 250%)
Holland et al. (2010)

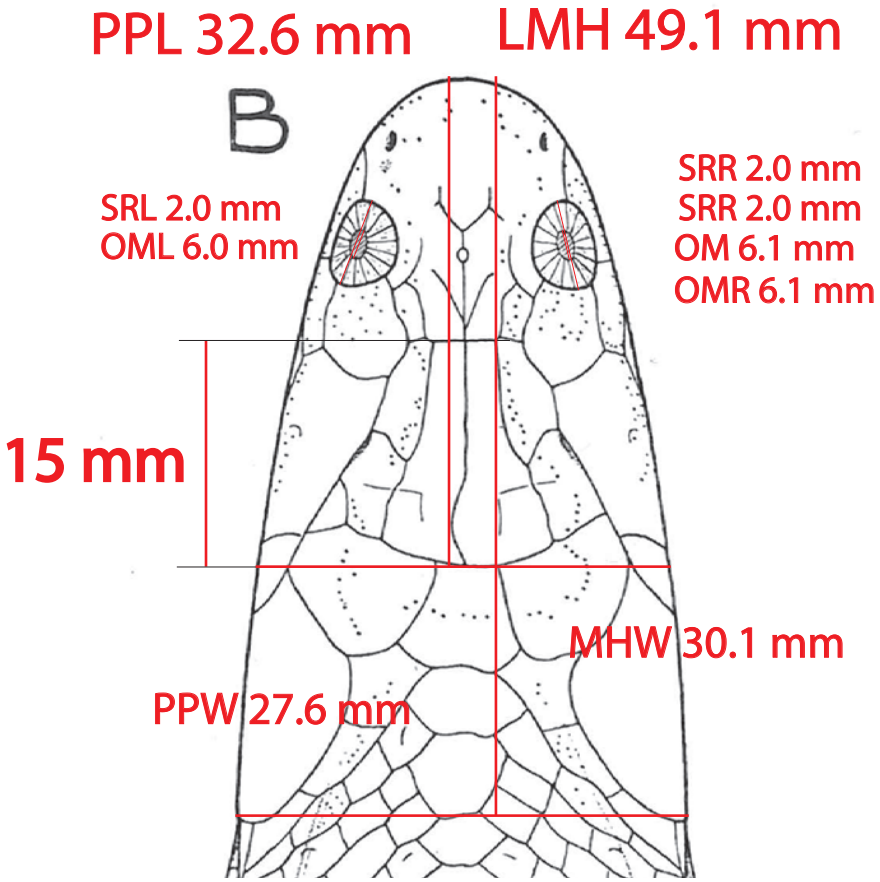

Osteolepis macrolepidotus
393.3-387.7 Ma
Finned tetrapod (scaled 200%)
Jarvik (1948)

OM 14.8 mm PPL 85.5 mm LMH 106.2 mm

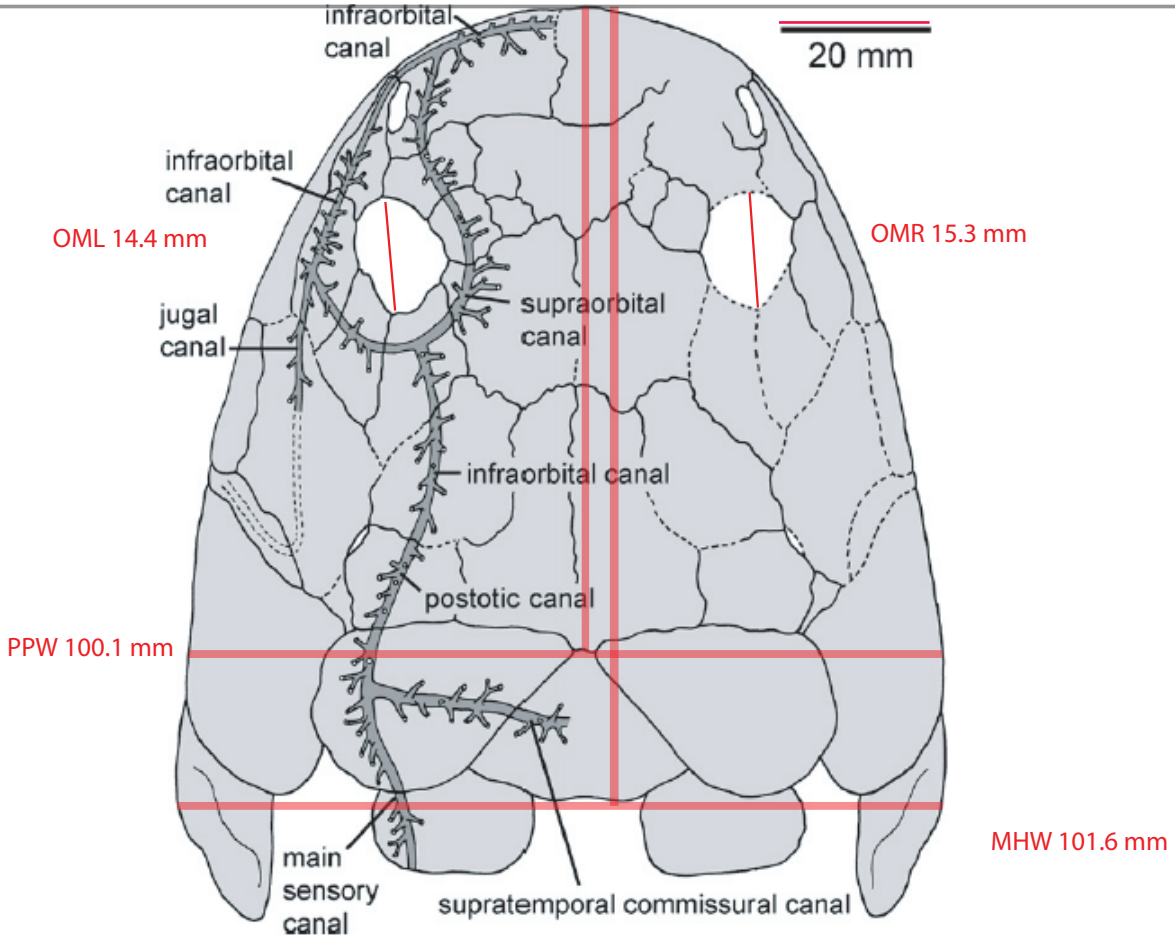

Palatinichthys laticeps
298.9-272.3 Ma
Finned tetrapod (actual size)
Witzmann and Schoch (2012)

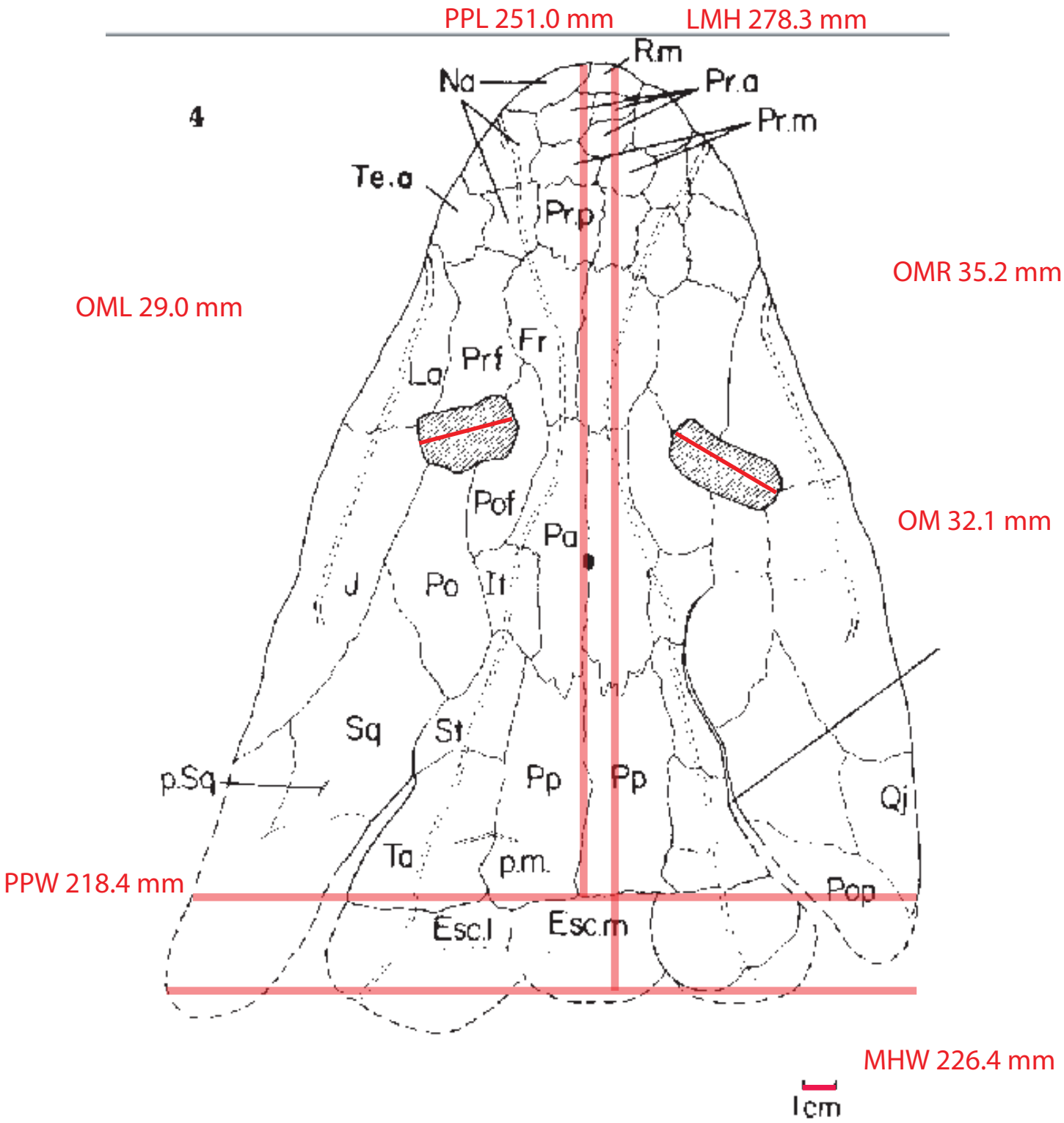

Panderichthys rhombolepis
382.7-372.2 Ma
Finned tetrapod (scaled 60%)
Schultze and Vorobyeva (1991)

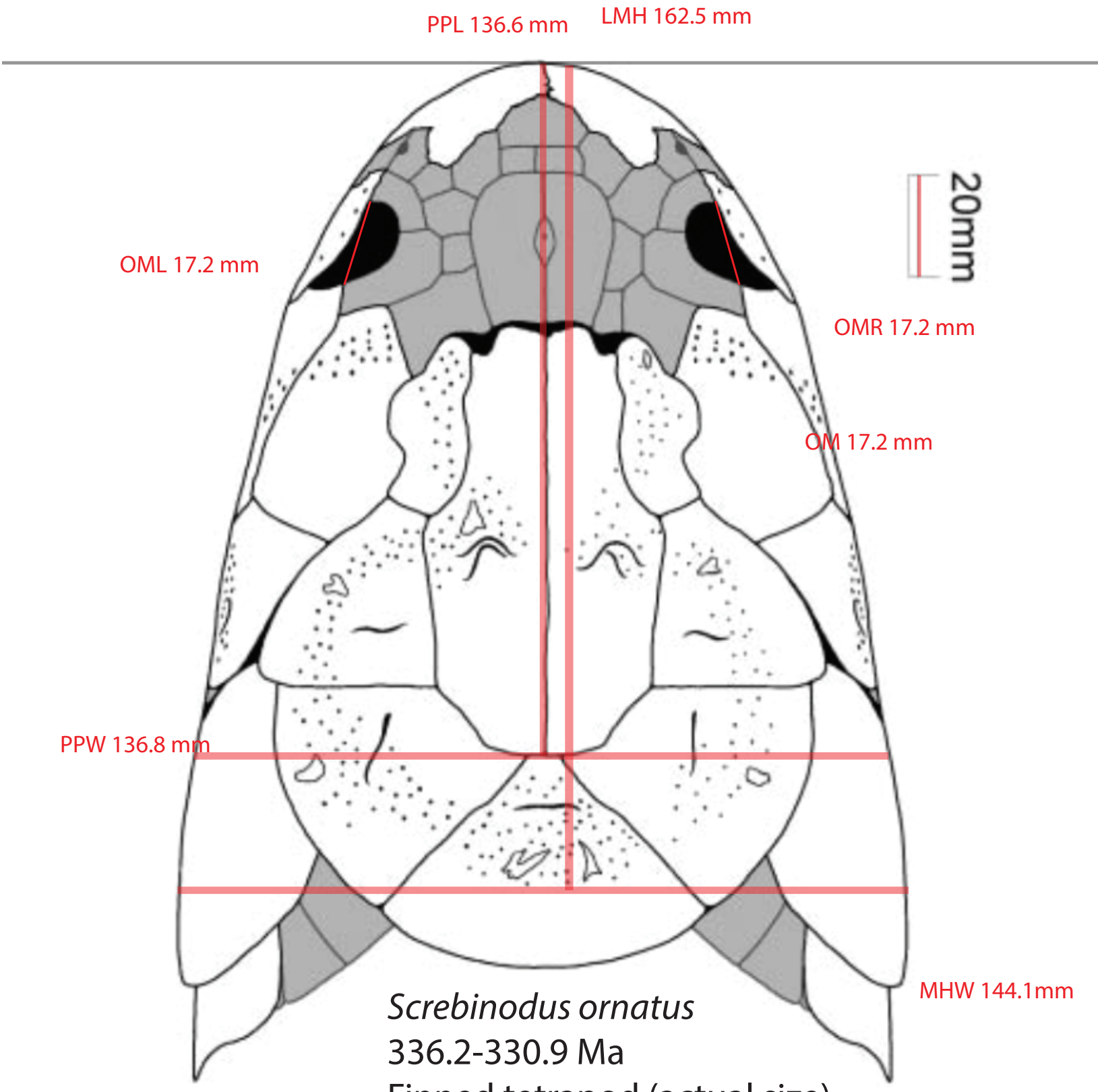
PPL 136.6 mm
LMH 162.5 mm
20mm
OML 17.2 mm
OMR 17.2 mm
OM 17.2 mm
PPW 136.8 mm
MHW 144.1mm
Screbinodus ornatus
336.2-330.9 Ma
Finned tetrapod (actual size)
Jeffery (2012)

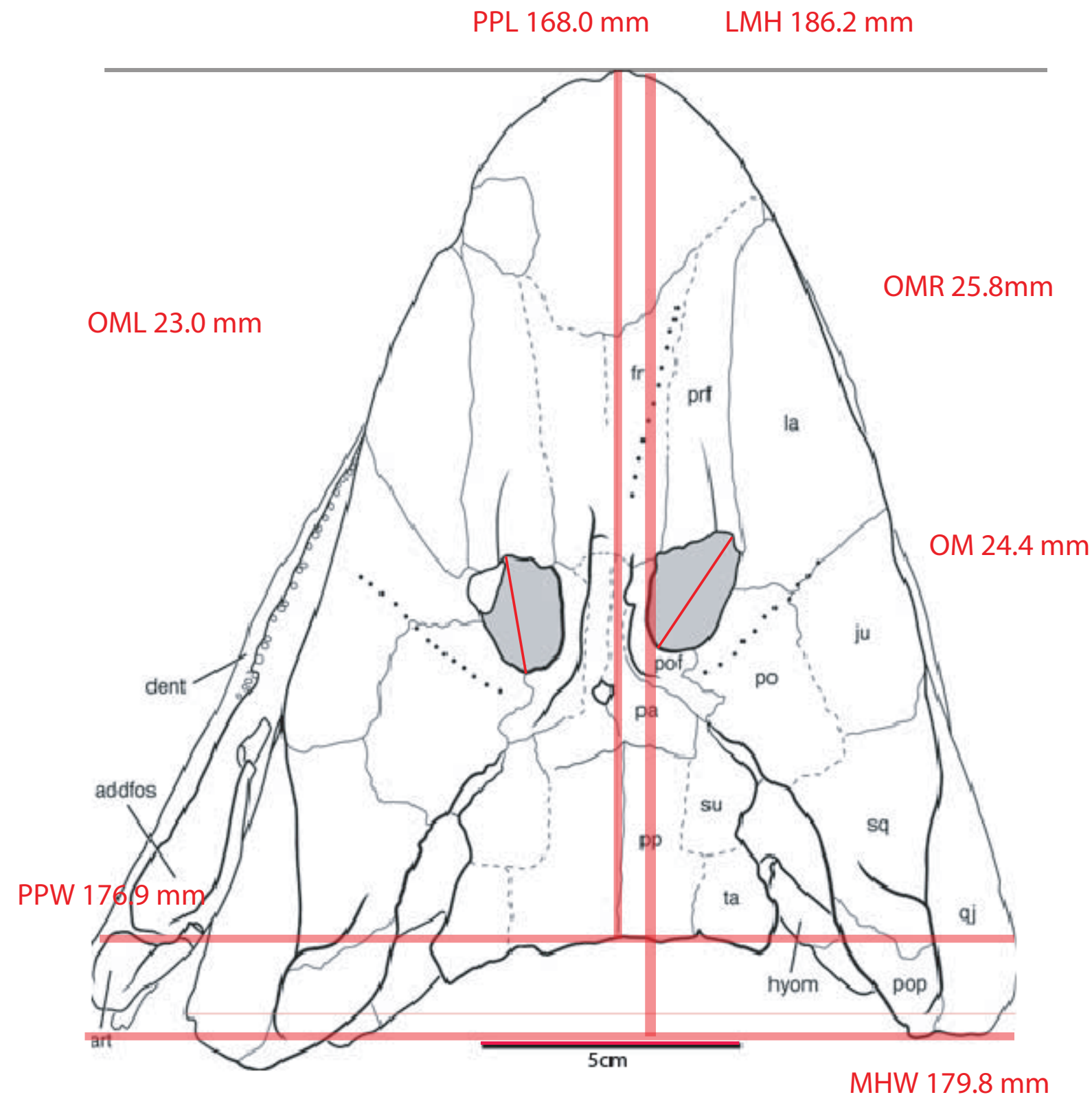

Tiktaalik roseae
382.7-379.2 Ma
Finned tetrapod (actual size)
Daeschler et al. (2006)

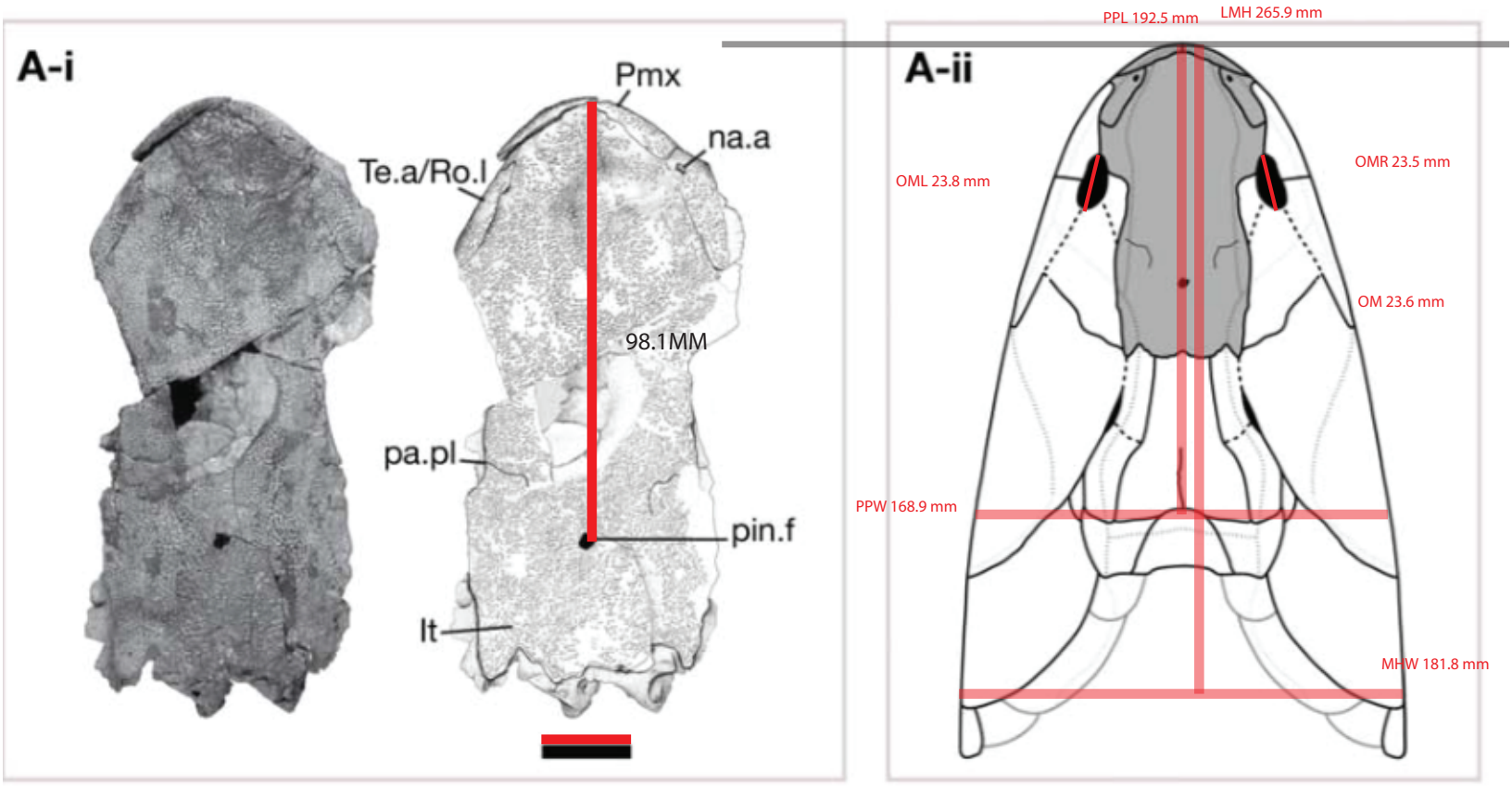

Tinirau clackae
385.2-382.7 Ma
Finned tetrapod (scaled 35%)
Swartz (2012)

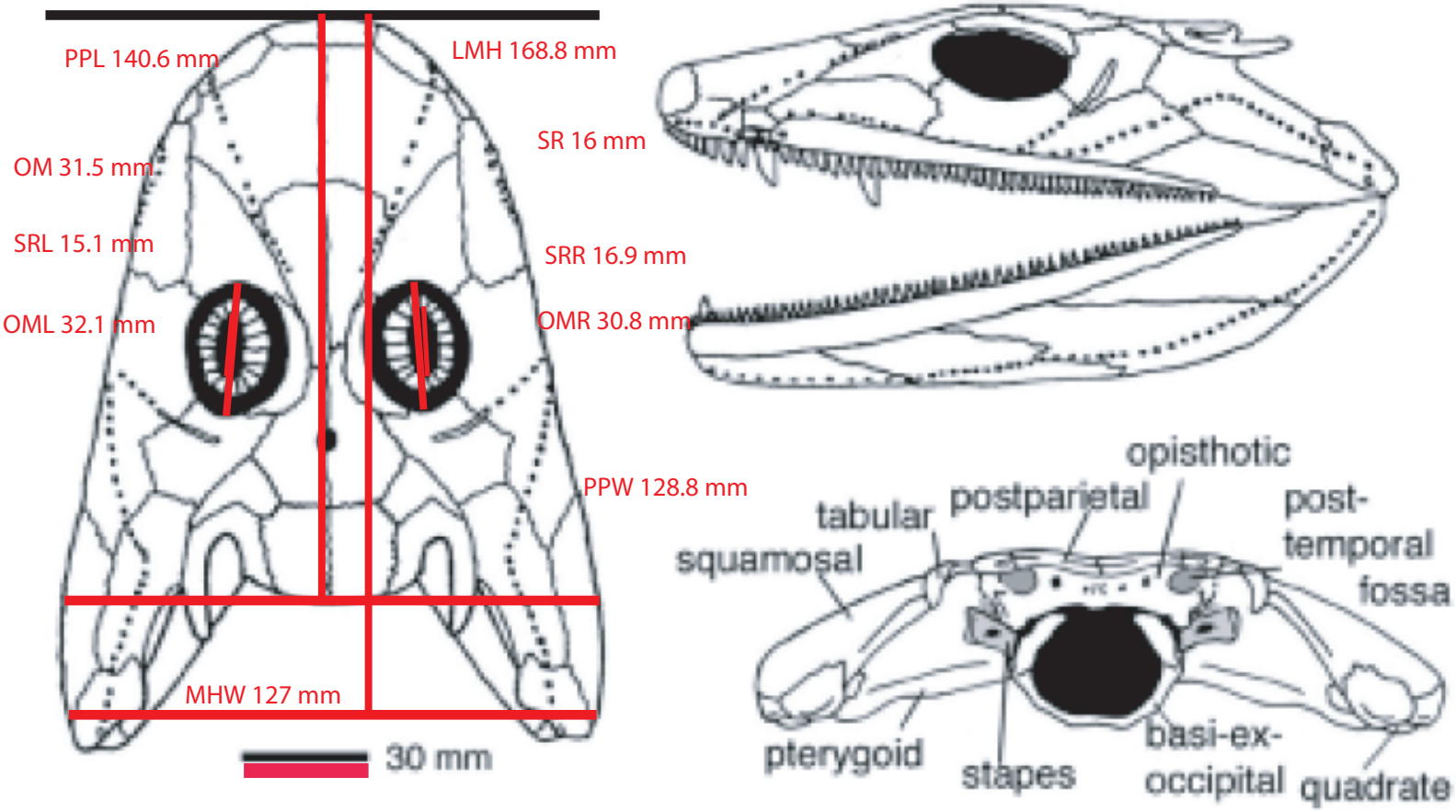

Acanthostega gunnari
367.8-363.3 Ma
Digited tetrapod (scaled 60%)
Clack (2002b); Porro et al. (2015)

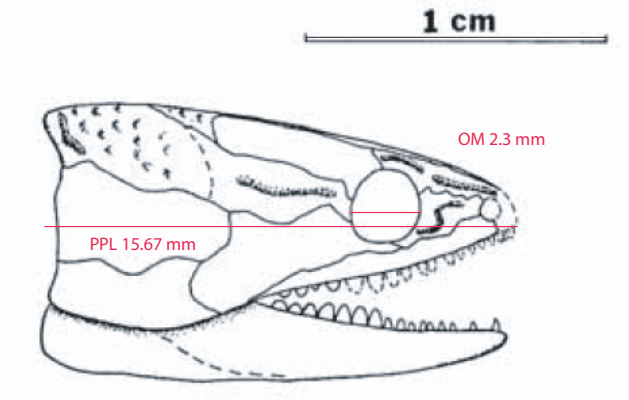

Acherontiscus caledoniae
330.9-315.2 Ma
Digited tetrapod (scaled 400%)
Carroll (1969)

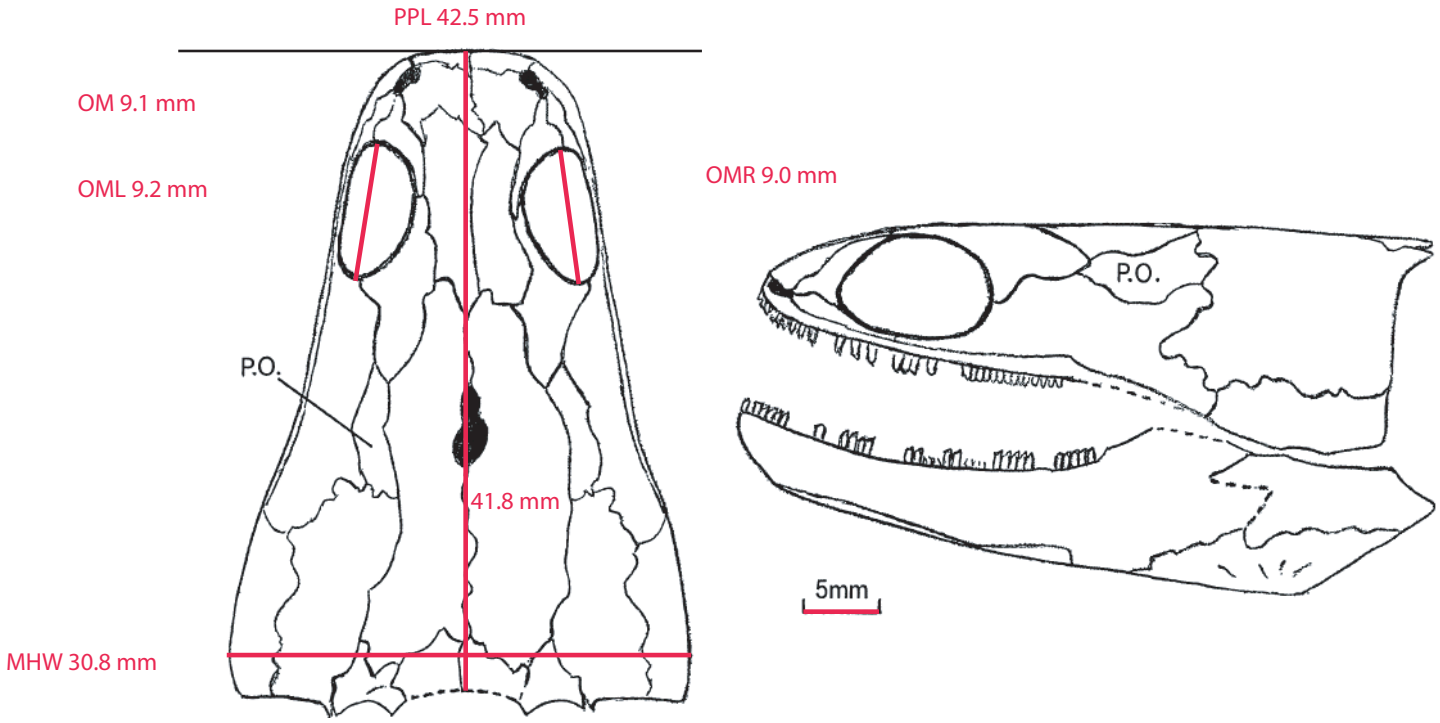

Adelogyrinus simnorhynchus
336.17-330.9 Ma
Digited tetrapod (scaled 200%)
Brough and Brough (1967)

123.0 mm

VOLUME 45 JANUARY 1967 NUMBER 1

PPL 67.4 mm

LMH 57.2 mm

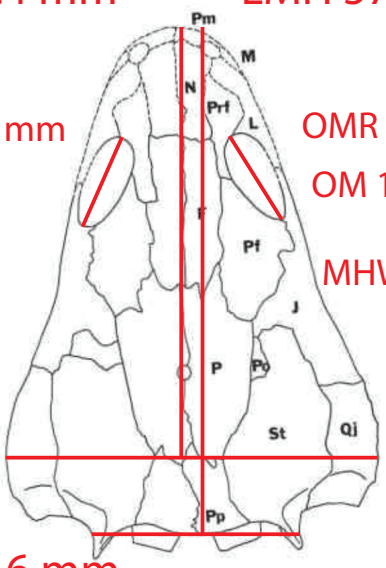

OML 13.0 mm

OMR 13.0 mm

OM 13.0 mm

MHW 49.4 mm

PPW 27.6 mm

Adelospondylus watsoni
319.2-315.2 Ma
Digited tetrapod (actual size)
Carroll (1967)

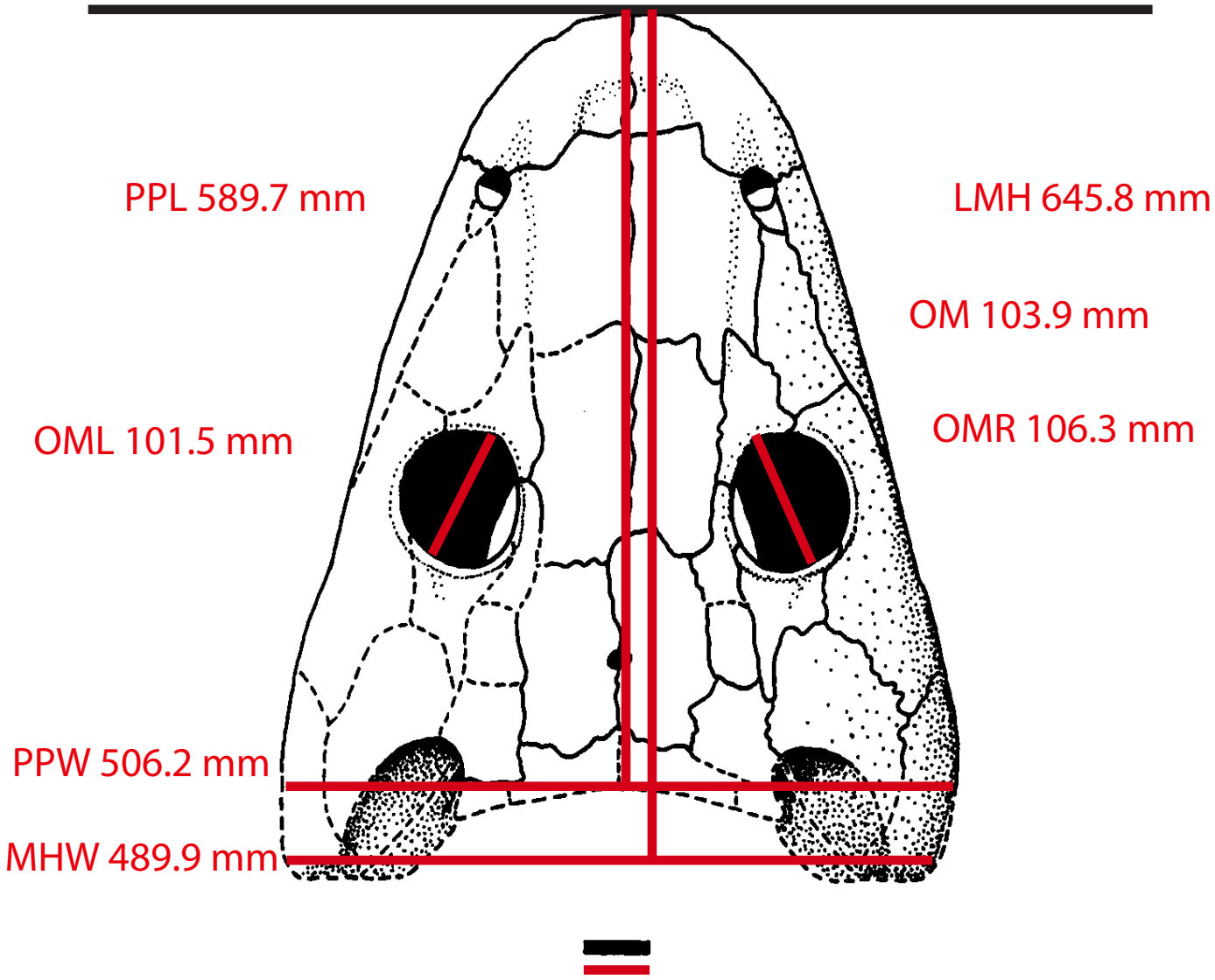

Adamanterpeton ohioensis
311.1-307 Ma
Digited tetrapod (scaled 20%)
Milner and Sequeira (1998)

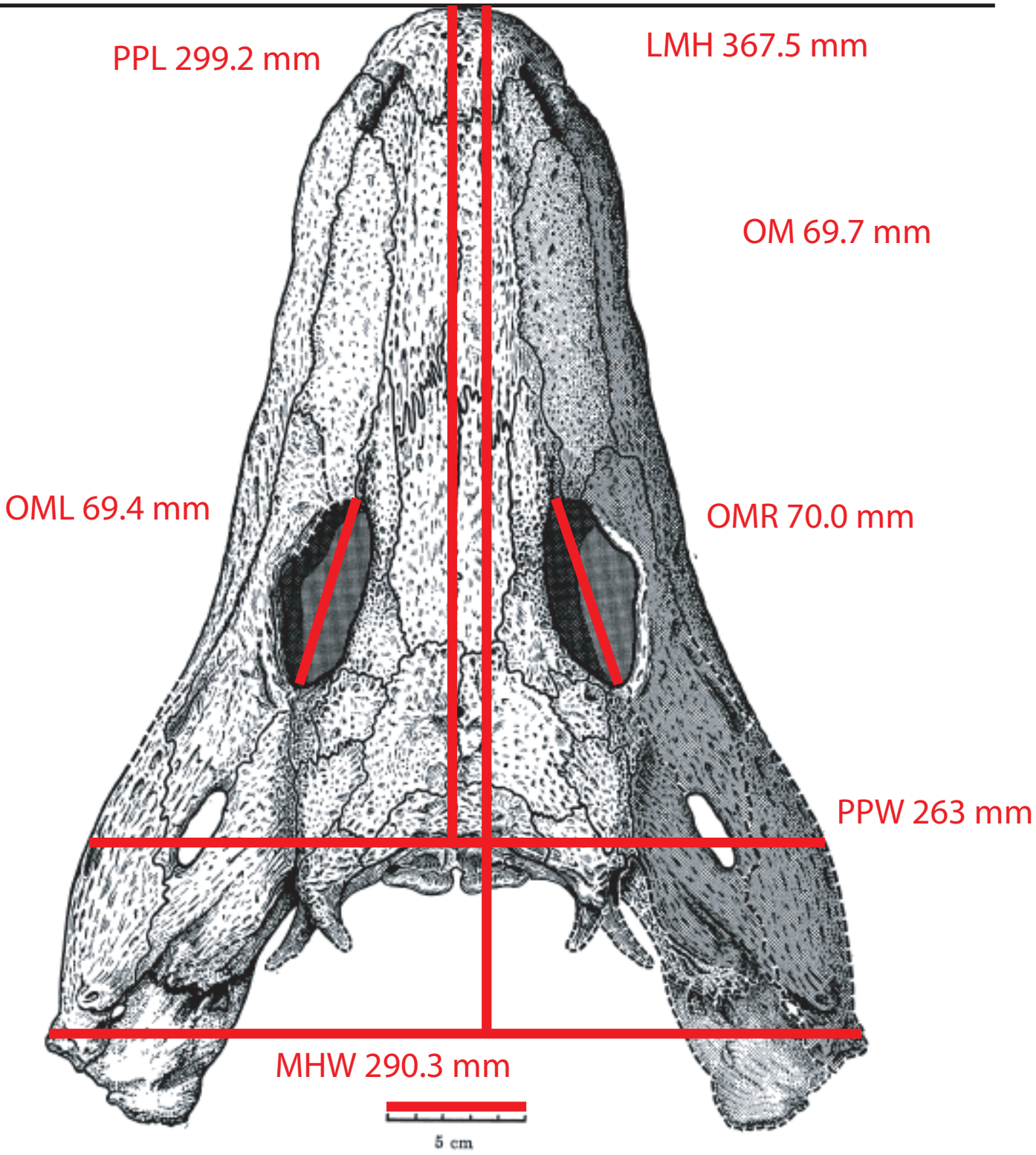

Anthracosaurus russelli
319.2-307 Ma
Digited tetrapod (scaled 50%)
Panchen (1977)

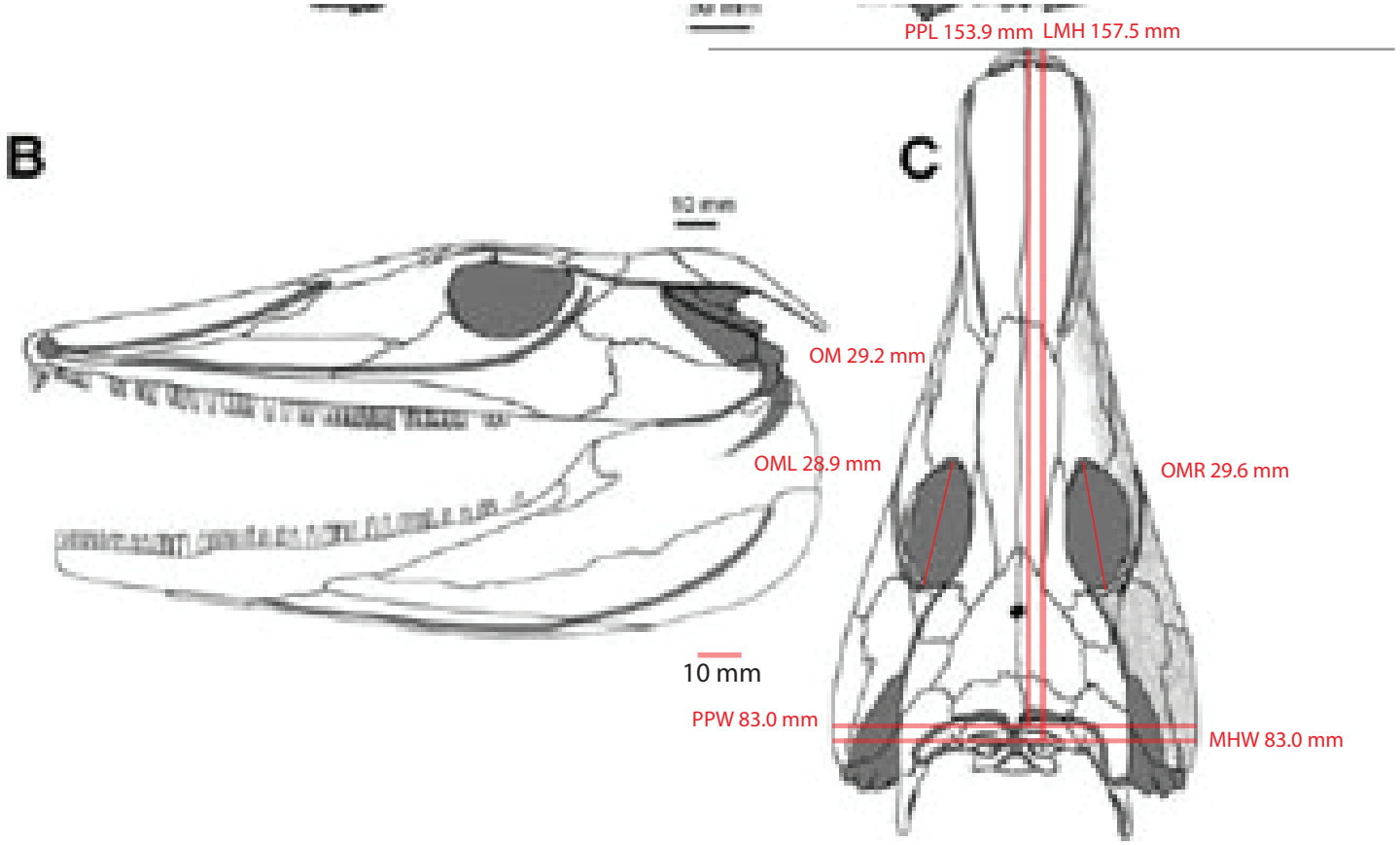

Archeria crassidisca
295.0-277.9 Ma
Digited tetrapod (scaled 60%)
Clack (2012)

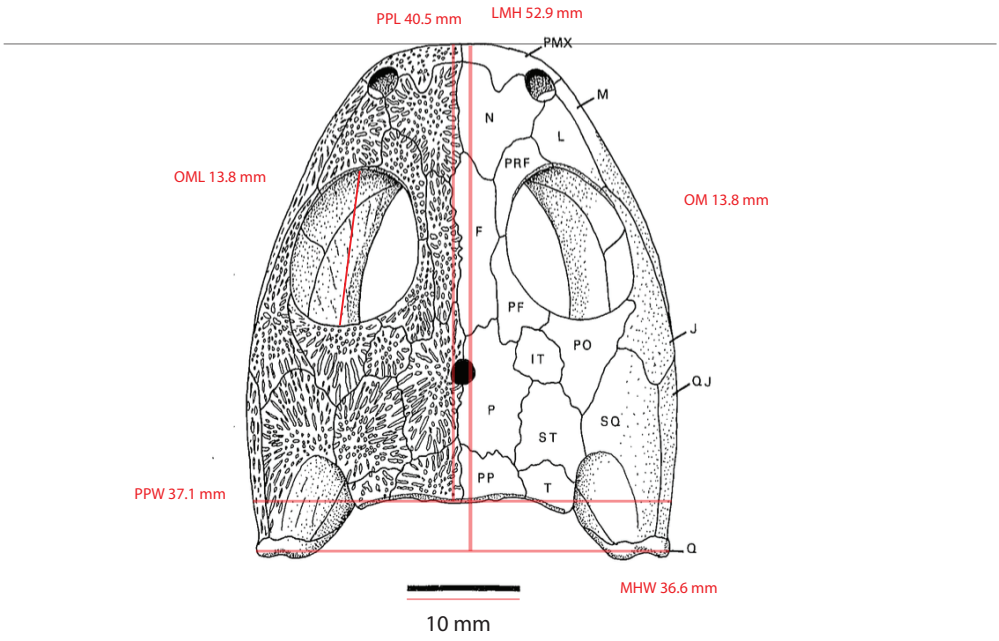

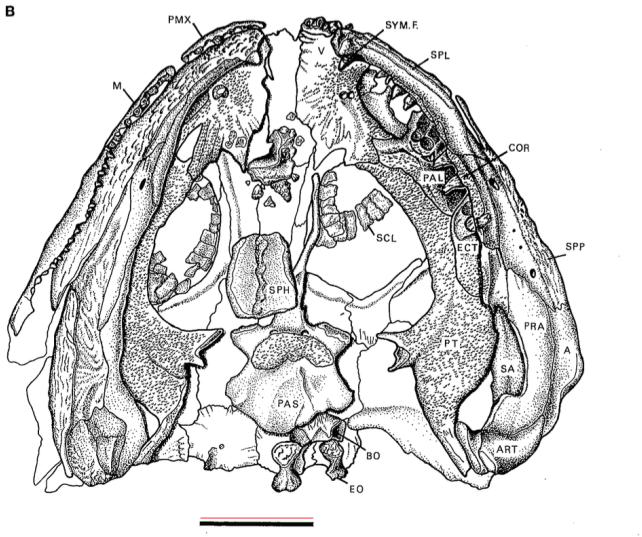

Balanerpeton woodi
336.2-330.9 Ma
Digited tetrapod (scaled 150%)
Milner and Sequeira (1994)

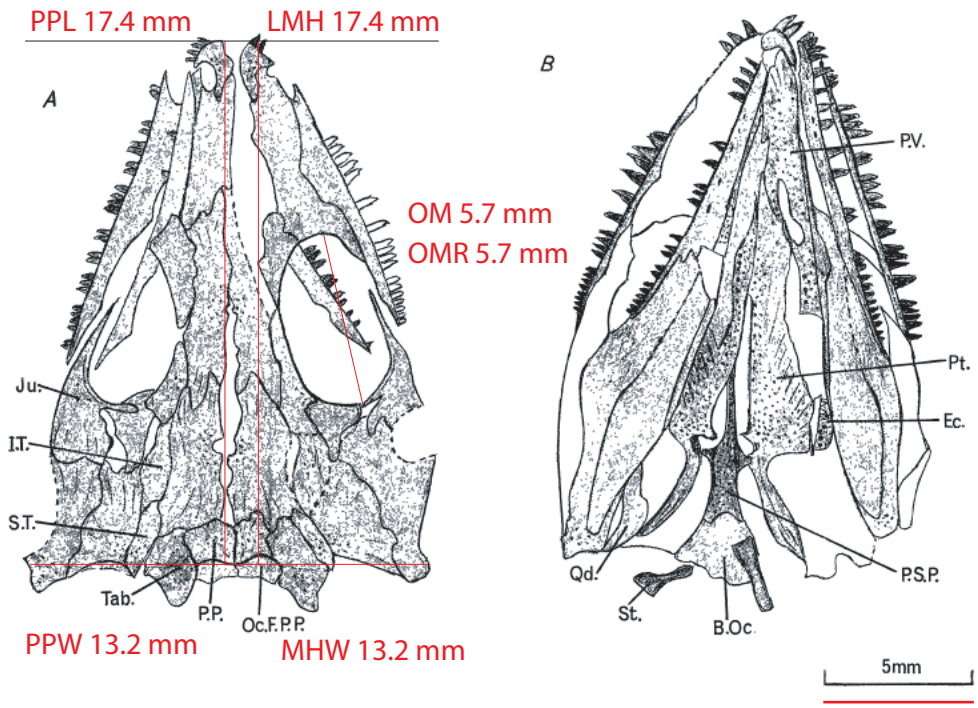

Gephyrostegus bohemicus
311.1-307 Ma
Digited tetrapod (scaled 400%)
Brough and Brough (1967)

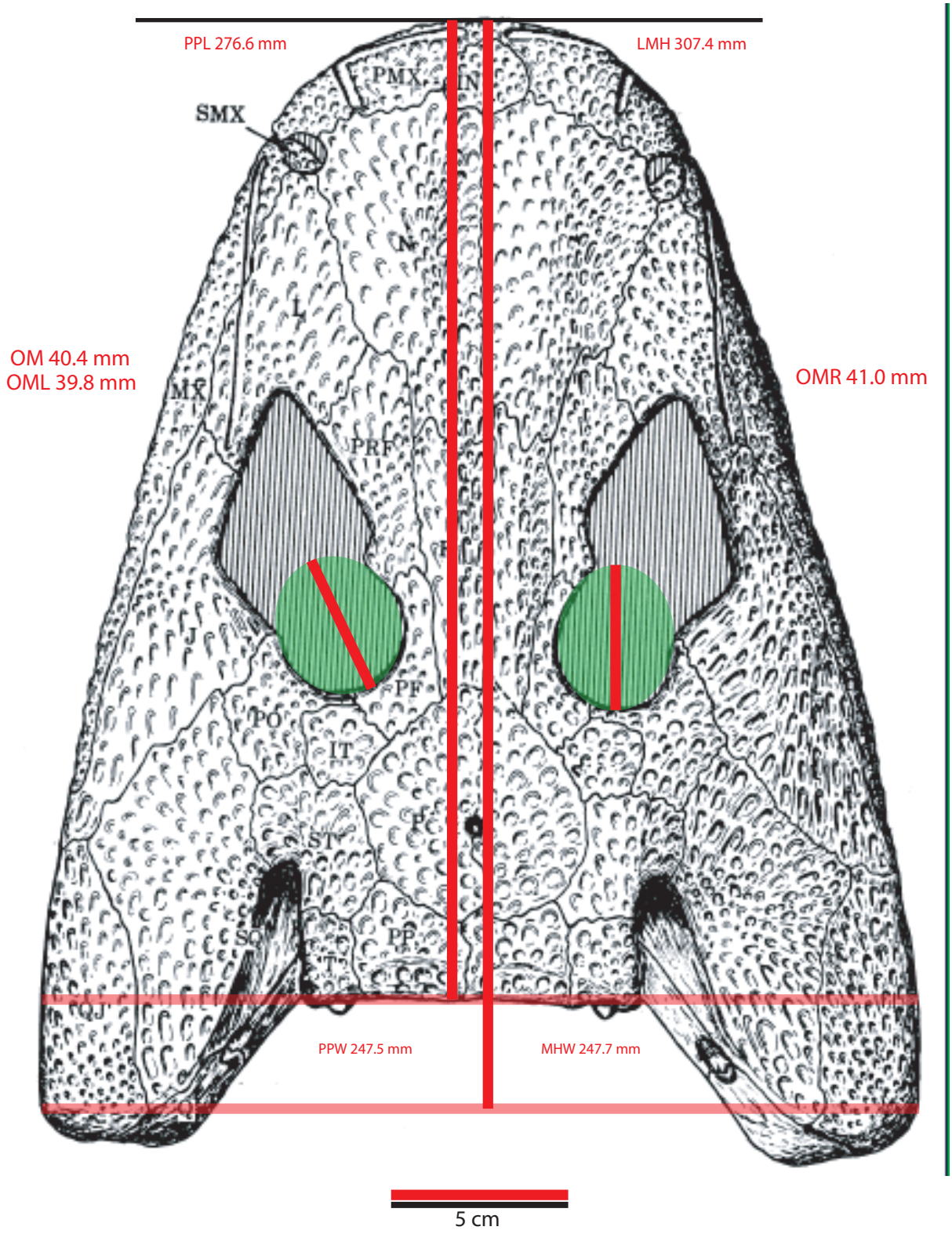

Baphetes kirkbyi
319.2-307 Ma
Digited tetrapod (scaled 60%)
Beaumont (1977)

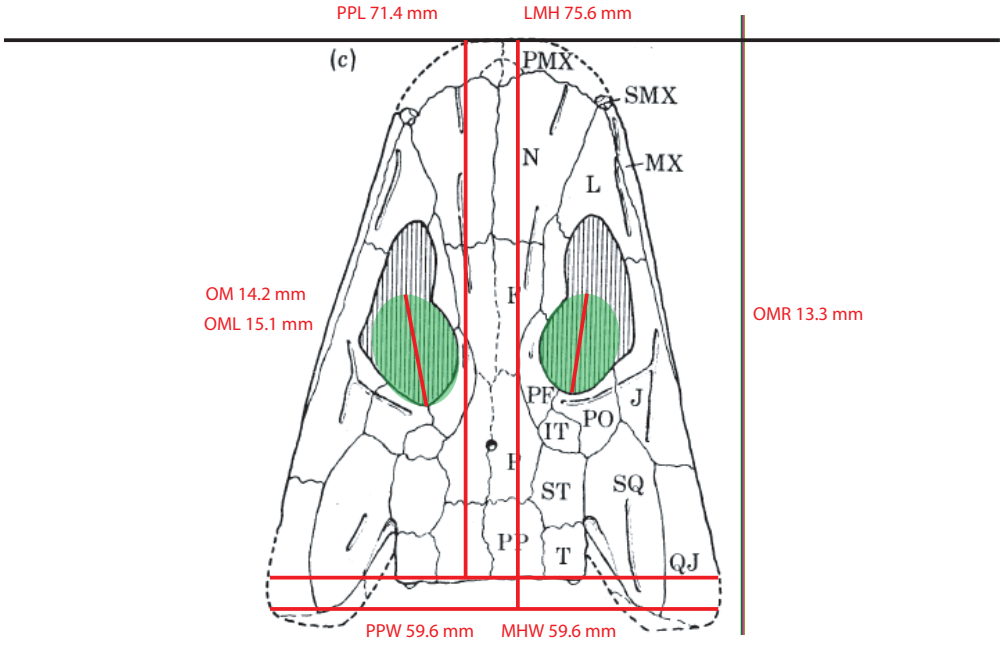

10 mm

Baphetes lintonensis
319.2-307 Ma
Digited tetrapod (actual size)
Beaumont (1977)

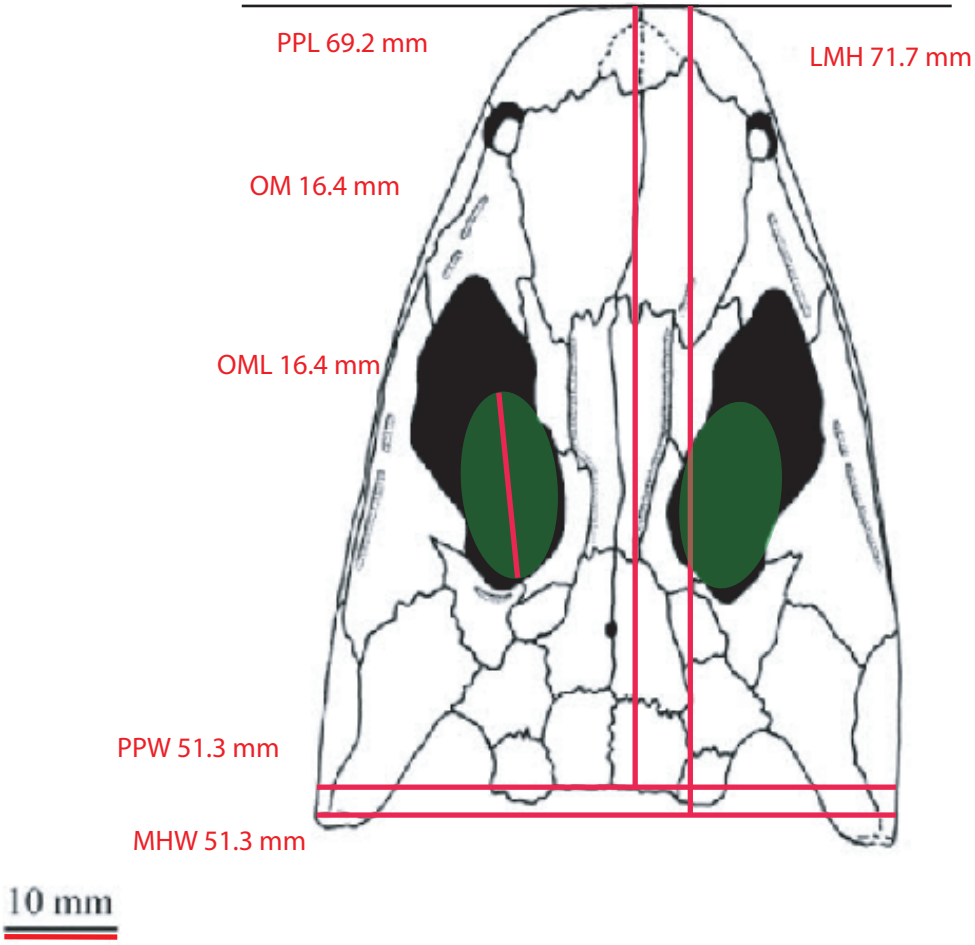

Baphetes orientalis
319.2-307 Ma
Digited tetrapod (scaled 150%)
Milner et al. (2009)

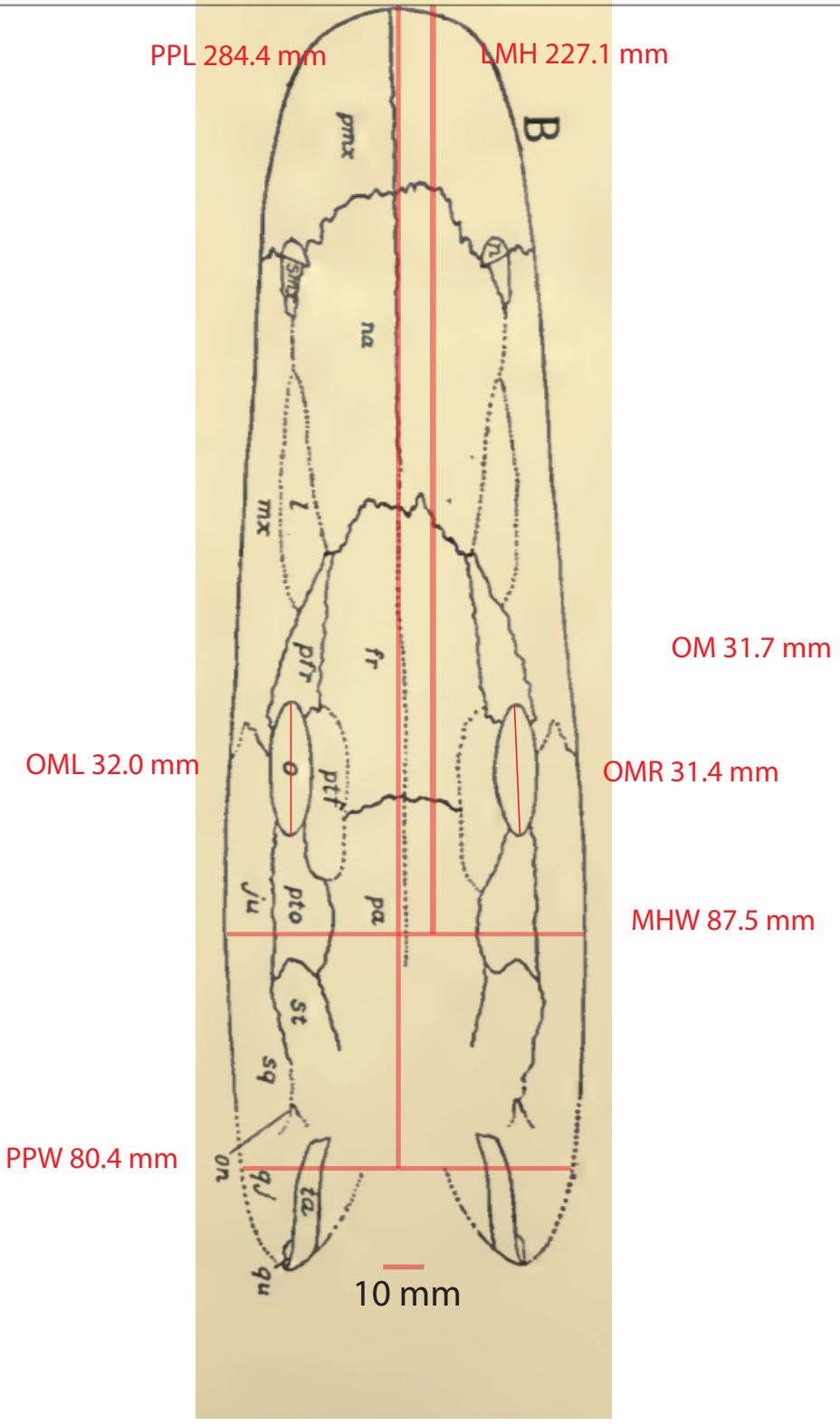

Chenoprosopus milleri
303.7-295.0 Ma
Digited tetrapod (scaled 60%)
Case et al. (1913)

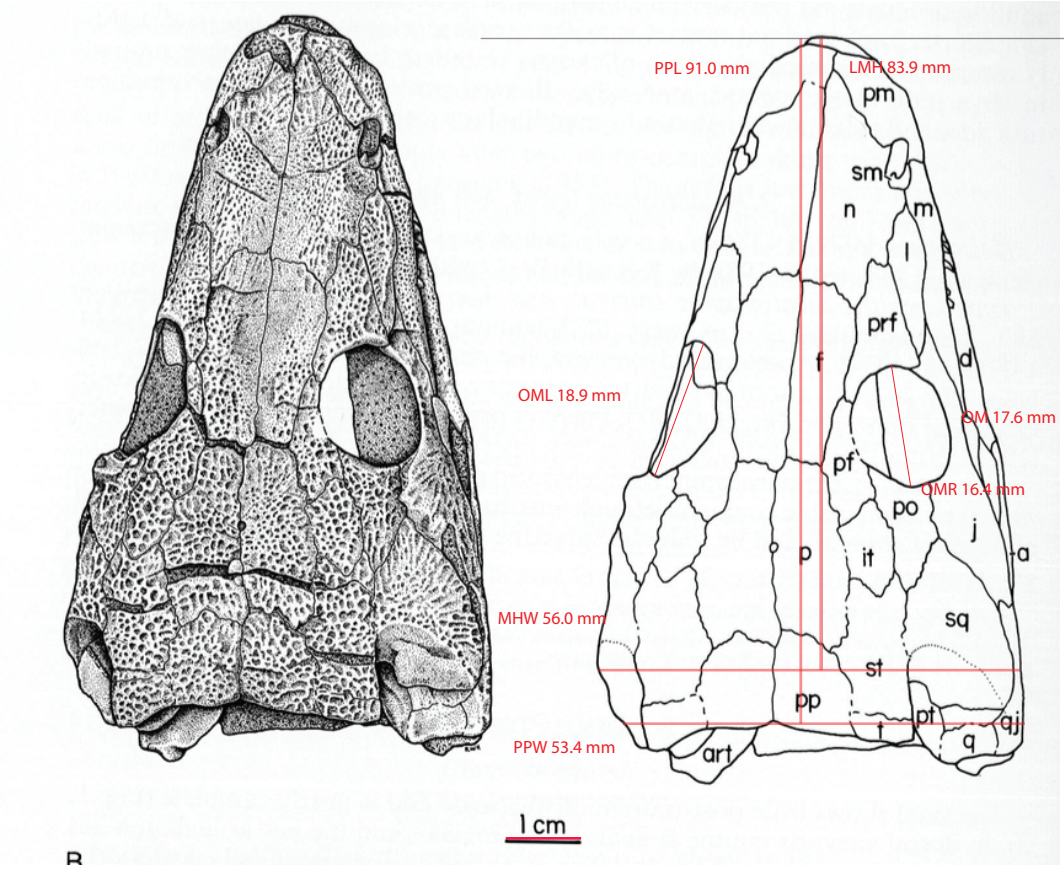

Chenoprosopus lewisi
303.7-295.0 Ma
Digited tetrapod (actual size)
Hook (1993)

PPL 204.1 mm LMH 176.6 mm

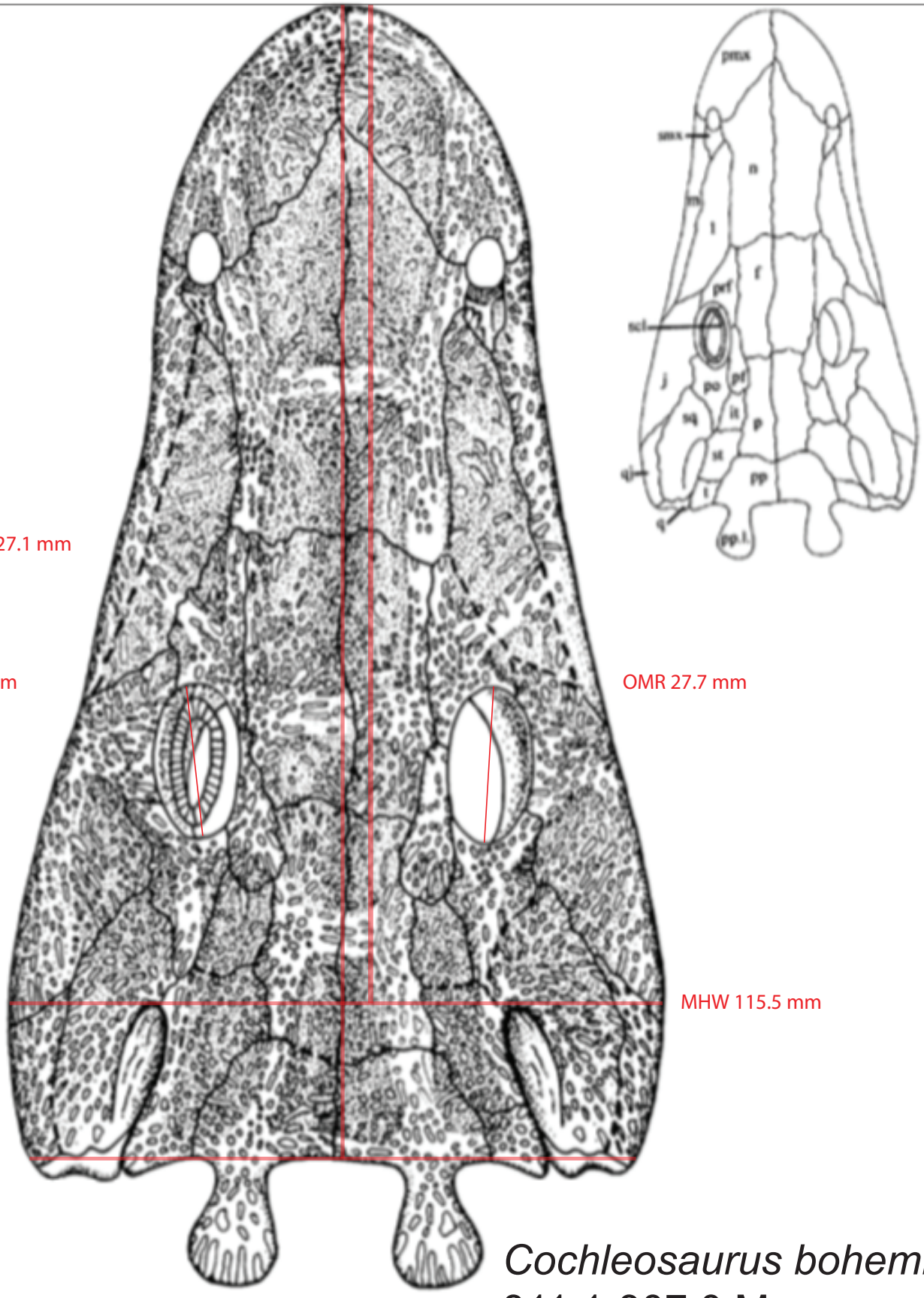

OM 27.1 mm

OML 26.6 mm

OMR 27.7 mm

MHW 115.5 mm

PPW 107.2 mm

10 mm

Cochleosaurus bohemicus
311.1-307.0 Ma
Digited tetrapod (actual size)
Sequeira (2003)

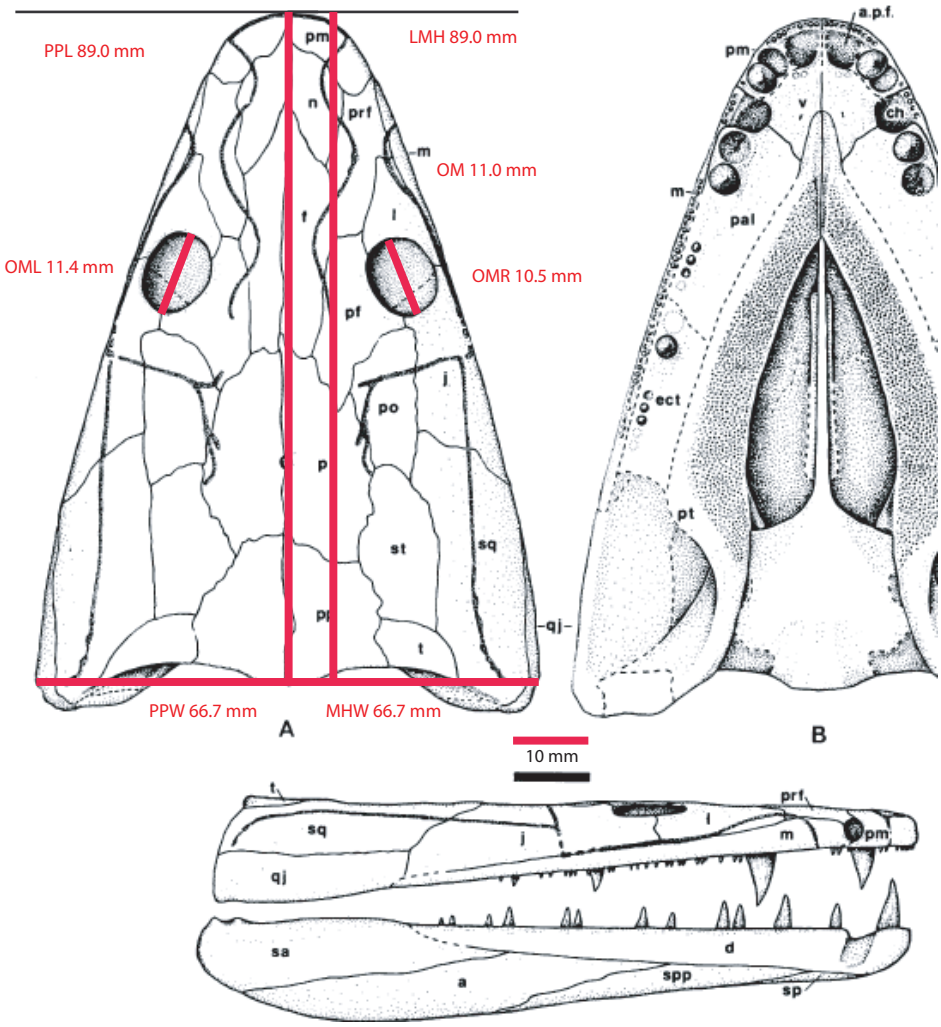

Colosteus scutellatus
311.1-307 Ma
Digited tetrapod (actual size)
Hook (1983)

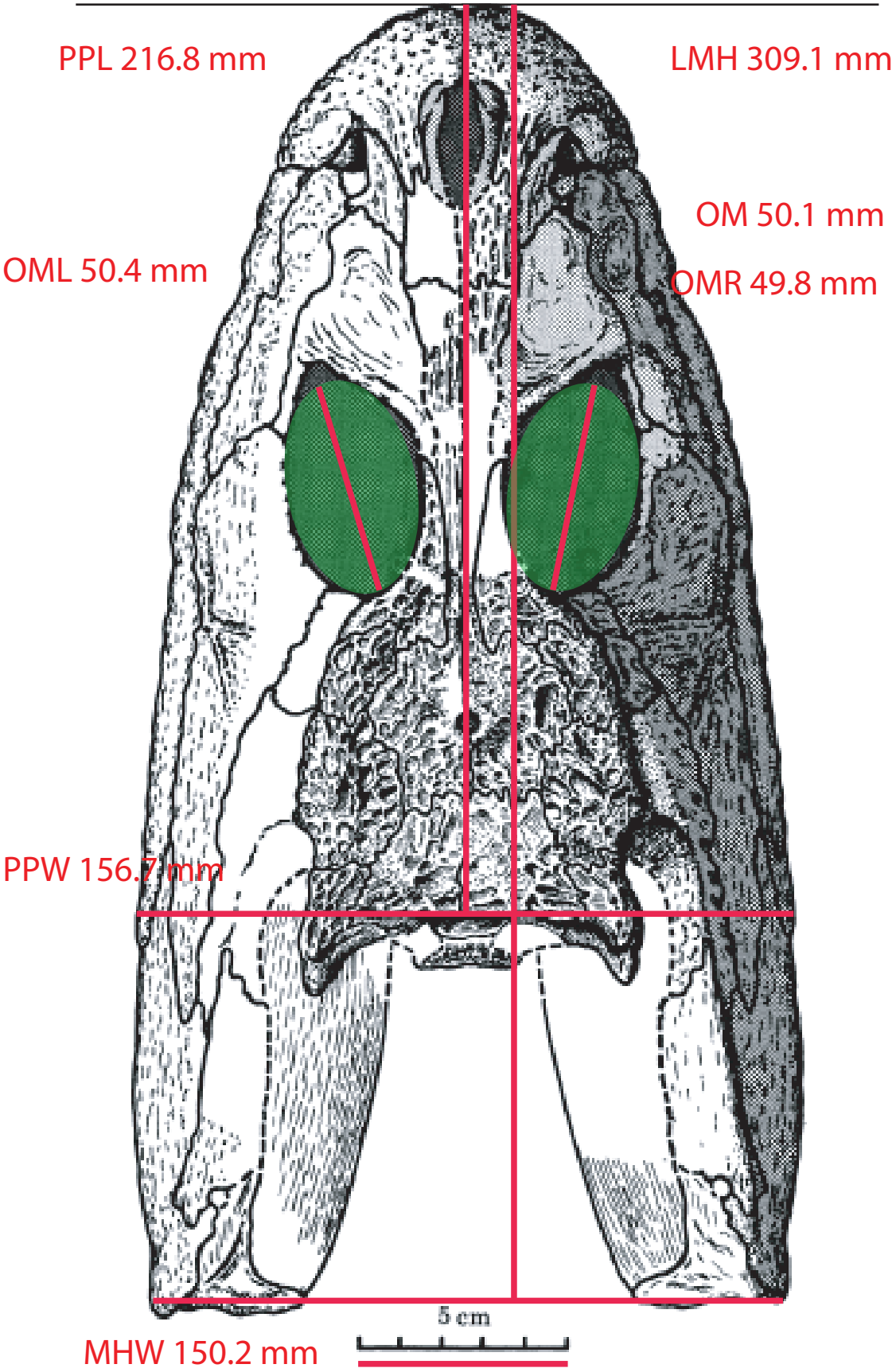

Crassigyrinus scoticus
336.2-327.1 Ma
Digited tetrapod (scaled 70%)
Panchen (1985)

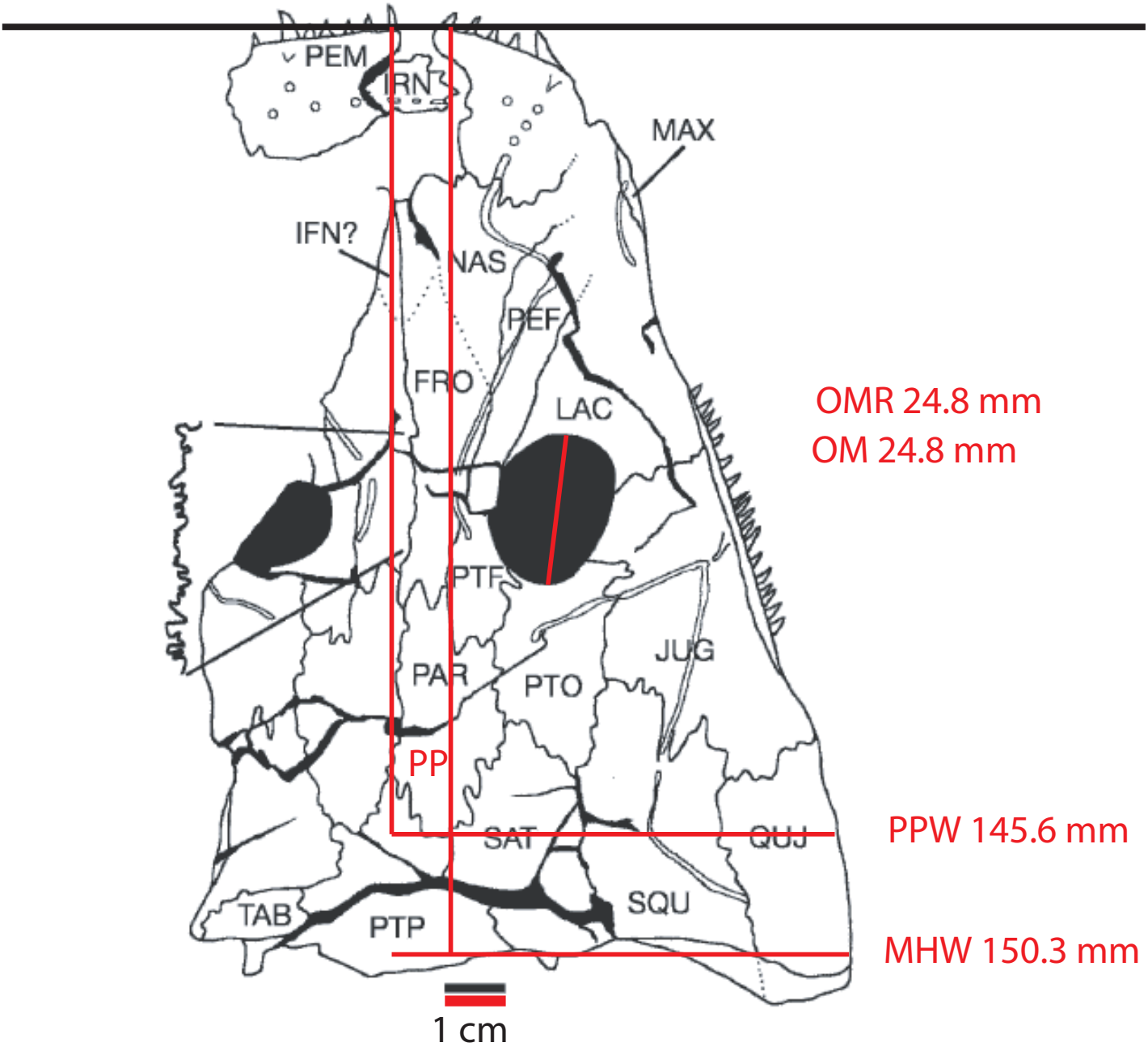

Deltaherpeton hiemstrae
341.4-336.2 Ma
Digited tetrapod (actual size)
Bolt and Lombard (2010)

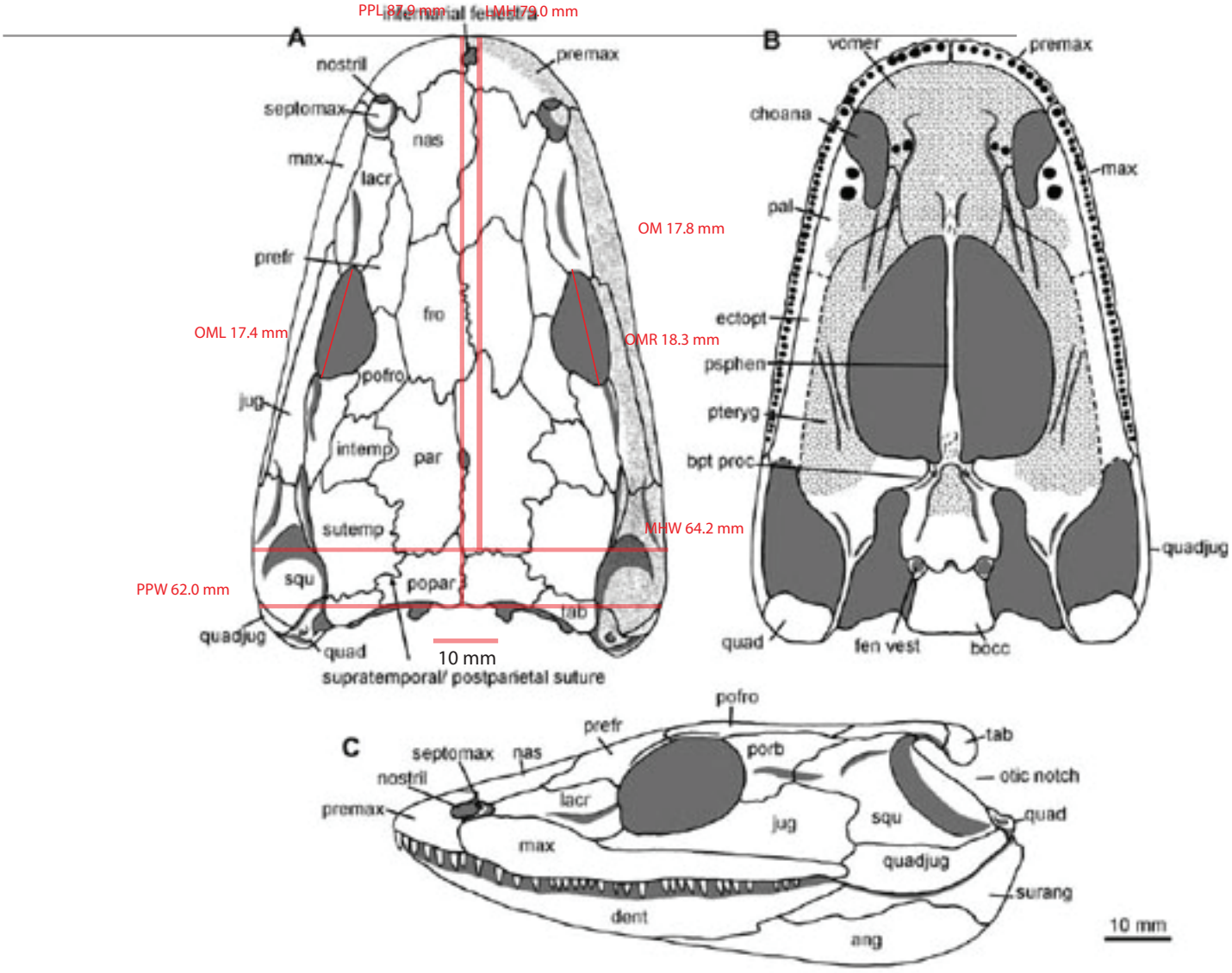

Dendrerpeton acadianum
323.2-315.2 Ma
Digited tetrapod (actual size)
Holmes et al. (1998)

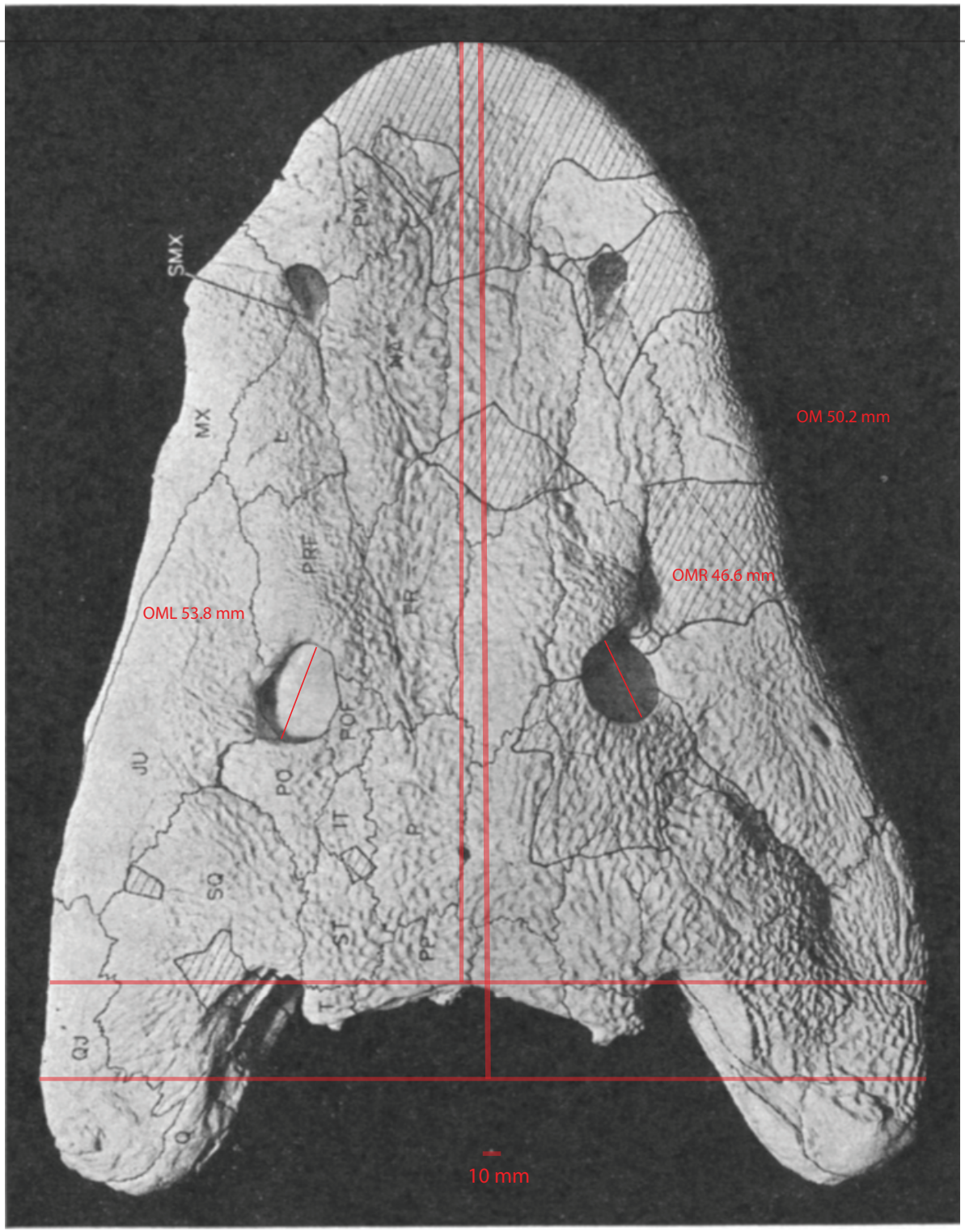

Edops craigi
295.0-292.6 Ma
Digited tetrapod (scaled 30%)
Romer and Witter (1942)

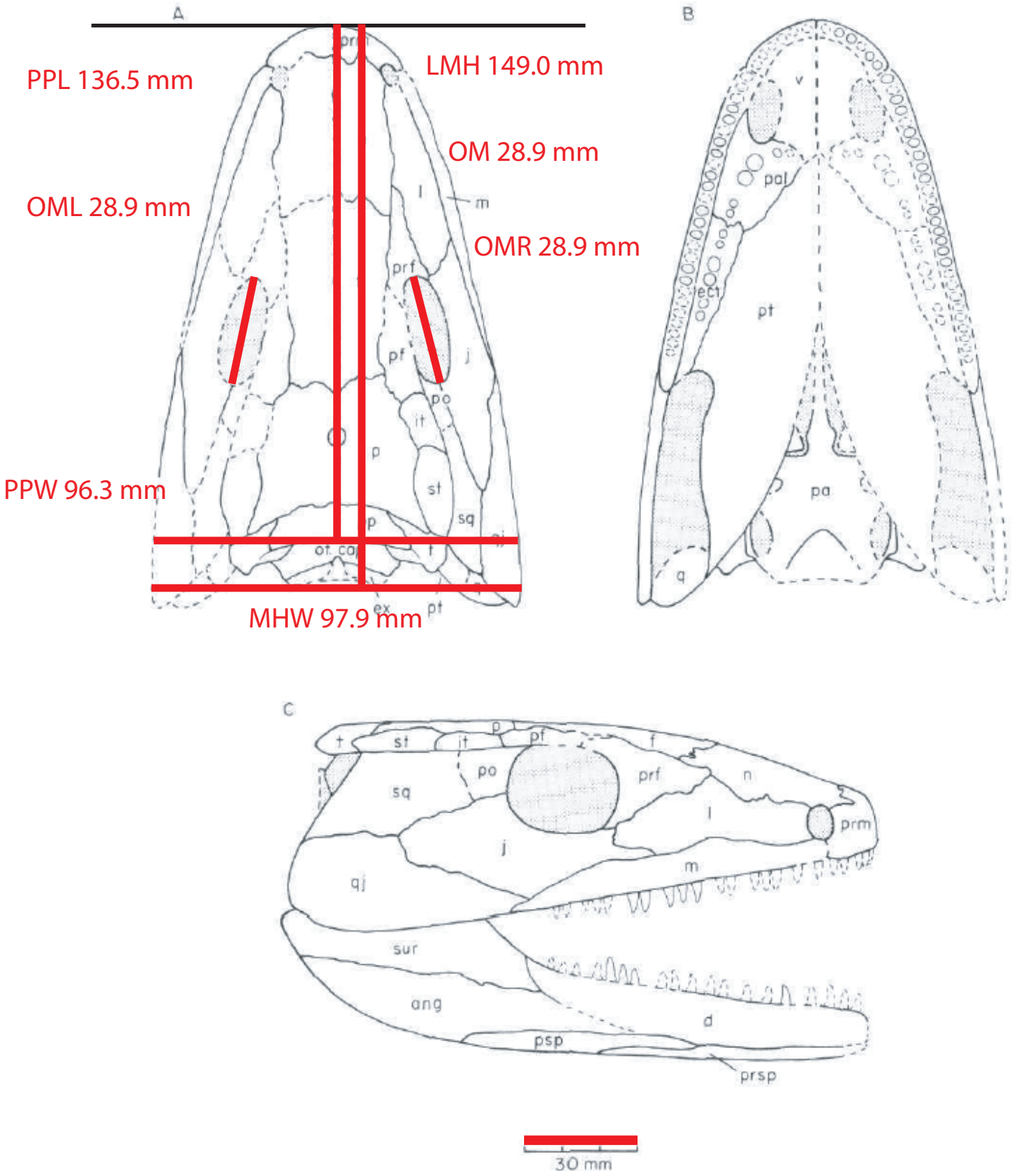

Eoherpeton watsoni
336.2-330.9 Ma
Digited tetrapod (scaled 70%)
Smithson (1985)

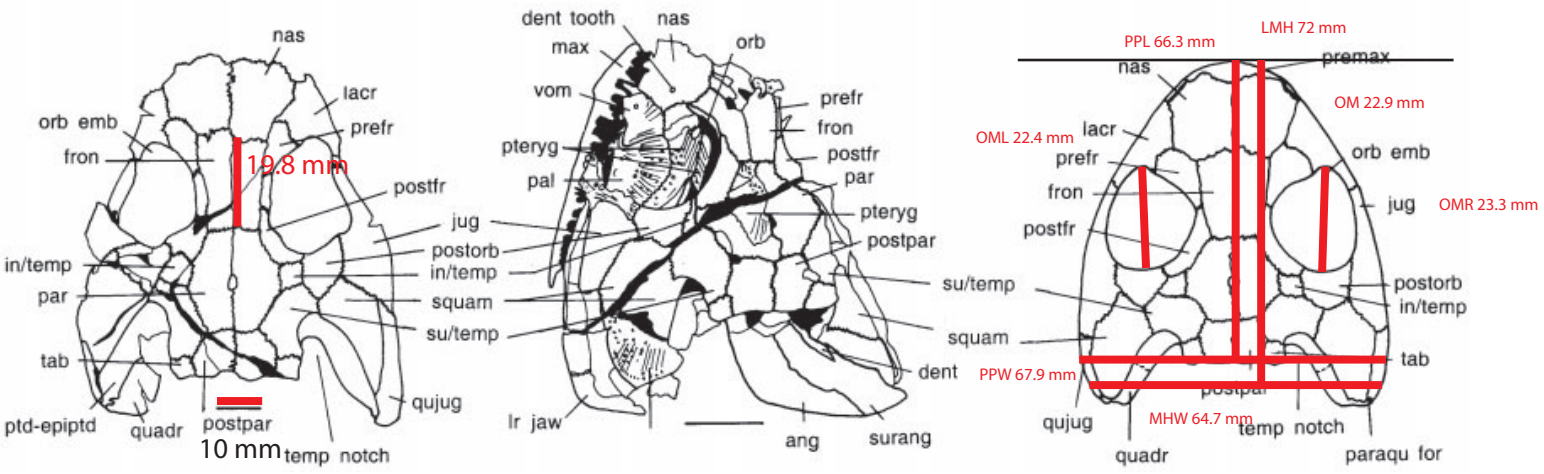

Eucritta melanolimnetes
336.2-330.9 Ma
Digited tetrapod (scaled 60%)
Clack (1998)

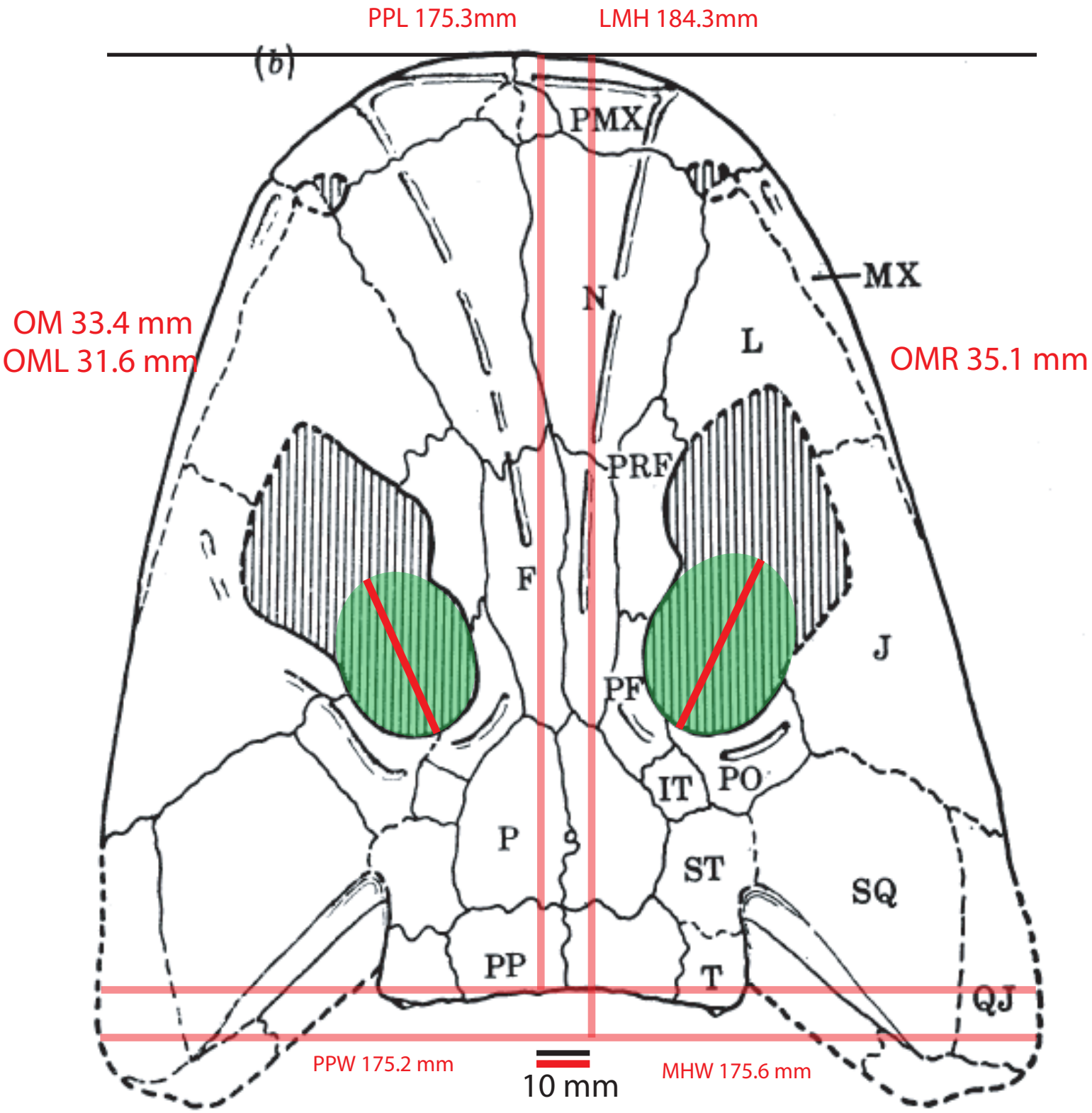

Baphetes bohemicus
311.1-307 Ma
Digited tetrapod (actual size)
Beaumont (1977)

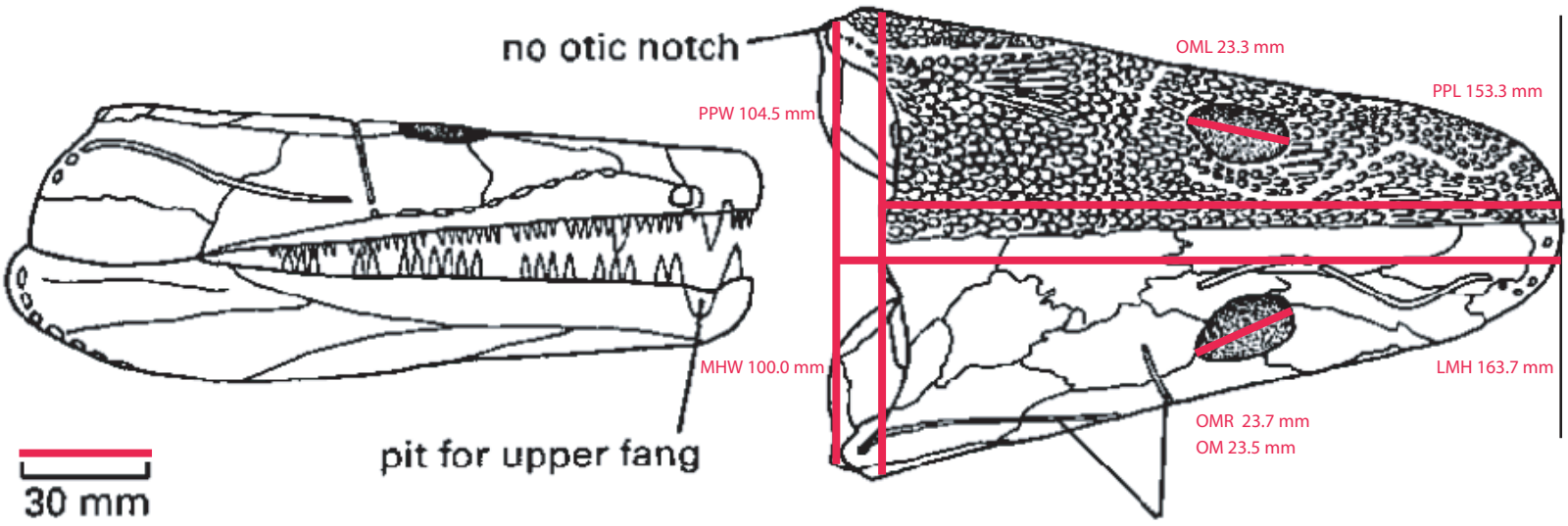

Greererpeton burkemorani
327.1-319.2 Ma
Digited tetrapod (scaled 60%)
Benton (2000)

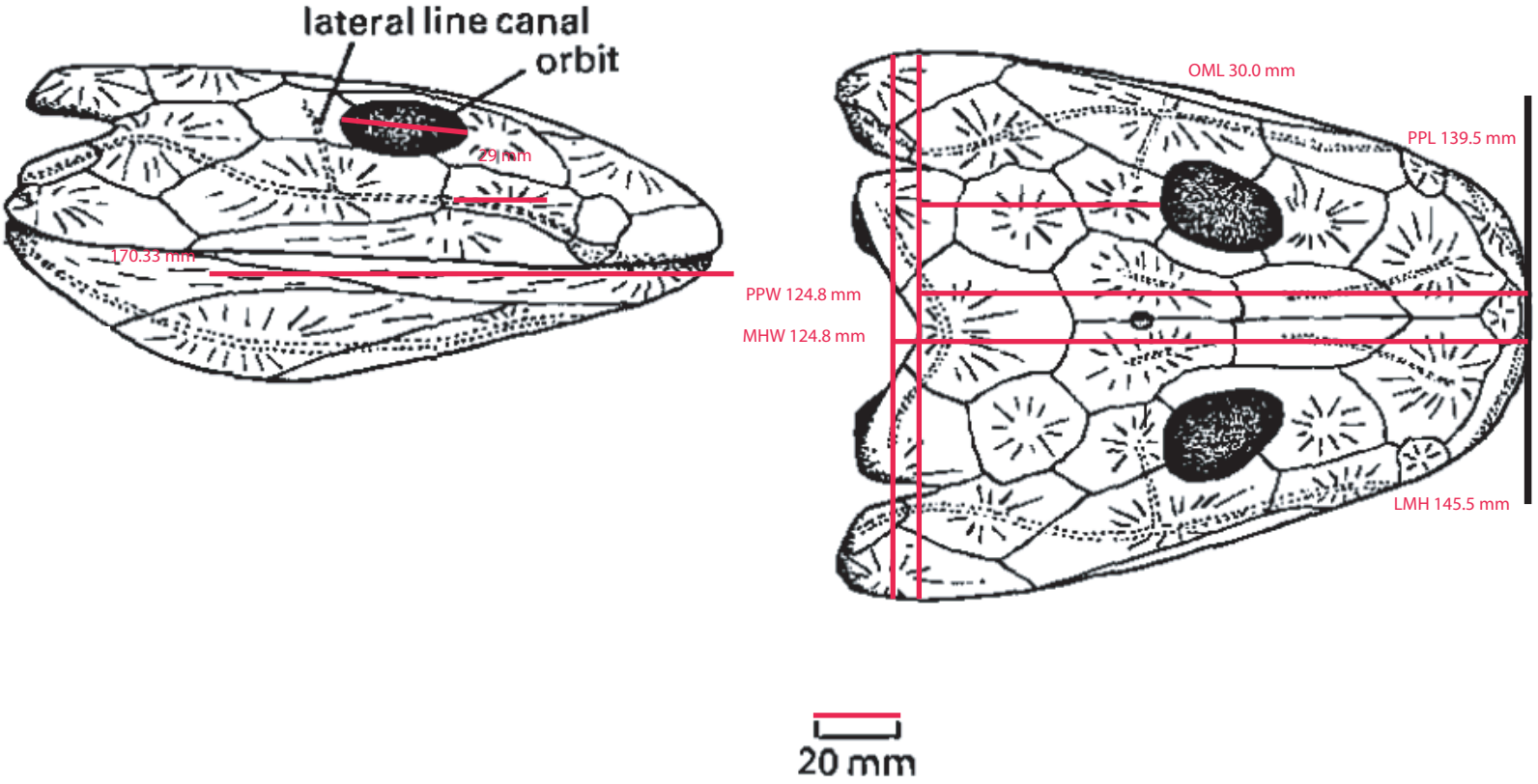

Ichthyostega
367.8-363.3 Ma
Digited tetrapod (scaled 60%)
Benton (2000)

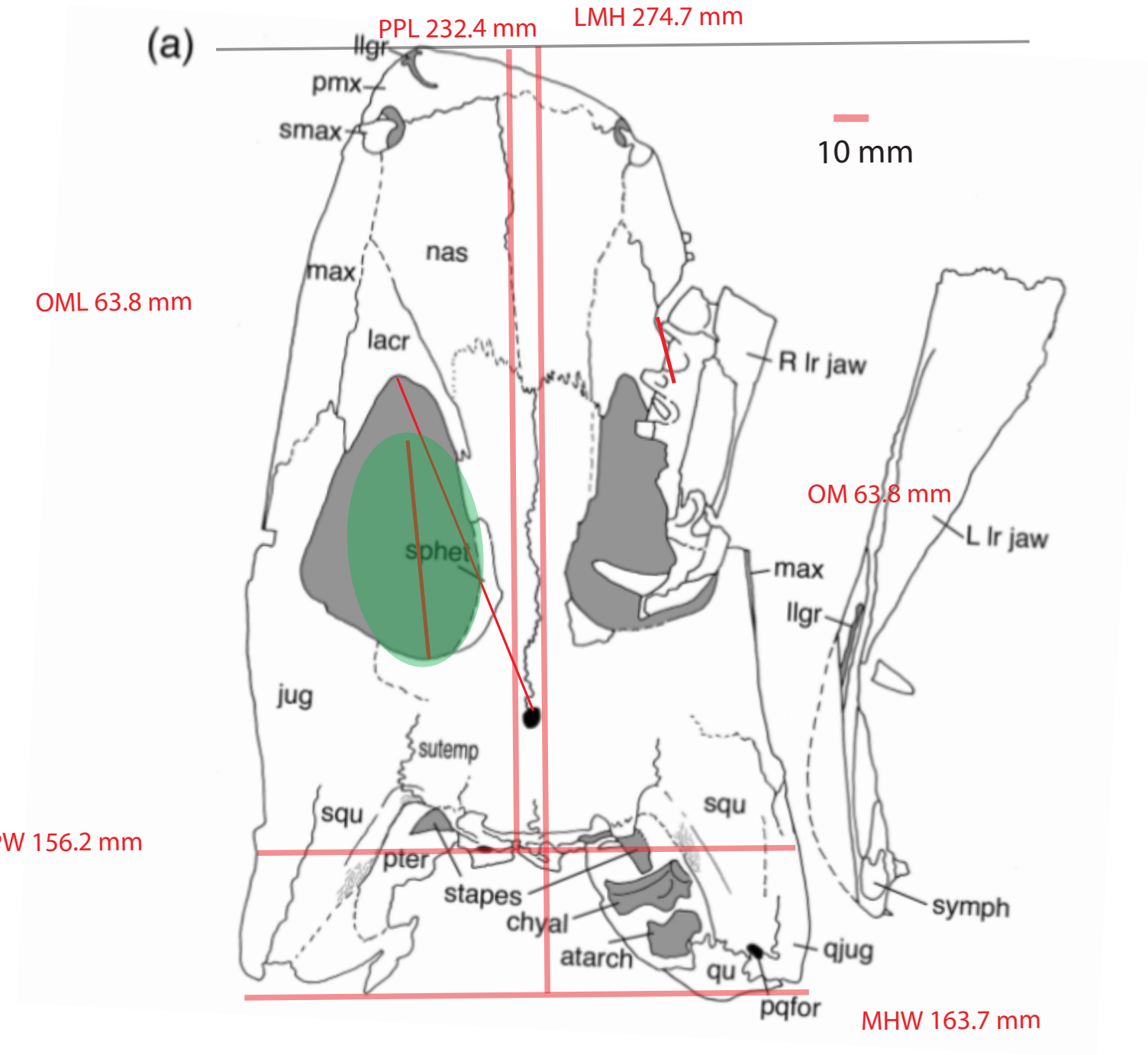

Kyrinion martilli
319.2-315.2 Ma
Digited tetrapod (scaled 60%)
Clack (2003)

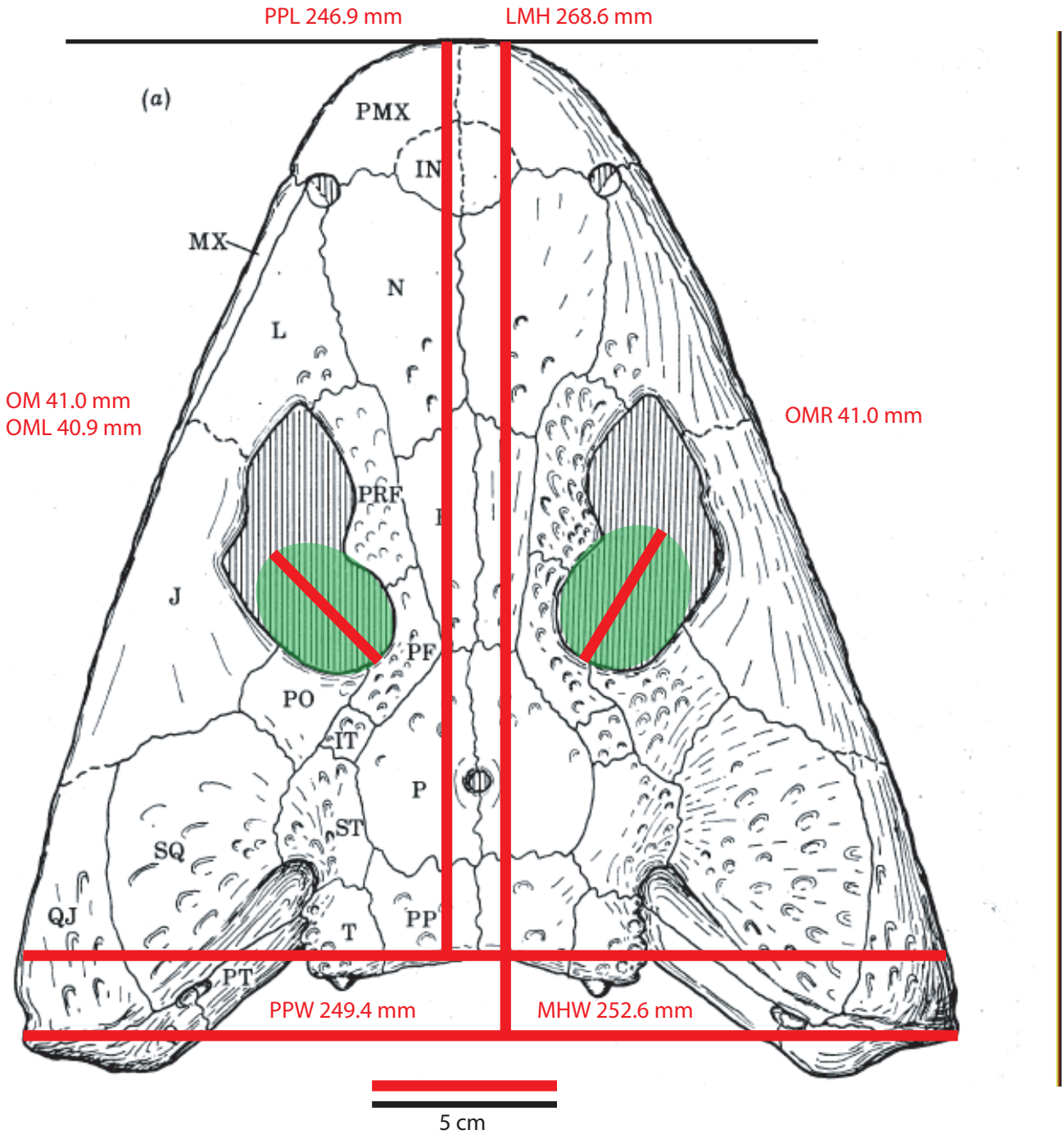

Loxomma acutirhinus
336.2-315.2 Ma
Digited tetrapod (scaled 60%)
Beaumont (1977)

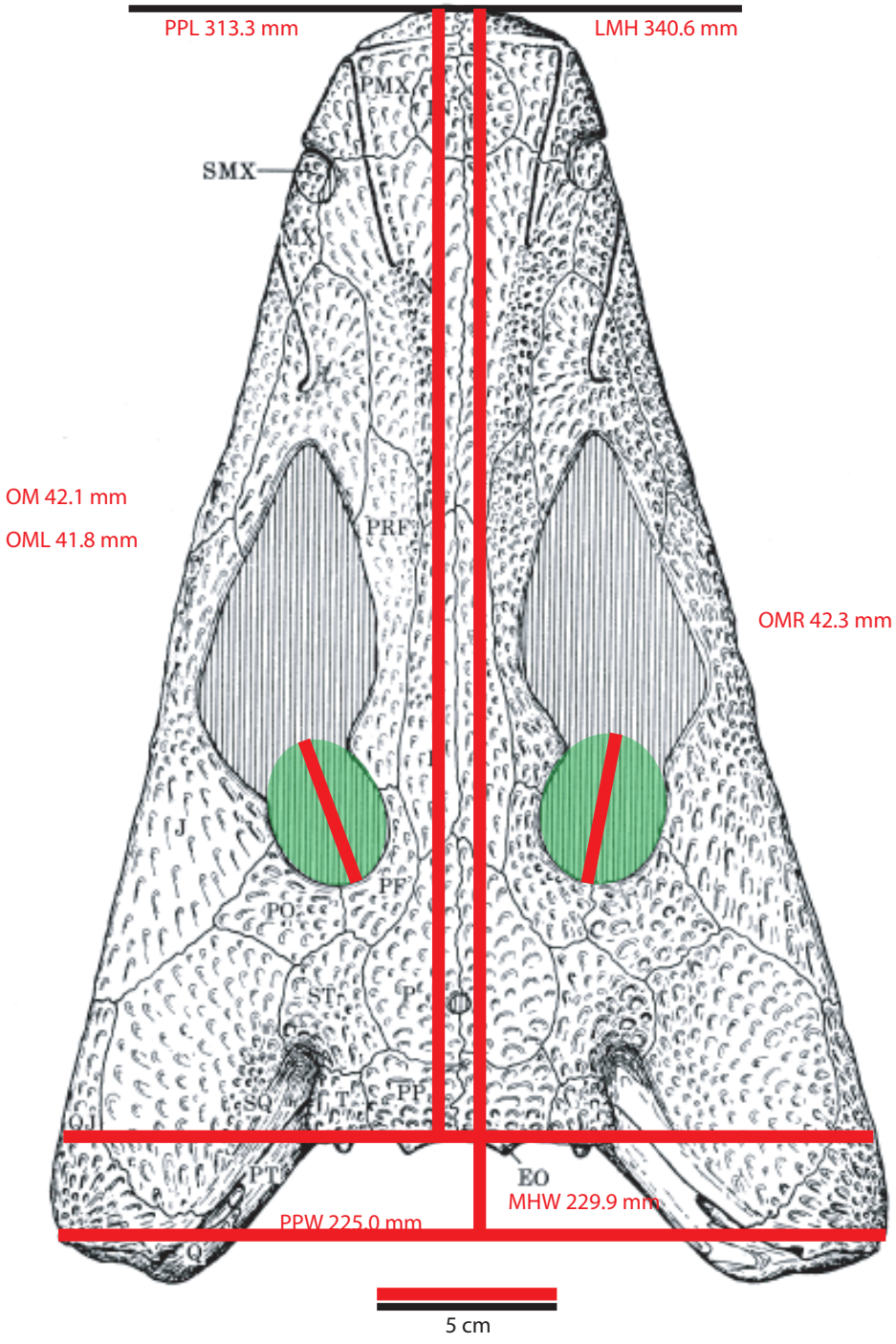

Megalocephalus pachycephalus
319.2-307 Ma
Digited tetrapod (scaled 50%)
Beaumont (1977)

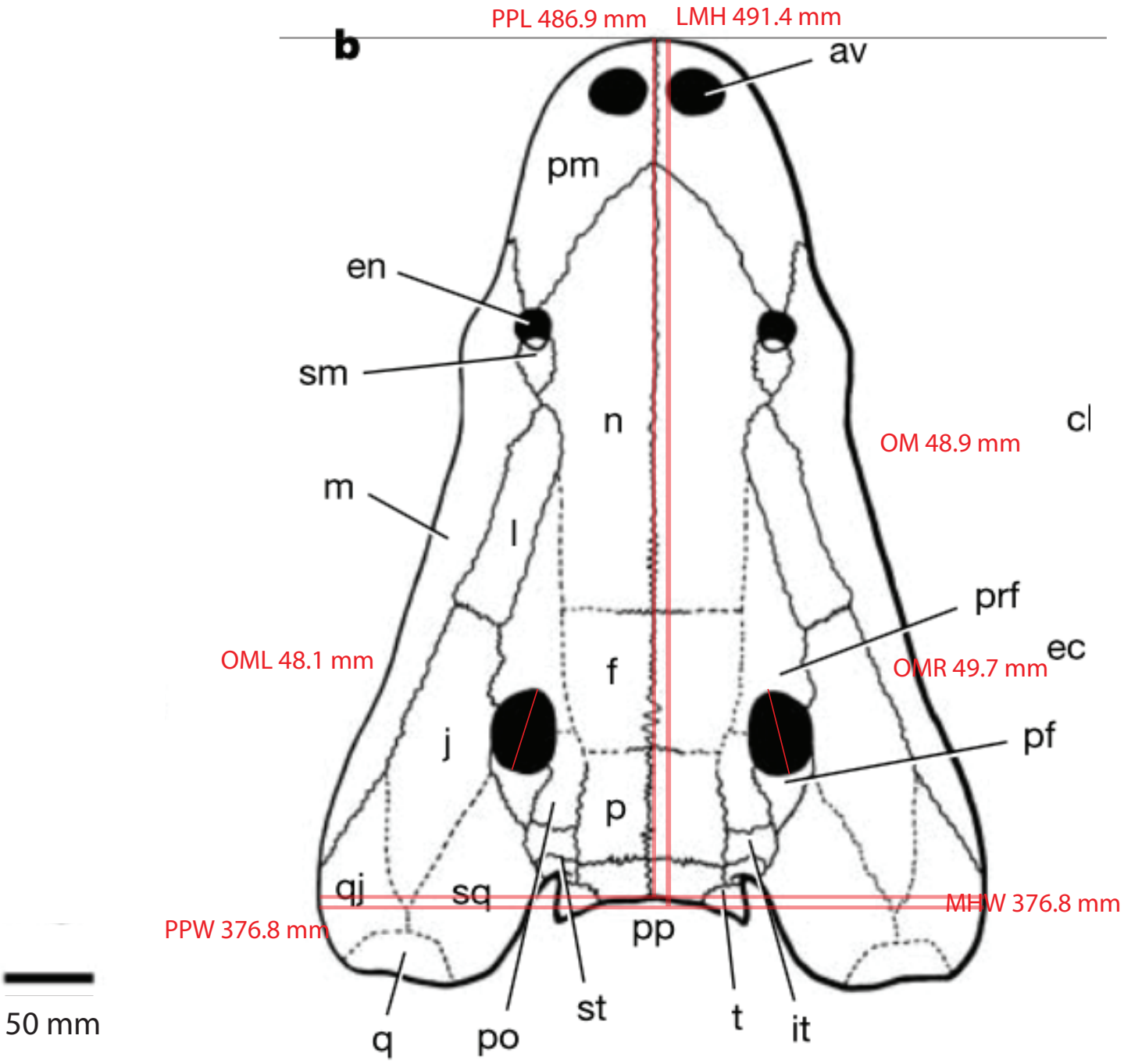

Nigerpeton ricqlesi
259.8-254.1 Ma
Digited tetrapod (scaled 30%)
Sidor et al. 2005

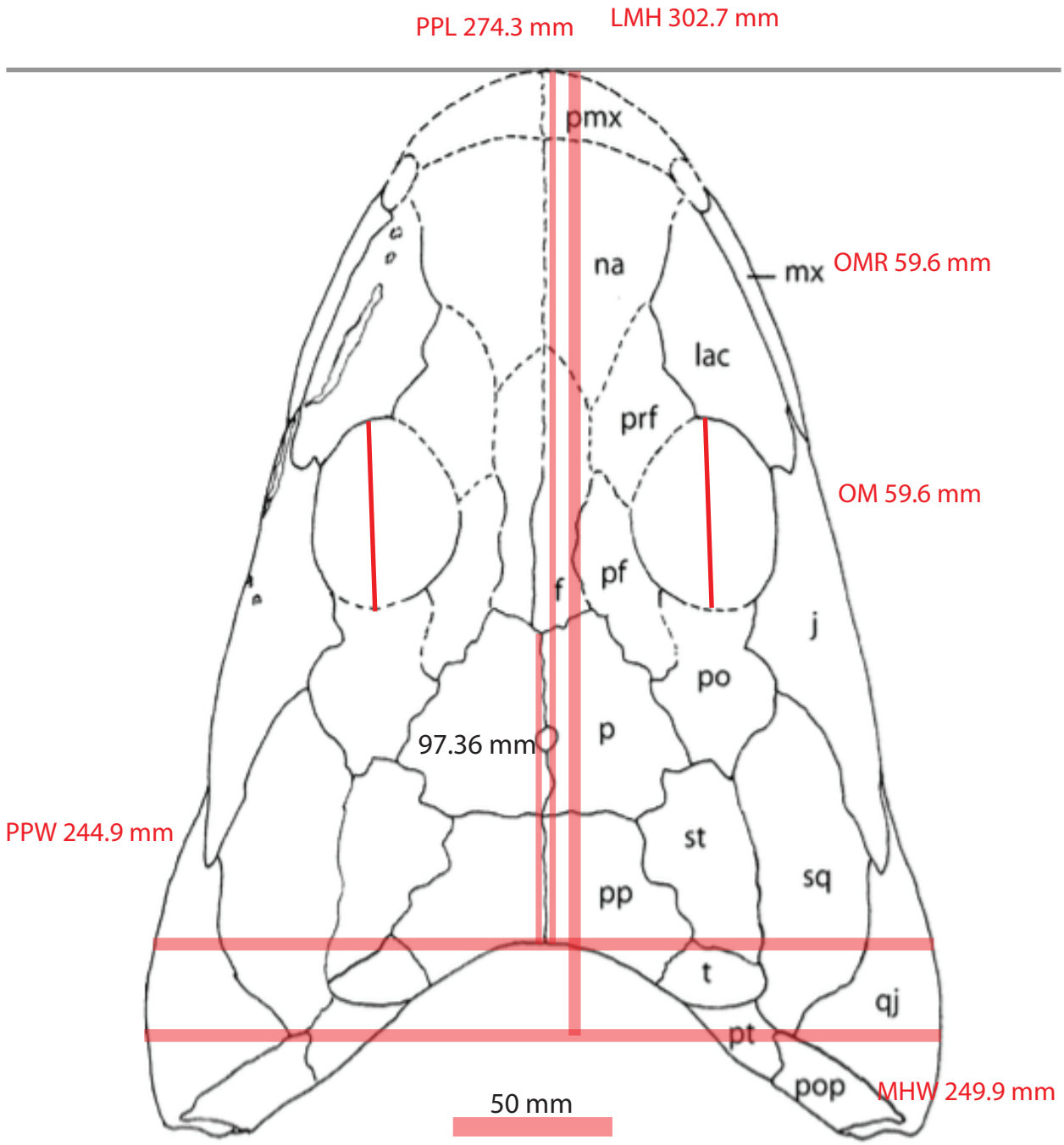

Ossinodus pueri
341.4-336.2 Ma
Digited tetrapod (scaled 50%)
Warren and Turner (2004); Warren (2007)

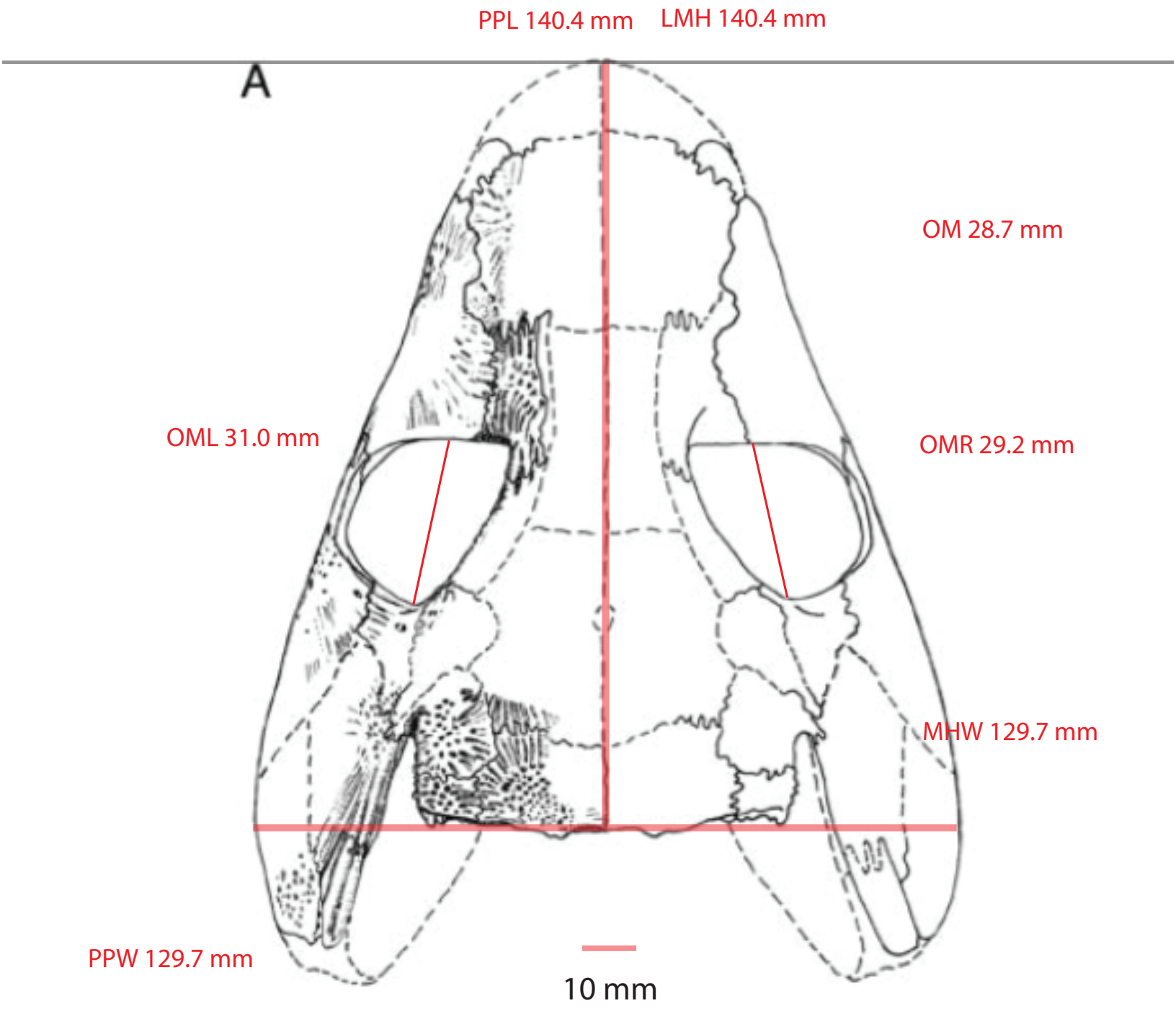

Pederpes finneyae
350.8-346.7 Ma
Digited tetrapod (actual size)
Clack & Finney (2004)

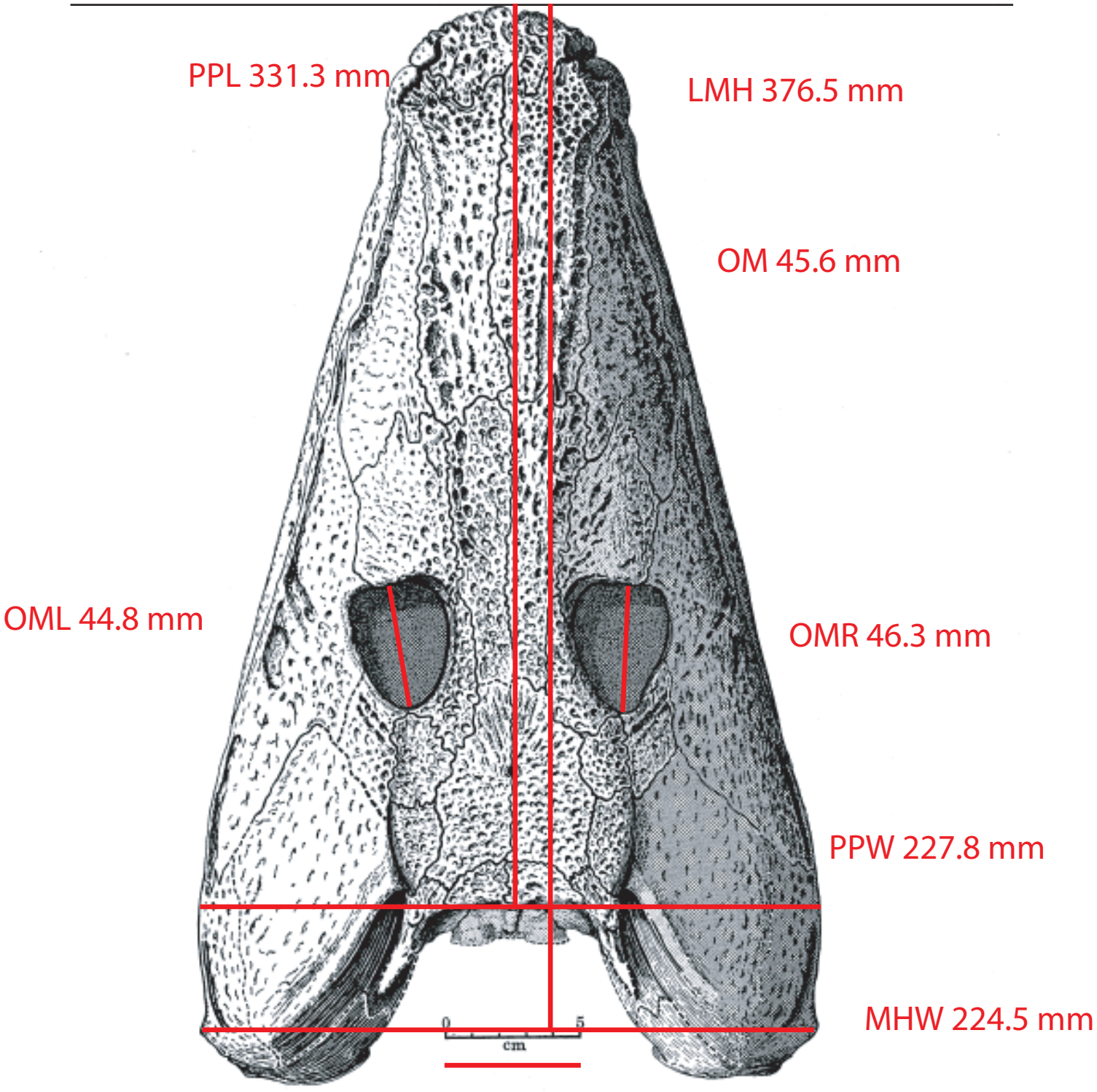

Eogyrinus attheyi
319.2-315.2 Ma
Digited tetrapod (Actual Size)
Panchen (1972)

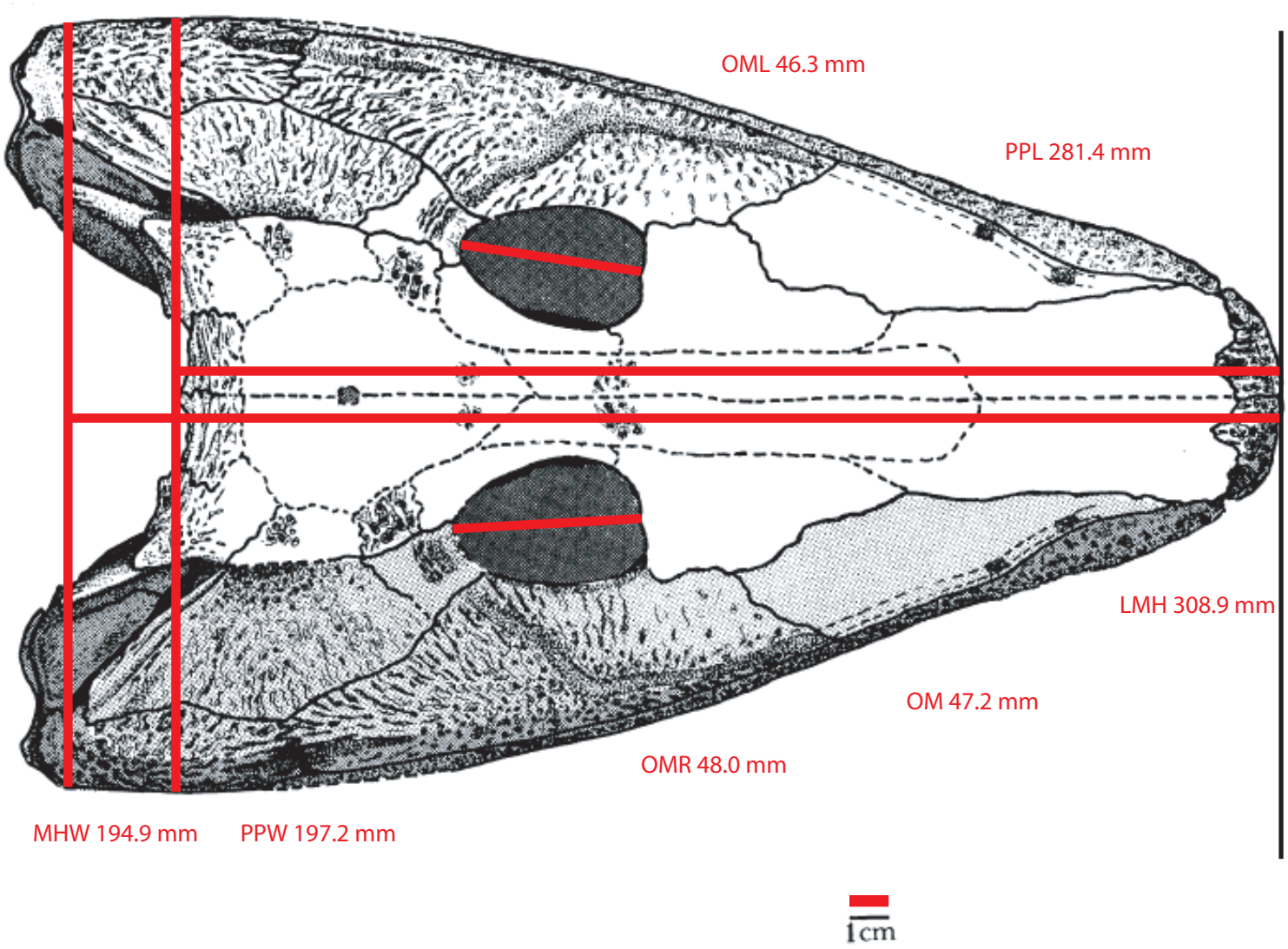

Pholiderpeton scutigerum
330.9-315.2 Ma
Digited tetrapod (scaled 60%)
Clack (1987)

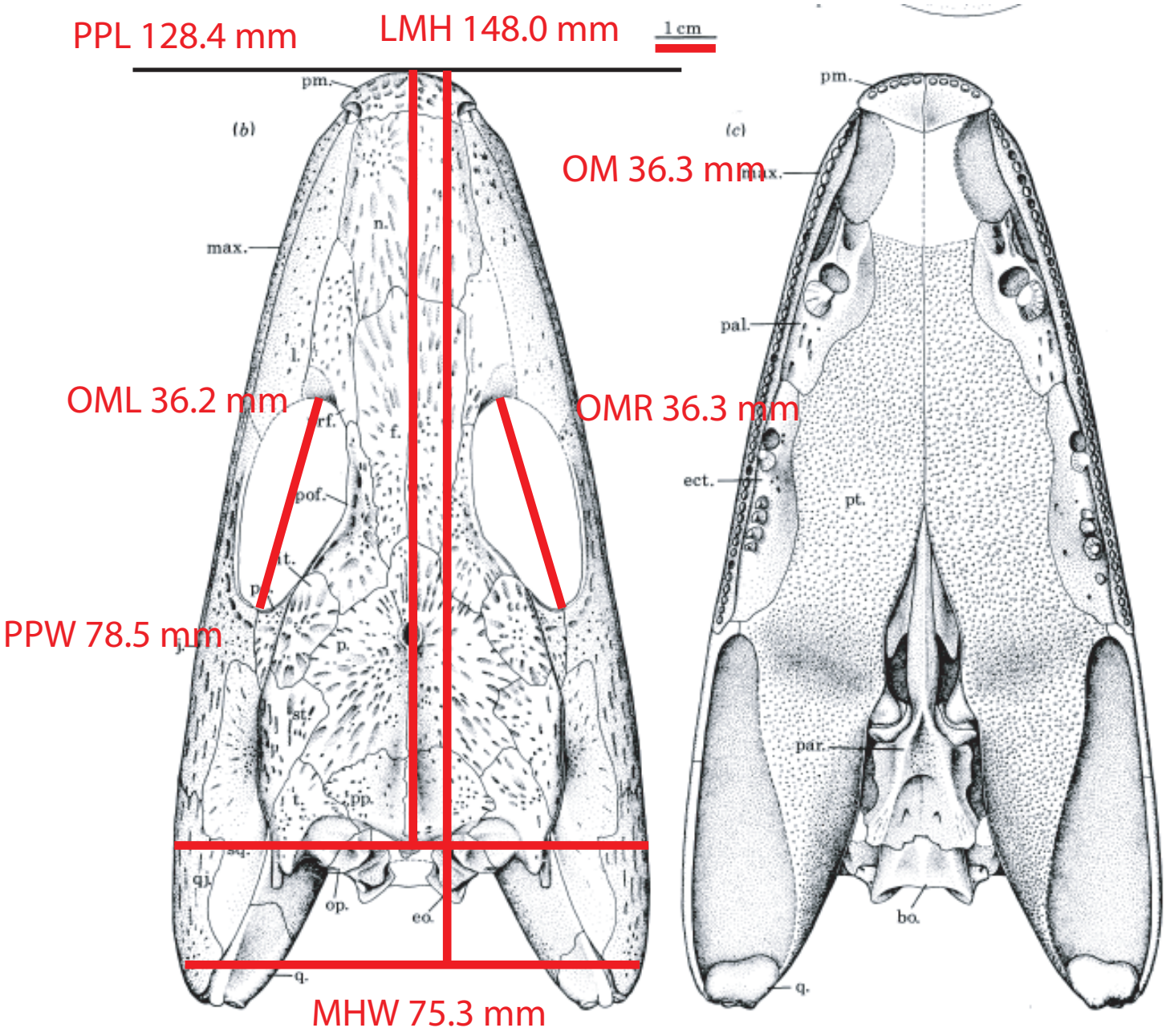

Proterogyrinus scheelei
330.9-323.2 Ma
Digited tetrapod (actual size)
Holmes (1984)

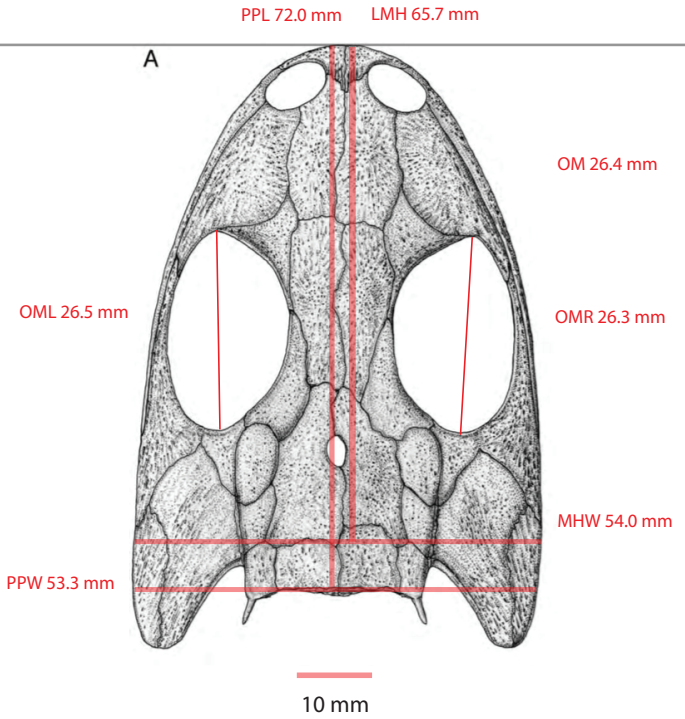

Silvanerpeton miripedes
336.2-330.9 Ma
Digited tetrapod (actual size)
Ruta and Clack 2006

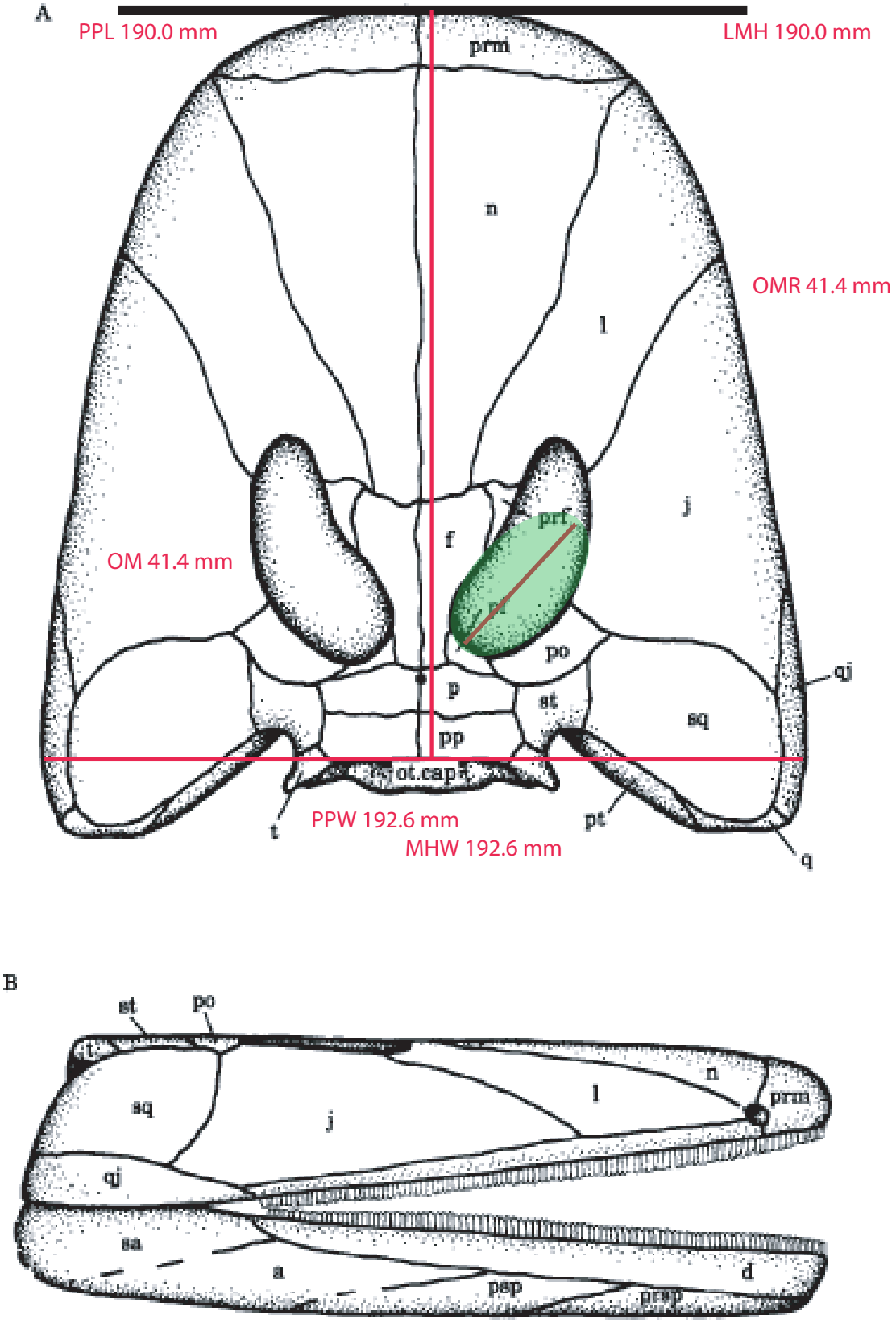

Spathicephalus mirus

330.9-327.1 Ma

Digited tetrapod (scaled 65%)

Beaumont and Smithson (1998)

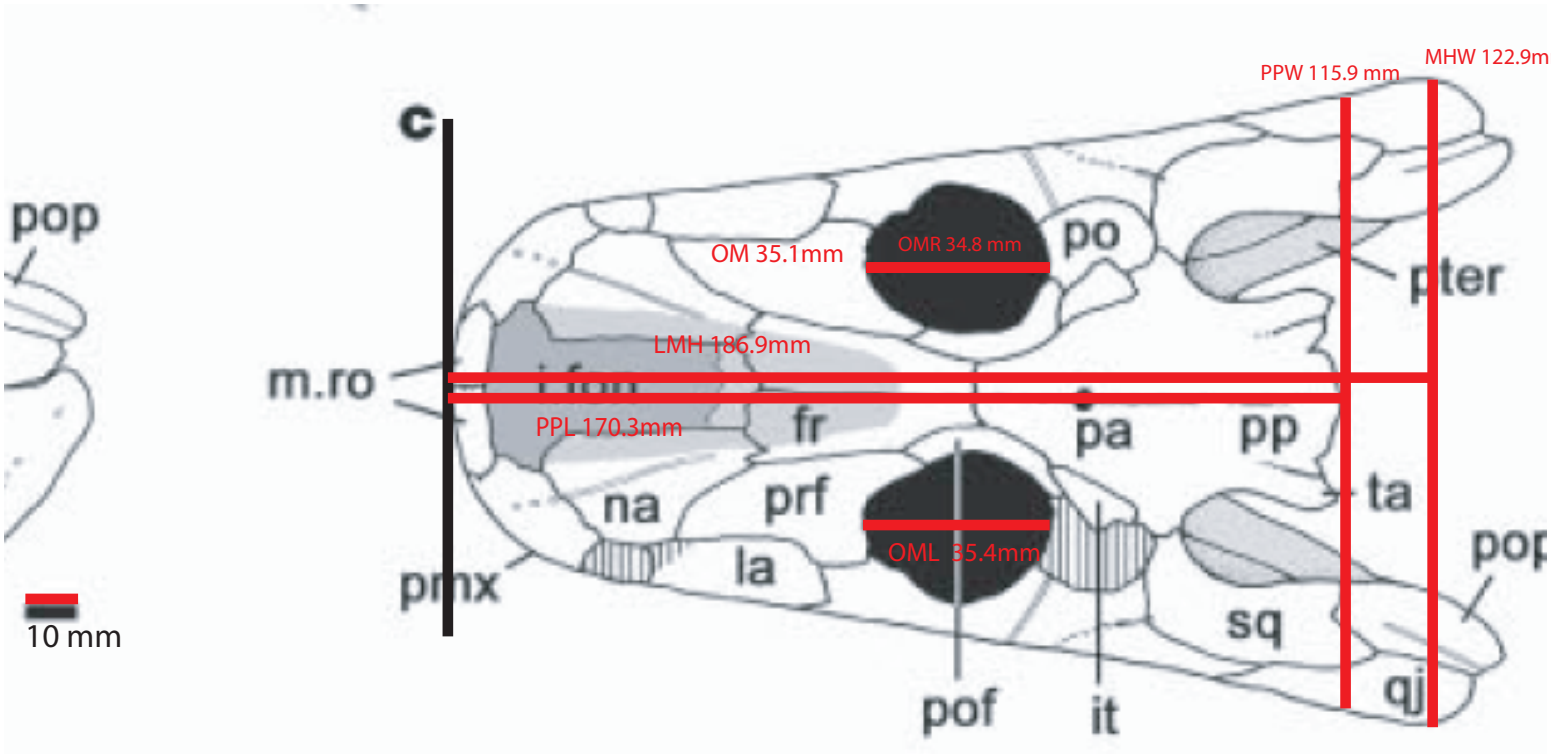

Ventastega curonica
363.3-358.9 Ma
Digited tetrapod (scaled 70%)
Ahlberg et al. (2008)

1. Nilsson DE, Warrant E, Johnsen S (2014) Computational visual ecology in the pelagic realm. *Philosophical Transactions of the Royal Society B-Biological Sciences* 369(1636).

2. Duntley SQ (1948) The visibility of distant objects. *Journal of the Optical Society of America* 38(3):237–249.

3. Horvath H (1971) On the applicability of the Koschmieder visibility formula. *Atmospheric Environment* 5:177–184.

4. Middleton WEK (1952) *Vision through the atmosphere*. (University of Toronto Press, Toronto), pp. xiv, 250 pages.

5. Dorno C (1919) Observations of sun- and sky- rays and their importance for climatology and biology as well as for geophysics and astronomy. *Naturwissenschaften* 7(1-52):1007–1012.

6. Cronin TW, Johnsen S, Marshall NJ, Warrant EJ (2014) *Visual ecology*. (Princeton University Press, Princeton, N.J.), pp. xx, 405 sider.

7. Warrant EJ, Nilsson DE (1998) Absorption of white light in photoreceptors. *Vision Research* 38(2):195–207.

8. Wyszecki G, Stiles WS (1967) *Color science: concepts and methods, quantitative data and formulas*. (Wiley New York), pp. xiv, 628.

9. Snyder AW (1979) Physics of vision in compound eyes in *Comparative Physiology and Evolution of Vision in Invertebrates: A: Invertebrate Photoreceptors*, ed. Autrum H. (Springer Berlin Heidelberg, Berlin, Heidelberg), pp. 225–313.

10. Aho AC, Donner K, Reuter T (1993) Retinal origins of the temperature effect on absolute visual sensitivity in frogs. *Journal of Physiology-London* 463:501–521.

11. Blackwell HR (1946) Contrast thresholds of the human eye. *Journal of the Optical Society of America* 36(11):624–643.

12. Killinger D, Churnside J, Rothman L (1995) Atmospheric optics in *Handbook of optics*, eds. Bass M, of America. OS. (McGraw-Hill, New York) Vol. 1, 2nd edition, pp. 44.1–44.49.

13. Aksyutov L (2002) Operational thresholds of the spatial resolution of the visual system and the contrast perception of objects. *Journal of Optical Technology* 69(8):552.

14. Land MF, Nilsson DE (2012) *Animal eyes*, Oxford animal biology series. (Oxford University Press, Oxford ; New York), 2nd edition, pp. xiii, 271 p., 4 p. of plates.

15. Clack JA (2012) *Gaining ground : The origin and evolution of tetrapods*. (Indiana University Press, Bloomington).

16. Narkiewicz M et al. (2015) Palaeoenvironments of the Eifelian dolomites with earliest tetrapod trackways (Holy Cross Mountains, Poland). *Palaeogeography Palaeoclimatology Palaeoecology* 420:173–192.

17. Retallack GJ (2011) Woodland Hypothesis for Devonian Tetrapod Evolution. *Journal of Geology* 119(3):235–258.

18. Daeschler EB, Shubin NH, Jenkins FA (2006) A Devonian tetrapod-like fish and the evolution of the tetrapod body plan. *Nature* 440(7085):757–763.

19. Clack JA (2007) Devonian climate change, breathing, and the origin of the tetrapod stem group. *Integr. Comp. Biol.* 47(4):510–523.

20. Stein WE, Berry CM, Hernick LV, Mannolini F (2012) Surprisingly complex community discovered in the mid-Devonian fossil forest at Gilboa. *Nature* 483(7387):78–81.

21. Mobley CD (1995) The optical properties of water in *Handbook of optics*, ed. Bass M. (McGraw-Hill, New York) Vol. 1, 2nd edition, pp. 43.3–43.56.

22. Johnsen S, Widder EA, Mobley CD (2004) Propagation and perception of bioluminescence: Factors affecting counterillumination as a cryptic strategy. *The Biological Bulletin* 207(1):1–16.

23. Davies-Colley RJ, Nagels JW (2008) Predicting light penetration into river waters. *Journal of Geophysical Research: Biogeosciences* 113(G3):1–9.

24. Davies-Colley RJ (1988) Measuring water clarity with a black disk. *Limnology and Oceanography* 33(4):616–623.

25. Koenings J, Edmundson J (1991) Secchi disk and photometer estimates of light regimes in Alaskan lakes: Effects of yellow color and turbidity. *Limnology and Oceanography* 36(1):91–105.

26. Harrison A, Coombes C (1988) An opaque cloud cover model of sky short wavelength radiance. *Solar Energy* 41(4):387–392.

27. Steen M (2014) Spectrum of moonlight. http://www.olino.org/us/articles/2015/10/05/spectrum-of-moon-light.

28. Mobley CD (1994) *Light and water: radiative transfer in natural waters*. (Academic press).

29. Raven J, Cockell C (2006) Influence on Photosynthesis of Starlight, Moonlight, Planetlight, and Light Pollution (Reflections on Photosynthetically Active Radiation in the Universe). *Astrobiology* 6(4):668–675.

30. Johnsen S et al. (2006) Crepuscular and nocturnal illumination and its effects on color perception by the nocturnal hawkmoth deilephila elpenor. *Journal of Experimental Biology* 209(5):789–800.

31. Brown M (1981) The measurement and simulation of the light of the night sky, (DTIC Document), Technical report.

32. Stavenga D, Smits R, Hoenders B (1993) Simple exponential functions describing the absorbance bands of visual pigment spectra. *Vision research* 33(8):1011–1017.

33. Duntley S, Preisendorfer R (1952) The visibility of submerged objects. *Final Report to Office of Naval Research*.

34. Trivedi CA, Bollmann JH (2013) Visually driven chaining of elementary swim patterns into a goal-directed motor sequence: a virtual reality study of zebrafish prey capture. *Frontiers in Neural Circuits* 7(86).

35. Dunn TW et al. (2016) Neural Circuits Underlying Visually Evoked Escapes in Larval Zebrafish. *Neuron* 89(3):613–628.

36. Temizer I, Donovan JC, Baier H, Semmelhack JL (2015) A Visual Pathway for Looming-Evoked Escape in Larval Zebrafish. *Curr. Biol.* 25(14):1823–1834.

37. Preuss T, Osei-Bonsu PE, Weiss SA, Wang C, Faber DS (2006) Neural representation of object approach in a decision-making motor circuit. *The Journal of Neuroscience* 26(13):3454–3464.

38. Ben-Tov M, Donchin O, Ben-Shahar O, Segev R (2015) Pop-out in visual search of moving targets in the archer fish. *Nat Commun* 6:6476.

39. Webb PW (1984) Form and function in fish swimming. *Sci. Am.* 251:58–68.

40. Snyder JB, Nelson ME, Burdick JW, MacIver MA (2007) Omnidirectional sensory and motor volumes in an electric fish. *PLoS Biology* 5(11):2671–2683.

41. MacIver MA (2009) Neuroethology: From morphological computation to planning in *The Cambridge Handbook of Situated Cognition*, eds. Robbins P, Aydede M. (Cambridge University Press, New York, NY), pp. 480–504.

42. Jun JJ, Longtin A, Maler L (2014) Enhanced sensory sampling precedes self-initiated locomotion in an electric fish. *Journal of Experimental Biology* 217(20):3615–3628.

43. Haggard P (2008) Human volition: towards a neuroscience of will. *Nature Reviews Neuroscience* 9(12):934–946.

44. Nilsson DE, Warrant EJ, Johnsen S, Hanlon R, Shashar N (2012) A unique advantage for giant eyes in giant squid. *Current Biology* 22(8):683–688.

45. Hester FJ (1968) Visual contrast thresholds of goldfish (*Carassius auratus*). *Vision Research* 8(10):1315–1335.

46. Ansari A, Murphey TD (2016) Sequential action control: Closed-form optimal control for nonlinear systems. *Under review at: IEEE Transactions on Robotics*.

47. Paradis E, Claude J, Strimmer K (2004) Ape: Analyses of phylogenetics and evolution in R language. *Bioinformatics* 20(2):289–290.

48. Uyeda JC, Harmon LJ (2014) A novel Bayesian method for inferring and interpreting the dynamics of adaptive landscapes from phylogenetic comparative data. *Systematic Biology* 63(6):902–918.

49. Uyeda JC, Eastman J, Harmon L (2015) *bayou: Bayesian Fitting of Ornstein-Uhlenbeck Models to Phylogenies*. R package version 1.1.0.

50. Harmon LJ, Weir JT, Brock CD, Glor RE, Challenger W (2008) Geiger: investigating evolutionary radiations. *Bioinformatics* 24(1):129–131.

51. Venables WN, Ripley BD (2002) *Modern Applied Statistics with S*. (Springer, New York), Fourth edition.

52. Pinheiro J, Bates D, DebRoy S, Sarkar D, R Core Team (2014) *nlme: Linear and Nonlinear Mixed Effects Models*. R package version 3.1-117.

53. Beaulieu JM, O'Meara B (2016) *OUwie: Analysis of Evolutionary Rates in an OU Framework*. R package version 1.49.

54. Bapst DW (2012) paleotree: an R package for paleontological and phylogenetic analyses of evolution. *Methods in Ecology and Evolution* 3(5):803–807.

55. Revell LJ (2012) phytools: An R package for phylogenetic comparative biology (and other things). *Methods in Ecology and Evolution* 3:217–223.

56. Hansen TF, Pienaar J, Orzack SH (2008) A comparative method for studying adaptation to a randomly evolving environment. *Evolution* 62(8):1965–1977.

57. Pienaar J (2011) *slouch: Stochastic Linear Ornstein Uhlenbeck models for Comparative Hypotheses*. R package version 1.2.

58. Bell MA, Lloyd GT (2014) *strap: Stratigraphic Tree Analysis for Palaeontology*. R package version 1.4.

59. Hutchinson JR (2012) On the inference of function from structure using biomechanical modelling and simulation of extinct organisms. *Biol. Lett.* 8(1):115–118.

60. Anderson PS, Bright JA, Gill PG, Palmer C, Rayfield EJ (2012) Models in palaeontological functional analysis. *Biol. Lett.* 8(1):119–122.

61. McInroe B et al. (2016) Tail use improves performance on soft substrates in models of early vertebrate land locomotors. *Science* 353(6295):154–158.

62. Angielczyk KD, Schmitz L (2014) Nocturnality in synapsids predates the origin of mammals by over 100 million years. *Proc. Biol. Sci.* 281(1793).

63. Schmitz L (2009) Quantitative estimates of visual performance features in fossil birds. *Journal of Morphology* 270(6):759–773.

64. Hall MI (2009) The relationship between the lizard eye and associated bony features: A cautionary note for interpreting fossil activity patterns. *Anatomical Record-Advances in Integrative Anatomy and Evolutionary Biology* 292(6):798–812.

65. Schmitz L, Wainwright PC (2011) Nocturnality constrains morphological and functional diversity in the eyes of reef fishes. *Bmc Evolutionary Biology* 11.

66. Wainwright PC, Bellwood DR, Westneat MW, Grubich JR, Hoey AS (2004) A functional morphospace for the skull of labrid fishes: patterns of diversity in a complex biomechanical system. *Biological Journal of the Linnean Society* 82(1):1–25.

67. Rabosky DL et al. (2013) Rates of speciation and morphological evolution are correlated across the largest vertebrate radiation. *Nature Communications* 4.

68. Symonds MRE, Blomberg SP (2014) A primer on phylogenetic generalised path analysis in *Modern phylogenetic comparative methods and their application in evolutionary biology*, ed. Garamszegi LZ. (Springer, Heidelberg, New York, Dordrecht, London), p. 552.

69. Milner AC, Milner AR, Walsh SA (2009) A new specimen of *Baphetes* from Nýřany, Czech Republic and the intrinsic relationships of the Baphetidae. *Acta Zoologica* 90:318–334.

70. Motani R, Rothschild BM, Wahl WJ (1999) Large eyeballs in diving ichthyosaurs. *Nature* 402:402.

71. Porro LB, Rayfield EJ, Clack JA (2015) Descriptive Anatomy and Three-Dimensional Reconstruction of the Skull of the Early Tetrapod *Acanthostega gunnari* Jarvik, 1952. *PLOS ONE* 10(3).

72. Brough MC, Brough J (1967) Studies on early tetrapods III. the genus *Gephyrostegus*. *Philosophical Transactions of the Royal Society of London Series B-Biological Sciences* 252(776):147–165.

73. Benton MJ (2005) *Vertebrate Palaeontology*. (Blackwell Publishing, Malden, Oxford, Victoria).

74. Schoch RR (2014) *Amphibian Evolution: The Life of Early Land Vertebrates*. (John Wiley & Sons, Oxford).

75. Schmitz L, Motani R (2011) Nocturnality in dinosaurs inferred from scleral ring and orbit morphology. *Science* 332:705–708.

76. Kirk EC (2004) Comparative morphology of the eye in primates. *The Anatomical Record* 281A:1095–1103.

77. Schmitz L et al. (2013) Allometry indicates giant eyes of giant squid are not exceptional. *BMC Evolutionary Biology* 13.

78. Howland HC, Merola S, Basarab JR (2004) The allometry and scaling of the size of vertebrate eyes. *Vision Research* 44(17):2043 – 2065.

79. Revell LJ (2009) Size-correction and principal components for interspecific comparative studies. *Evolution* 63(12):3258–3268.

80. Hansen TF (2014) Use and misuse of comparative methods to study adaptation in *Modern phylogenetic comparative methods and their application in evolutionary biology*, ed. Garamszegi LZ. (Springer, Heidelberg, New York, Dordrecht, London), p. 552.

81. Nilsson DE, Pelger S (1994) A pessimistic estimate of the time required for an eye to evolve. *Proc. Biol. Sci.* 256(1345):53–58.

82. Douglas RH, Harper RD, Case JF (1998) The pupil response of a teleost fish, *Porichthys notatus*: description and comparison to other species. *Vision Res.* 38(18):2697–2710.

83. Bailes HJ, Trezise AE, Collin SP (2007) The optics of the growing lungfish eye: lens shape, focal ratio and pupillary movements in *Neoceratodus forsteri* (Krefft, 1870). *Vis. Neurosci.* 24(3):377–387.

84. Bailes HJ, Robinson SR, Trezise AE, Collin SP (2006) Morphology, characterization, and distribution of retinal photoreceptors in the Australian lungfish *Neoceratodus forsteri* (Krefft, 1870). *The Journal of Comparative Neurology* 494(3):381–397.

85. Warrant EJ (1999) Seeing better at night: life style, eye design and the optimum strategy of spatial and temporal summation. *Vision Research* 39(9):1611 – 1630.

86. BAILES HJ, TREZISE AE, COLLIN SP (2006) The number, morphology, and distribution of retinal ganglion cells and optic axons in the australian lungfish neoceratodus forsteri (krefft 1870). *Visual Neuroscience* 23:257–273.

87. Shear WA, Edgecombe GD (2010) The geological record and phylogeny of the Myriapoda. *Arthropod Struct Dev* 39(2-3):174–190.

88. Nagloo N, Collin SP, Hemmi JM, Hart NS (2016) Spatial resolving power and spectral sensitivity of the saltwater crocodile, *Crocodylus porosus*, and the freshwater crocodile, *Crocodylus johnstoni*. *Journal of Experimental Biology* 219(9):1394–1404.

89. Anderson PSL, Friedman M, Ruta M (2013) Late to the table: Diversification of tetrapod mandibular biomechanics lagged behind the evolution of terrestriality. *Integrative and Comparative Biology* 53(2):197–208.

90. MacIver MA, Sharabash NM, Nelson ME (2001) Prey-capture behavior in gymnotid electric fish: Motion analysis and effects of water conductivity. *J. Exp. Biol.* 204(3):543–557.

91. Shubin NH, Daeschler EB, Jenkins FA (2014) Pelvic girdle and fin of *Tiktaalik roseae*. *Proc. Natl. Acad. Sci. U.S.A.* 111(3):893–899.

92. Clack JA (2009) The fish–tetrapod transition: New fossils and interpretations. *Evolution: Education and Outreach* 2(2):213–223.

93. Paton RL, Smithson TR, Clack JA (1999) An amniote-like skeleton from the early carboniferous of scotland. *Nature* 398(6727):508–513.

94. Lin J, Wu Y, Huang TS (2000) Modeling the constraints of human hand motion in *Proceedings of the Workshop on Human Motion (HUMO'00)*, HUMO '00. (IEEE Computer Society, Washington, DC, USA), pp. 121–.

95. Liberzon D (2012) *Calculus of variations and optimal control theory : a concise introduction*. (Princeton University Press, Princeton; Oxford).

96. LaValle SM (2006) *Planning Algorithms*. (Cambridge University Press).

97. Todorov E (2004) Optimality principles in sensorimotor control. *Nat. Neurosci.* 7(9):907–915.

98. Partridge JC (1990) The color sensitivity and vision of fishes. *Light and Life in the Sea* pp. 167–184.

99. Land MF (1981) Optics and vision in invertebrates in *Handbook of Sensory Physiology*, ed. Autrum H. (Springer, New York) Vol. VII/6B, pp. 471–592.

100. Pirhofer-Walzl K, Warrant E, Barth FG (2007) Adaptations for vision in dim light: impulse responses and bumps in nocturnal spider photoreceptor cells (cupiennius salei keys). *Journal of Comparative Physiology A-Neuroethology Sensory Neural and Behavioral Physiology* 193(10):1081–1087.

101. Donner K, Koskelainen A, Djupsund K, Hemila S (1995) Changes in retinal time-scale under background light - observations on rods and ganglion-cells in the frog retina. *Vision Research* 35(16):2255–2266.

102. Miller WH (1979) Ocular optical filtering in *Comparative Physiology and Evolution of Vision in Invertebrates: A: Invertebrate Photoreceptors*, ed. Autrum H. (Springer Berlin Heidelberg, Berlin, Heidelberg) Vol. VII/6A, pp. 69–143.

103. Preisendorfer RW (1986) Secchi disk science: Visual optics of natural waters1. *Limnology and Oceanography* 31(5):909–926.

104. Long JA (1987) An unusual Osteolepiform fish from the Late Devonian of Victoria, Australia. *Palaeontology* 30:839–852.

105. Schultze HP, Reed JW (2012) A tristichopterid sarcopterygian fish from the upper Middle Devonian of Nevada. *Historical Biology* 24(4, SI):425–440.

106. Ahlberg PE, Johanson Z (1997) Second tristichopterid (Sarcopterygii, Osteolepiformes) from the Upper Devonian of Canowindra, New South Wales, Australia, and phylogeny of the Tristichopteridae. *Journal of Vertebrate Paleontology* 17(4):653–673.

107. Long JA (1985) New information on the head and shoulder girdle of *Canowindra grossi* Thomson, from the Late Devonian Mandagery Sandstone, New South Wales. *Records of the Australian Museum* 37(2):91–99.

108. Fox RC, Campbell K, Barwick R, Long J (1995) A new osteolepiform fish from the Lower Carboniferous Raymond Formation, Drummond Basin, Queensland. *Memoirs of The Queensland Museum* 38:125.

109. Young B, Dunstone RL, Senden TJ, Young GC (2013) A Gigantic Sarcopterygian (Tetrapodomorph Lobe-Finned Fish) from the Upper Devonian of Gondwana (Eden, New South Wales, Australia). *PLoS ONE* 8(3):e53871.

110. Schultze H, Arsenault M (1985) The Panderichthyid fish *Elpistostege*—A close relative of Tetrapods? *Palaeontology* 28(MAY):293–309.

111. Markey MJ, Marshall CR (2007) Terrestrial-style feeding in a very early aquatic tetrapod is supported by evidence from experimental analysis of suture morphology. *Proceedings of the National Academy of Sciences* 104(17):7134–7138.

112. Long JA, Young GC, Holland T, Senden TJ, Fitzgerald EM (2006) An exceptional Devonian fish from Australia sheds light on tetrapod origins. *Nature* 444(7116):199–202.

113. Johanson Z, Ahlberg PE (1998) A complete primitive rhizodont from Australia. *Nature* 394(6693):569–573.

114. Newman MJ, Mark-Kurik E, Den Blaauwen JL, Zupins I (2015) Scottish Middle Devonian fishes in Estonia. *Scottish Journal OF Geology* 52(2):141–147.

115. Snitting D (2009) *Heddleichthys*—a new tristichopterid genus from the Dura Den Formation, Midland Valley, Scotland (Famennian, Late Devonian). *Acta Zoologica* 90:273–284.

116. Young GC, Long JA, Ritchie A (1992) *Crossopterygian fishes from the Devonian of Antarctica : systematics, relationships, and biogeographic significance*. (Australian Museum, Sydney South, NSW, Australia).

117. Johanson Z, Ahlberg PE (1997) A new tristichopterid (Osteolepiformes: Sarcopterygii) from the Mandagery Sandstone (Late Devonian, Famennian) near Canowindra, NSW, Australia. *Transactions of the Royal Society of Edinburgh: Earth Sciences* 88:39–68.

118. Holland T, Long J, Snitting D (2010) New information on the enigmatic tetrapodomorph fish *Marsdenichthys longioccipitus* (Long, 1985). *Journal of Vertebrate Paleontology* 30(1):68–77.

119. Jarvik E (1948) *On the morphology and taxonomy of the middle Devonian osteolepid fishes of Scotland*, Kungliga Svenska Vetenskapsakademiens Handlingar. (Almqvist & Wiksells Boktryckeri, Stockholm) Vol. 25, pp. 1–301.

120. Witzmann F, Schoch RR (2012) A megalichthyid sarcopterygian fish from the Lower Permian (Autunian) of the Saar-Nahe Basin, Germany. *Geobios* 45(2):241 – 248.

121. Vorobyeva E, Schultze HP (1991) *Description and systematics of Panderichthyid fishes with comments on their relationship to tetrapods*. (Comstock Pub. Associates, Ithaca), pp. 68–109.

122. Jeffery JE (2012) Cranial morphology of the Carboniferous rhizodontid *Screbinodus ornatus* (Osteichthyes: Sarcopterygii). *Journal of Systematic Palaeontology* 10(3):475–519.

123. Swartz B (2012) A Marine Stem-Tetrapod from the Devonian of Western North America. *PLoS ONE* 7(3):e33683.

124. Clack JA (2002) Patterns and processes in the early evolution of the tetrapod ear. *J Neurobiol* 53(2):251–64.

125. Carroll R (1969) A new family of Carboniferous amphibians. *Palaeontology* 12(4):537–548.

126. Milner AR, Sequeira SEK (1998) A cochleosaurid temnospondyl amphibian from the middle Pennsylvanian of Linton, Ohio, USA. *Zoological Journal of the Linnean Society* 122(1-2):261–290.

127. Brough M, Brough J (1967) Studies on early tetrapods: I. Lower Carboniferous microsaurs. *Philosophical Transactions of the Royal Society of London Series B-Biological Sciences* 252(776):107–129.

128. Carroll RL (1967) An adelogyrinid lepospondyl amphibian from the Upper Carboniferous. *Canadian Journal of Zoology* 45(1):1–16.

129. Panchen AL (1977) On *Anthracosaurus russelli* Huxley (Amphibia: Labyrinthodontia) and the family Anthracosauridae. *Philosophical Transactions of the Royal Society of London B: Biological Sciences* 279(968):447–512.

130. Milner A, Sequeira S (1994) The Temnospondyl amphibians from the Visean of East Kirkton, West-Lothian, Scotland. *Transactions of the Royal Society of Edinburgh-Earth Sciences* 84(3-4):331–361.

131. Beaumont EH (1977) Cranial morphology of the Loxommatidae (Amphibia: Labyrinthodontia). *Philosophical Transactions of the Royal Society of London B: Biological Sciences* 280(971):29–101.

132. Hook RW (1993) *Chenoprosopus lewisi*, a new cochleosaurid amphibian (Amphibia: Temnospondyli) from the Permo-Carboniferous of north-central Texas. *Annals of the Carnegie Museum* 62(4):273–291.

133. Case E, Williston S, Mehl M (1913) *Permo-Carboniferous vertebrates from New Mexico*, Carnegie Institution of Washington publication. (Carnegie Institution of Washington).

134. Sequeira SEK (2003) The skull of *Cochleosaurus bohemicus* Frič, a temnospondyl from the Czech Republic (Upper Carboniferous) and cochleosaurid interrelationships. *Transactions of the Royal Society of Edinburgh: Earth Sciences* 94:21–43.

135. Hook RW (1983) *Colosteus scutellatus (Newberry): a primitive temnospondyl amphibian from the Middle Pennsylvanian of Linton, Ohio*, American Museum novitates,. (American Museum of Natural History, New York N Y) Vol. no. 2770, p. 41 pages.

136. Panchen AL (1985) On the amphibian Crassigyrinus scoticus Watson from the *Carboniferous of Scotland*. *Philosophical Transactions of the Royal Society of London. Series B, Biological Sciences* 309(1140):505–568.

137. Bolt JR, Lombard RE (2010) *Deltaherpeton Hiemstrae*, a new Colosteid Tetrapod from the Mississippian of Iowa. *Journal of Paleontology* 84(6):1135–1151.

138. Robert B. Holmes, Robert L. Carroll RRR (1998) The First Articulated Skeleton of *Dendrerpeton acadianum* (Temnospondyli, Dendrerpetontidae) from the Lower Pennsylvanian Locality of Joggins, Nova Scotia, and a Review of Its Relationships. *Journal of Vertebrate Paleontology* 18(1):64–79.

139. Alfred S. Romer RVW (1942) *Edops*, a Primitive Rhachitomous Amphibian from the Texas Red Beds. *The Journal of Geology* 50(8):925–960.

140. Smithson TR (1985) The morphology and relationships of the Carboniferous amphibian *Eoherpeton watsoni* Panchen. *Zoological Journal of the Linnean Society* 85(4):317–410.

141. Clack JA (1998) A new Early Carboniferous tetrapod with a *mélange* of crown-group characters. *Nature* 394(6688):66–69.

142. Benton JM (2000) *Vertebrate Palaeontology, Second Edition*. (Australian Museum).

143. Clack J (2003) A new baphetid (stem tetrapod) from the Upper Carboniferous of Tyne and Wear, UK, and the evolution of the tetrapod occiput. *CANADIAN JOURNAL OF EARTH SCIENCES* 40(4):483–498.

144. Sidor CA et al. (2005) Permian tetrapods from the sahara show climate-controlled endemism in pangaea. *Nature* 434(7035):886–889.

145. Warren A, Turner S (2004) The first stem tetrapod from the Lower Carboniferous of Gondwana. *Palaeontology* 47(1):151–184.

146. Warren A (2007) New data on *Ossinodus pueri*, a stem tetrapod from the Early Carboniferous of Australia. *Journal of Vertebrate Paleontology* 27(4):850–862.

147. Clack JA, Finney SM (2004) *Pederpes finneyae*, an articulated tetrapod from the Tournaisian of western Scotland. *Journal of Systematic Palaeontology* 2(4):311–346.

148. Panchen AL (1972) The skull and skeleton of *Eogyrinus attheyi* Watson (Amphibia: Labyrinthodontia). *Philosophical Transactions of the Royal Society of London B: Biological Sciences* 263(851):279–326.

149. Clack JA (1987) *Pholiderpeton scutigerum* Huxley, an Amphibian from the Yorkshire Coal Measures. *Philosophical Transactions of the Royal Society of London B: Biological Sciences* 318(1188):1–107.

150. Holmes R (1984) The carboniferous amphibian *Proterogyrinus scheelei* Romer, and the early evolution of tetrapods. *Philosophical Transactions of the Royal Society of London. Series B, Biological Sciences* 306(1130):431–524.

151. Ruta M, Clack JA (2006) A review of *Silvanerpeton miripedes*, a stem amniote from the Lower Carboniferous of East Kirkton, West Lothian, Scotland. *Transactions of the Royal Society of Edinburgh: Earth Sciences* 97:31–63.

152. Beaumont E, Smithson T (1998) The cranial morphology and relationships of the aberrant carboniferous amphibian *Spathicephalus mirus* watson. *ZOOLOGICAL JOURNAL OF THE LINNEAN SOCIETY* 122(1-2):187–209.

153. Ahlberg PE, Clack JA, Luksevics E, Blom H, Zupins I (2008) *Ventastega curonica* and the origin of tetrapod morphology. *Nature* 453(7199):1199–204.

154. Lombard RE, Bolt JR (1995) A new primitive tetrapod, *Whatcheeria deltae*, from the Lower Carboniferous of Iowa. *Palaeontology* 38:471–494.

155. Cohen KM, Finney SC, Gibbard PL, Fan JX (2013) The ICS International Chronostratigraphic Chart, update v2015/01. *Episodes* 36(3):199–204.